ATOMIC FORCE MICROSCOPY METHODS FOR THE ANALYSIS OF HIGH-LET TRACKS IN CR-39 PLASTIC NUCLEAR TRACK DETECTOR

By

CARL E. JOHNSON Jr.

Bachelor of Science in Physics
University of Arkansas at Little Rock
Little Rock, Arkansas
2003

Master of Science in Applied Science
University of Arkansas at Little Rock
Little Rock, Arkansas
2005

Submitted to the Faculty of the
Graduate College of the
Oklahoma State University
in partial fulfillment of
the requirements for
the Degree of
DOCTOR OF PHILOSOPHY
July, 2009

ATOMIC FORCE MICROSCOPY METHODS FOR THE ANALYSIS OF HIGH-LET TRACKS IN CR-39 PLASTIC NUCLEAR TRACK DETECTOR

Dissertation Approved:

Eric R. Benton

Dissertation Adviser

Andy S. Arena

Eduardo Yukihara

Albert Rosenberger

A. Gordon Emslie

Dean of the Graduate College

ACKNOWLEDGMENTS

I am very grateful for the assistance provided by many individuals over the course of this research project. There is insufficient space for me to thank everyone, in the detail that they deserve, or address fully each individual who has provided essential guidance and support, but I hope these acknowledgments will be sufficiently complete to convey my deep gratitude, both to friends and family and to the faculty members instrumental to my education.

I appreciate very much the contribution of accelerator beam time from many institutions. The beam time provided by LLUMC as well as the donation of the atomic force microscope used in our detector analyses was essential to this work. The NASA Space Radiation Laboratory at Brookhaven donated beam time for both proton exposures and calibration detectors. The NIRS HIMAC accelerator donated beams for various calibration detectors as well.

I have been fortunate to have Eric Benton as my advisor. His tireless enthusiasm for rigorous scientific investigation has been inspirational and his dedication to physics education is unrivaled.

I am grateful for many helpful discussions with Koichi Ogura and Nahahiro Yasuda. Many thanks to Joel DeWitt and Chris Austin for critical readings of this work.

The assistance of my committee members has been greatly appreciated. Special thanks are extended to Art Lucas. Art’s extensive body of knowledge in radiation detection and dosimetry was helpful on many occasions. Mike Lucas of the Physics and Chemistry Instrument and Machine Shop was also very helpful with detector stand fabrication.

I am thankful for the faculty of the OSU Physics Department for kind guidance and instruction during my coursework. I am especially grateful for the help of Paul Westhaus, who while Graduate Coordinator, was instrumental in insuring that I was able to complete my education.

Throughout my youth, my mother always encouraged me to do my very best and she was able to convince me, with repeated praise, that I was capable of achieving anything. Thanks mom!

For giving me two wonderful reasons for wanting to become a better man, I thank my sons Nathan and Andrew. Boys, I will always love you!

And most importantly of all, my wife Maureen deserves a great deal of credit for my success and without her this work would not have been possible. She was the one who encouraged me to pursue this degree and she was also the one to stick with me every step of the way through it. Maureen never lost faith in me even long after I had lost faith in myself. I love you always honey!

Maureen, I lovingly dedicate this dissertation to you!

TABLE OF CONTENTS

Chapter Page

LIST OF TABLES

LIST OF FIGURES

CHAPTER I

INTRODUCTION

Proton- and neutron-induced target fragmentation of heavy nuclei is a class of medium energy nuclear reaction with relevance to proton cancer therapy, the radiation protection of space crews and avionics, and radiation protection from neutrons. Target fragmentation reactions in tissue are capable of depositing energy greater than that of the incident nucleon (proton or neutron) over very short-range (~10 μm) by generating secondary particles consisting of knock-out protons, neutrons, alpha-particles, and heavy nuclear recoil (HNR) particles. The contribution from HNR particles to patient total dose during proton cancer therapy or to the total absorbed dose received by an astronaut during space flight is not precisely known, due to the difficulty in directly measuring these short-range recoil particles. This thesis develops a method to directly measure the contribution from proton- and neutron-induced HNR particles to total dose using CR-39 plastic nuclear track detector (PNTD) analyzed using of atomic force microscopy (AFM).

1.0 Importance of HNR Particles

HNR particles may make a significant contribution to total absorbed dose in healthy tissue surrounding an irradiated tumor during proton cancer treatment. In proton cancer therapy, cyclotrons or synchrotrons produce beams of energetic protons of known, fixed energy to directly irradiate malignant tumors located deep inside the patient's body [Wilson, 1946; Gottschalk et al., 1982]. An energetic proton beam passes through healthy tissue and stops inside the tumor volume, thereby depositing energy, killing the cancer cells within. Energy is transferred from the protons of the beam to tissue through electromagnetic (Coulomb) interactions between the protons and the constituent orbital electrons of the healthy tissue and tumor. The deposition of energy per unit path length (measured in units of keV/µm) along the proton beam's trajectory, i.e. as a function of depth in tissue, is referred to as the linear energy transfer (LET) and is described by the Bragg curve shown in Figure 1. The Bragg curve shows the relationship between LET, which is proportional to absorbed dose (in Gy or J/kg), and depth in tissue or water.

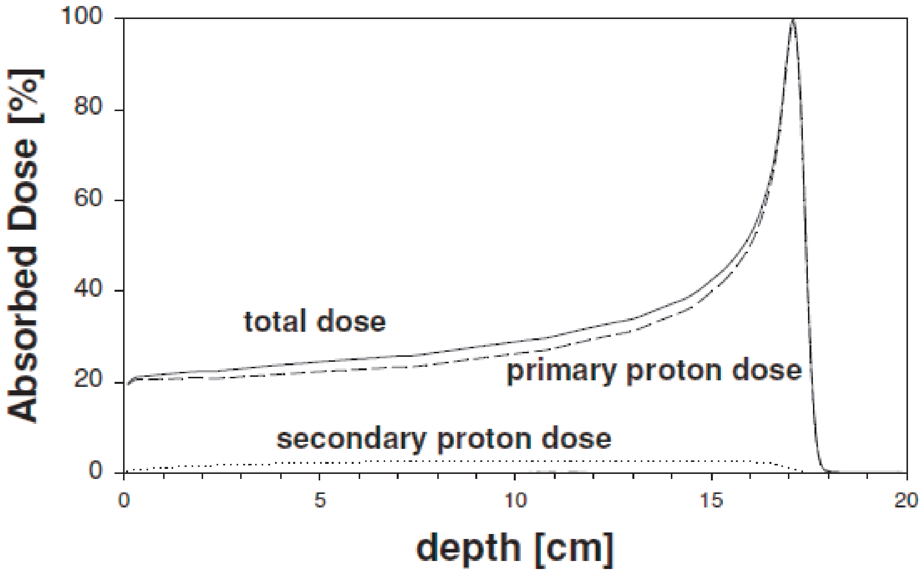

Figure 1. The Bragg peak for a proton beam (160 MeV) in water showing the contributions to dose from both primary and secondary protons [Paganetti, 2002]. Absorbed dose on the y-axis is proportional to primary proton LET.

For proton beams, the Bragg curve consists of a flat region known as the plateau, after which the LET rises up to its peak value in a region called the Bragg peak, the region of maximum energy transfer. In the Bragg peak, the protons expend their energy completely and stop. For the range of proton beam energy in clinical use, roughly 50 to 250 MeV, the proton LET in the plateau is 1.2 to 0.4 keV/µm respectively. Near the Bragg peak, proton LET rises quickly to its maximum, ~95 keV/µm [ICRU, 1993]. The depth in tissue of the proton Bragg peak is a function of proton energy. As proton energy increases, the overall proton range in tissue increases and the location of the Bragg peak is correspondingly deeper. It is the distinctive pattern of energy deposition as a function of tissue depth, wherein less energy is deposited at the beginning of a proton's range, corresponding to healthy tissue in front of the tumor volume, while the majority of energy is deposited over a relatively short distance near the end of its range, i.e. the Bragg peak, corresponding to the tumor volume, that represents the major advantage of proton cancer therapy over other forms of radiotherapy such as X-ray and energetic electron beams.

In the clinical application of proton radiotherapy, multiple proton energies are used since the tumor occupies a range of depth inside the patient. Each proton energy has a distinct Bragg peak which when combined form the so-called spread out Bragg peak (SOBP) [Koehler et al., 1975; Gottschalk et al., 1993; Lu et al., 2006]. The techniques used in proton radiotherapy can be summarized as methods that physically modify the cross-sectional area and energy of the beam such that the associated Bragg peak matches the physical location of the tumor volume within the patient.

It is important to note that the distinctive profile of energy deposition as a function of proton range represented by the Bragg curve is entirely the result of Coulomb interactions between the energetic protons of the beam and the electrons that occupy the bulk of the volume of the target tissue. Nuclear interactions between the protons of the beam and the constituent nuclei of the target tissue are far less frequent, making only a small contribution to the Bragg curve. However, in nuclear collisions such as proton-induced target fragmentation reactions, it is possible to produce secondary protons, neutrons, alpha-particles, intermediate mass fragments (IMFs) with $Z \lesssim 10$, and heavy nuclear recoil (HNR) particles, all of which contribute to patient dose and especially to the dose deposited in healthy tissue corresponding to the plateau of the Bragg curve [Wilson et al., 1993; Chadwick et al., 1998].

HNR particles have much larger LET values than the primary protons of the treatment beam and, generally a shorter range (≤10 μm in tissue) [Shinn et al., 1990]. Estimates of the contribution from HNR particles to the dose to healthy tissue have been made using Monte Carlo simulations [Paganetti et al., 1997; Wroe et al., 2005] and analytical models [Bortfeld, 1997], but only a limited number of measurements of the actual contribution to healthy tissue dose have been made [Benton et al., 2002c]. It is known that these initial experiments made using CR-39 PNTD analyzed by standard visible light microscopy, only measured a fraction of the total dose deposited by HNR particles.

In proton radiotherapy the contribution from HNR particles to total dose is expected to be small [Paganetti et al., 1997], but experimental confirmation has been complicated due to difficulties in making direct measurements of short-range ($\leq$ 10 μm) particles. Active detectors generally have a protective outer casing that is too thick for short-range particles to traverse. A short-range particle formed in the wall of an active detector, such as a tissue equivalent proportional counter (TEPC), can be detected, but placing such a detector directly in the proton beam will saturate the detector with primary protons. This makes interpretation of the signal from secondary HNR particles extremely difficult. Some measurements have been made in neutron therapy beams that reveal a significant dose contribution from heavy ions of LET $\geq$ 200 keV/μm [Fidorra et al., 1981]. In the case of neutrons, primary particles are not detected and the detector can be placed directly in the beam. The results at energies $\gtrsim$50 MeV from proton beams are expected to be similar.

Another area where the contribution of HNR particles to total dose is only partly known is in the radiation exposure of space crews [Benton et al., 2001a; Benton et al., 2006]. Astronauts in low Earth orbit (LEO) and on lunar or interplanetary missions receive a dose contribution from HNR particles due to the presence of protons in the Galactic Cosmic Ray (GCR) spectrum, trapped protons in the Van Allen belt, and protons in solar particle events (SPEs). The importance of absorbed dose from GCR primaries was recognized early in the space program [Benton et al., 1966]. The GCR spectrum consists primarily of protons, ~87%, which are peaked in energy between 1 to 10 GeV [Simpson, 1983]. In addition to GCR protons, the Earth's trapped radiation belts contain protons broadly peaked in energy between 10 and 250 MeV [NCRP, 1989]. SPEs release protons as well, generally with energies $\leq$ 200 MeV. Protons from these sources deposit energy, and therefore dose, primarily via electromagnetic interactions, but also have sufficient energy to produce HNR particles through nuclear target fragmentation reactions.

The dose component from secondary particles was first measured in PNTD on the Biosatellite III experiment [Benton et al., 1972]. Measurements on the Long Duration Exposure Facility (LDEF) found that proton-induced secondary particles were responsible for most of the of the high LET (> 100 keV/µm) component in low altitude, low inclination orbit [Benton et al., 1996a; Benton et al., 1996b; Nefedov et al., 1996]. TEPC measurements aboard the space shuttle have been made [Shinn et al., 1999; Singleterry et al., 2001], but due to detector cross-section, the LETs of these particles cannot be accurately measured. A comparison between active and passive detectors in LEO showed a loss of short-range, high-LET secondaries in passive detectors due to prolonged etching [Tawara et al., 2002]. Recent measurements, such as the Matroshka experiment on the International Space Station (ISS) [Reitz et al., 2009], in which a human torso phantom was used for quantitative dose determination in LEO, have also demonstrated the ability for naturally occurring, high energy protons to penetrate into the body and produce HNR particles.

1.1. Heavy Nuclear Recoil Formation

HNR particles are formed by nuclear collisions in a sequence of events first described by Serber [Serber, 1947]. The Serber, two-step nuclear reaction model was later experimentally verified by other investigators [Winsberg, 1980a; Cumming et al., 1981]. In the first step, a sufficiently energetic projectile nucleus ($\gtrsim$20 MeV), or single proton or neutron, has a small probability of undergoing a nuclear collision with a nucleus in the target matter. The nuclear collision may produce knock-out particles such as protons, neutrons and alpha-particles from the target nucleus, which are ejected rapidly as a result of nucleon-nucleon collisions inside the target nucleus in what is often called an intra-nuclear cascade (INC). This initial, pre-equilibrium step progresses rapidly, typically in less than 30 fm/c or ~ 10^{-22} s [Cugnon et al., 1997; Machner et al., 2006], which is on the order of the time it takes for the projectile particle to traverse the target nucleus.

After direct particle ejection in the first step, the remaining nuclear fragment is left in an excited state similar to that resulting from compound nucleus formation in lower energy nuclear reactions. This residual nuclear fragment undergoes nuclear evaporation to reach the ground state by emitting additional nucleons, photons, and perhaps other light particles. To conserve momentum during the evaporation step, the nuclear fragment recoils in the opposite direction to that of the evaporation particles; this is the heavy nuclear recoil (HNR) particle. The Serber two-step nuclear reaction model is sometimes referred to as the cascade/evaporation model in later literature.

HNR particles are formed by intermediate energy reactions occurring at energies between that of compound nucleus formation at low energies (~50 MeV or less) and spallation/completely direct interactions at high energy (~500 MeV or more). HNR particles typically have a range on the order of 1 to 10 μm in low Z materials [Winsberg, 1980b], although the actual particle range is density dependent. Note that this range is on a scale similar to the dimensions of biological cells, making the investigation of HNR particles relevant to proton cancer therapy, as well as to the radiation protection of space crews. In addition, if the target fragmentation occurs in CPU or other integrated circuit (IC) on an orbiting satellite or spacecraft, the HNR particle can affect the state of one or more discrete circuit elements leading to a fault. Detailed measurements of target fragmentation reactions are needed to evaluate total dose to patients receiving proton cancer therapy, astronauts during space flight, and to properly evaluate the challenges facing orbiting electronic systems.

1.2. HNR Particle Measurement Techniques

Various experimental methods have been used previously to study the HNR particle formation mechanism and the constituent properties HNR particles. The two most commonly used methods are the radiochemical technique [Winsberg et al., 1961] and photographic nuclear emulsions [Waddington et al., 1985; Bogdanov et al., 2005]. In the radiochemical technique, a stack of thin layers of material, one of which is of different composition (the target layer), are exposed to a beam of high energy particles. The target layer is typically in the center of the stack, with so-called catcher layers of low-Z material such as Mylar, extending outward along the beam direction on either side, as shown in Figure 2. During the exposure, projectile nucleons collide with the nuclei in the target. A fraction of the HNR particles formed in these target fragmentation interactions, travel out of the target layer and become embedded in one of the multiple catcher layers. Following beam exposure, the catcher layers are independently analyzed with radiochemical methods, such as ionization chamber counting and γ-ray spectroscopy using HPGe detectors or scintillation detectors, to determine both half-life and specific activity of specific HNR particles. This analysis determines the fraction of activated HNR particles deposited in the forward and backward directions, which can then be used to determine nuclear reaction kinematics [Winsberg, 1980a, 1980b].

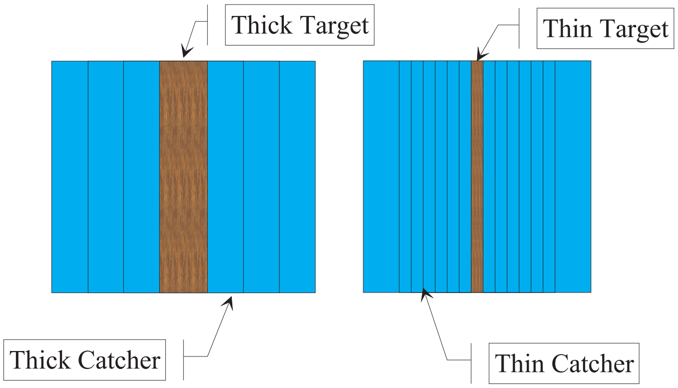

Figure 2. The thick-target/thick-catcher stack on the left is useful for determination of inelastic nuclear cross sections for various target materials. The thin-target/thin-catcher stack can be used to study reaction kinematics [Alexander et al., 1961; Winsberg, 1978].

A photographic nuclear emulsion consists of a solid substrate layer, such as glass, coated with a thin layer of silver halide of uniform grain size suspended in an emulsion. Passage of charged particles is detected by the change of state imparted during ionization of the silver halide grains, which is revealed after chemical development. Nuclear emulsions can detect singly ionized particles with minimum ionizing energy. This technology was the first to reveal the track structure of high energy particles and was used by Powell et al. in 1947 in the discovery of the pion [Lattes et al., 1947]. Photographic nuclear emulsions are exposed to high energy beams in a manner similar to that used in radiochemical methods, but detector processing is similar to developing photographic film. The exposed and developed emulsion is analyzed microscopically to study individual nuclear track details.

Although both methods are extremely useful tools, radiochemical methods are limited to the study of HNRs with sufficiently long radioactive half-lives for laboratory counting, while photographic nuclear emulsions are limited by the range of target nuclei available for interaction. Using radiochemical techniques or nuclear emulsions, it is possible to obtain detailed information about recoil kinetic energy, range, composition (Z), and reaction cross sections. However, they are not generally useful for measuring the dose from HNR particles in tissue.

Polyallyldiglycolcarbonate, or CR-39, plastic nuclear track detector (PNTD) is a passive detector sensitive to charged particles of LET in water between 5 and 1500 keV/μm [Benton et al., 1986]. Charged particles with an LET in this range produce latent damage in the detector along the particle's trajectory. Following irradiation, the PNTD is chemically etched, a process that transforms the latent damage trails into conically-shaped etch pits in the surface of the detector. The size of the elliptical opening of a conical etch pit, or nuclear track, is proportional to the LET of the charged particle that produced the damage.

Charged particles of LET < 5 keV/μm do not produce sufficient damage in CR-39 PNTD to yield etchable nuclear tracks. This includes primary protons of proton therapy beams at all depths with the exception of the Bragg peak, as well as the vast majority of energetic protons encountered during space flight. As a consequence, the nuclear tracks found in CR-39 PNTD exposed in the plateau of the Bragg curve, i.e. the region corresponding to healthy tissue in front of the tumor volume under treatment, are the result of nuclear interactions between the primary protons and the nuclei of the detector. The high LET tracks (≥250 keV/μm) are from particles formed in target fragmentation reactions between protons and the C and O nuclei of the CR-39 PNTD, and this includes tracks from HNR particles.

The minimum range of charged particles that can be measured in CR-39 PNTD is dictated by the thickness of the detector layer removed during chemical etching. In order to make tracks large enough to resolve by visible light microscopy, previous work carried out in our laboratory has shown that a minimum thickness of 8 μm must be removed [Benton et al., 2002b; Benton et al., 2006]. This means that particles with range shorter than 8 μm cannot be measured and, consequently, previous efforts to analyze the HNR particle contribution to dose have only included that fraction of HNR particles with range > 8 μm [Benton et al., 2001b]. To overcome this limitation, a method was required that permitted analysis of CR-39 PNTD that had only been etched to remove a much thinner layer (~1 μm) of bulk detector. Such a method is PNTD analysis using atomic force microscopy (AFM).

1.3. AFM Analysis of CR-39 PNTD

The application of AFM techniques to the study of nuclear track detectors closely followed the wide spread commercial availability of the AFM in the early 1990’s. The

AFM was first used on nuclear track detectors to study track evolution in mica [Price, 1993]. Analysis of polymer materials was greatly enhanced with the development of tapping mode AFM [Magonov et al., 1997]. AFM methods have also been used to provide a new means of direct bulk etch measurement [Yasuda et al., 1998] that is applicable for shorter etch times. The key feature of this early AFM work with CR-39 PNTD is that it focused on track specific characteristics using local measurements. Methods were still needed to enable the large area measurements of large numbers of tracks necessary to obtain statistically significant, quantitative data with the AFM.

Our research group's early work in this area, based on experiments conducted at the Loma Linda University Medical Center (LLUMC) Proton Therapy Facility [Benton et al., 2001b], as well as data collected in LEO on the Mir space station [Benton et al., 2002b, 2002a], were an attempt to adapt the AFM to large area measurements to obtain LET spectra. This work represented a successful evaluation of the measurement principles previously mentioned and produced the first LET spectra in CR-39 PNTD using AFM. However, the scope of this early method was limited due to the rudimentary nature of the analysis tools then available. A dedicated effort was needed to develop the quantitative analysis tools necessary to fully apply AFM based methods to large area analysis of CR-39 PNTD.

Because AFM provides a 3-D topographical map of the post-etch PNTD surface, there is a fundamental difference between AFM data and the data contained in a standard image of the post-etch CR-39 PNTD surface obtained using an optical microscope and CCD camera. The key feature of AFM data is that it represents a surface deterministically, unlike optical microscopy in which many surface features can yield the same gray scale value. As documented in this thesis, a method based on large area, automated AFM scanning followed by 3-D matrix analysis (as opposed to image processing), has been developed which allows quantitative, reproducible measurement of the dimensions of individual nuclear tracks. This new analysis method isolates data points from the individual nuclear track on a post-etch detector surface and then applies an ellipse-specific least squares fitting [Halíř et al., 1998; Fitzgibbon et al., 1999] to determine the track's geometrical parameters, followed by a gradient weighted estimate of fit (EOF) [Rosin, 1996]. The EOF calculation provides a useful metric for ellipse fit accuracy and has also proven to be useful for separating overlapped tracks from one another. The track geometry provided by this method is more accurate than previous approaches and the method is also amenable to automation.

This work represents a significant advancement in AFM/CR-39 PNTD analysis methods as illustrated by its application to LET spectra measurements for various thick-target/thick-catcher type experiments. In irradiations conducted at LLUMC and the NASA Space Radiation Laboratory (NSRL) at Brookhaven National Laboratory (BNL), targets of varying composition, including a number of elemental targets of high Z, were exposed in contact with layers of CR-39 PNTD to beams of 60 MeV, 230 MeV, and 1 GeV protons at doses between 2 and 50 Gy. Additionally, the least shielded (<0.05 g cm^{-2}) external detector on the International Space Station (ISS) Matroshka experiment was analyzed using the new methods. The results of our analysis of these experiments with AFM demonstrate the efficacy of the new analysis method and open the way to new applications of CR-39 PNTD in studying the physics of HNR particles and to measuring the space radiation environment on the exterior of spacecraft.

The analysis of CR-39 PNTD using optical microscopy is time consuming and the AFM methods presented in this document offer no improvement in this respect. Additionally, there are limitations on the measurement capability of AFM that restrict the range of particle LET measurements depending on the size of the scan area. This implies that a range of scanning regimes is needed to obtain the full LET spectrum, a fact that further increases AFM scan time. The principal advantage of our new method is that the quantitative data obtained regarding short-range, high-LET nuclear tracks allows us to directly measure the contribution from HNR particles to total absorbed dose.

In Chapter II of this document, I discuss the nuclear physics relevant to the HNR particle production mechanism and review previous work related to the study of HNR particles. Chapter III of this work describes the use of CR-39 PNTD in beam experiments and space exposures, and particularly its application to the study of HNR particles. An overview of AFM and the scanning techniques used in this work are discussed in Chapter IV. Chapter V describes the work carried out in developing methods to quantitatively analyze AFM data from CR-39 PNTD, including a discussion of the algorithms developed for this work. The experimental methods developed for this work are discussed further in Chapter VI, including the results of accelerator-based experiments demonstrating the AFM analysis methods developed during this project. The results of external spacecraft experiments using CR-39 PNTD are presented and discussed in Chapter VII, followed in Chapter VIII by conclusions and suggestions for future work.

CHAPTER II

THE FORMATION OF HEAVY NUCLEAR RECOIL PARTICLES

Nuclear interactions have been studied for 100 years, beginning with Geiger and Marsden's observation of α-particle scattering at large angles from gold foil in 1909 [Geiger et al., 1909]. Following these early experiments with low energy particles, particle accelerator technology emerged, increasing our capacity to study the nucleus by providing a broad range of beams with a wide variety of particle/energy combinations.

Particles that comprise the beam are referred to herein as projectile nuclei, or simply projectiles and the constituent nuclei of the target material placed in the beam are referred to as target nuclei. Particles formed in target fragmentation reactions are referred to as secondary particles. Projectile nuclei are assumed to be completely ionized and target nuclei are assumed to have all electron orbitals filled and to be at rest in the laboratory frame of reference. These assumptions have limitations in the case of heavy ion beams ($Z > 1$); it is known that charge accumulation occurs in a stochastic manner during the projectile's transit through target matter. Assuming target nuclei to be at rest completely neglects thermal motion, but since this velocity is small by comparison to the beam energy the assumption remains valid. In this work, projectiles are usually protons.

Projectile nuclei interact with matter through electromagnetic (ionization and excitation of atomic electrons in a medium) and elastic/inelastic nuclear collision processes. This discussion begins with the properties of electromagnetic interactions followed by a review the general characteristics elastic and inelastic nuclear collision processes pertinent to the range of projectile energies used in this work. For a more detailed discussion of the nuclear physics of medium energy nuclear reactions, the interested reader is referred to the excellent reviews of [Lynch, 1987; Viola et al., 2006] and references therein. The production and detection of HNR particles is addressed in this chapter, as are the implications for dose deposition, both in proton radiotherapy and for astronauts.

2.0 Electromagnetic Interactions

Throughout the entire range of primary particle energies, energy transfer occurs through collisions between the projectile and the orbital electrons of the target. This often results in the ionization and subsequent ejection of electrons at high velocity. The large scale transfer of energy from the projectile to the atomic electrons is described by the Bethe-Bloch formula using the continuous slowing down approximation (CSDA). The characteristic pattern of energy deposition with respect to depth (usually expressed in g/cm^2 or in cm of a given material such as water) is known as the Bragg curve (see Figure 1). The ionization of electrons represents the primary mode of energy transfer in the Bragg peak; however in the plateau of the Bragg curve, including the region immediately before the Bragg peak, nuclear interactions can contribute significantly to energy deposition, and therefore to the dose delivered in tissue.

2.1. Nuclear Interactions

For energetic projectiles passing through normal matter, there is always some probability of nuclear interaction. At low energy, ≤1 MeV for protons, these interactions are dominated by elastic scattering reactions with the nuclear and coulomb potentials of target nuclei [Cork et al., 1957; Glassgold, 1958; Hess, 1958]. Nuclear reactions in this energy range can be successfully described by the optical model [Satchler, 1967]. As the energy of the projectile increases, the Coulomb barrier of the nucleus is overcome and the projectile has an increased probability of penetrating the nucleus. Provided the energy is not too high (≲20 MeV, target nucleus dependent), the projectile collision with a target nucleus may result in the formation of a compound nucleus [Ghoshal, 1950; Williams et al., 1967]. The compound nucleus is usually in an excited state and may eject photons or nucleons by what is called nuclear evaporation to reach the ground state.

As proton energy is further increased (≳20 MeV), there is an increasing probability of inelastic nuclear collisions resulting in the emission of multiple secondary particles from the nucleus during a short period of time immediately following the nuclear collision. For this class of reactions, there are numerous possible outcomes with respect to secondary particle emission; multiple protons and/or neutrons, as well as individual or multiple α-particles and other light nuclei may be ejected in various combinations.

2.1.1. Two Step Nuclear Reaction Model

The first and still highly applicable model for this type of inelastic nuclear collision process was proposed by Robert Serber in a short letter to *Physical Review* [Serber, 1947]. The Serber model is often referred to as the “two-step” model in the literature and was later refined into the cascade/evaporation model [Harp et al., 1968; Cugnon, 1987] and the pre-equilibrium model [Blann, 1971; Blann, 1972]. In the first step of the two-step model, the projectile nucleus collides with a target nucleus (which is considered at rest), resulting in the emission of knock-out particles from the target. The residual nuclear fragment attains forward momentum in the beam direction and is left in an excited state. In the second step of the two-step model, the residue of the initial target nucleus is said to reach equilibrium, since the constituent nucleons of the residual fragment equally share the remaining kinetic energy imparted in the first step. As in de-excitation of compound nuclei, the nuclear fragment then undergoes nuclear evaporation until nuclear stability is achieved. To conserve momentum, the residual nucleus recoils during evaporation, in a direction opposite to that of the evaporation nucleons and light particles.

In the first step of the nuclear reaction, the nucleons exchange energy in what is referred to as the intra-nuclear cascade (INC) [Bertini, 1963]. The nucleons of the target nucleus following a nuclear collision have been described previously as participants and observers [Malfliet, 1981]. The nucleons affected by (or involved in) the INC, are known as participants. The remaining nucleons present, e.g. those that are not directly involved in the INC, are referred to as observers. Participant nucleons may acquire sufficient energy to leave the nucleus. The ejected nucleons and clusters of nucleons released in the INC are mainly emitted in the direction of the primary projectile. The particle ejection associated with the first step of the reaction occurs rapidly. Recent observations indicate that the time scale for these fast, pre-equilibrium emissions is $\leq$ 30 fm/*c* (~10^{-22} s) [Ginger et al., 2008].

As a result of the nuclear collision in the first step, a velocity, **v**, is imparted to the target nucleus. The amount of forward momentum imparted to the target nucleus depends on various factors, such as impact parameter and the masses of the target and projectile nuclei. The momentum transferred to the target nucleus generally decreases with projectile energy [Winsberg, 1980b].

Following the INC, the excitation energy of the nuclear collision is redistributed equally between the remaining nucleons in what is referred to as nuclear equilibrium. In the second step of the Serber two-step model, the residual target nucleus as a whole may be in an excited state and will then undergo nuclear evaporation to reach the ground state. Analogous to compound nucleus decay, nuclear evaporation may include the ejection of multiple nucleons and to conserve momentum, the target residual nucleus recoils in the appropriate direction. The HNR particle composition depends primarily on target Z and A and on the kinetic energy imparted by the projectile in the first step.

The heavy nuclear recoil (HNR) particle is known to have a Maxwellian velocity distribution and can be emitted in any direction [Winsberg, 1964]. The distribution of HNR momentum is considered isotropic based on the fact that all information about the initial collision event was lost during redistribution of nucleon energy following the first step. The recoil velocity of the residual nucleus in the second step is denoted **V**. Since the evaporation stage occurs following equilibrium, there is no preferred direction for **V** and it is considered isotropic. **V** in general, can be greater than **v**; therefore HNR particles can be detected that have traveled in a direction opposite to that of the projectile beam. An illustration of the velocity imparted to the target nucleus is shown in Figure 3.

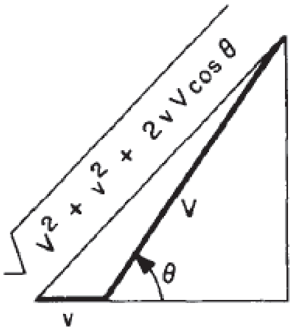

Figure 3. The two-step nuclear reaction model, originally proposed by Serber [Winsberg, 1980a]. In the first step, a velocity **v** is imparted to the target nucleus, and in the second step, following nucleon evaporation, the recoil velocity **V** is imparted to the residual nucleus.

In modeling nuclear collision processes (numerous Monte Carlo methods exist); the two steps are handled separately, with one routine performing the intra-nuclear cascade step and another performing the equilibrium/evaporation calculations. An attempt to clarify the overlap between the two steps has been tried by inserting a step that specifically addresses the nuclear pre-equilibrium condition [Cugnon et al., 1997]. This approach has had mixed results and introduces unnecessary complication, and the Serber two-step model has remained the predominant view applicable to this work.

2.2. HNR Particle Detection

The detection of HNR particles is difficult because these particles have extremely short-range in matter. HNR particles typically have a range less than 20 µm. For an active detector, an HNR particle is unlikely to penetrate through protective materials into the sensitive volume of the detector. Existing techniques for detecting HNR particles include radiochemical analysis [Miller et al., 1959], photographic nuclear emulsions [Beiser, 1952], charged particle telescopes and telescope arrays (when coincidence methods are used) [Viola et al., 2006], as well as nuclear track detectors [Benton et al., 2001b]. Each of the detection methods mentioned above has strengths and weaknesses.

2.2.1. Radiochemical Methods

Radiochemical analysis has been used to study the nuclear reaction mechanism by analyzing HNR particle formation and deposition by various investigators [Alexander et al., 1961; Winsberg, 1978]. Radiochemical methods are applied in two types of experiments: thick-target/thick-catcher experiments and thin-target/thin-catcher experiments. An example of a thick-target/thick catcher experiment, which is similar to the detector assemblies used in this work, is shown in Figure 4.

In this method, layers of Mylar, or another low-Z material are used on both sides of a target layer and the all the layers are held in intimate contact in a stack. This stack is then exposed to a particle beam. HNR particles formed by the beam interaction with nuclei in the target then travel both forward and backward out of the target layer. The activity, A, of radioactive HNR particles in the front layer, A_F, and back layer, A_B, is then measured in a low-background counting facility. The ratio of front to back activity can then be used to determine the kinetic energy distribution for the HNR measured. This method can only be used for HNR particles that have a sufficiently long radioactive half-life for handling and counting purposes.

The radiochemical analysis method can be illustrated by the proton-induced recoil reaction $Al^{27}(p, 3pn)Na^{24}$ with proton energy 2.9 GeV. In this reaction Na^{24} is formed as a result of the second step in the Serber model; it is a HNR particle and can be emitted in any direction. Na^{24} is a radioactive isotope with a 14.86 hr half-life that emits 1.3 MeV gamma-rays. Since the Mylar catcher film has no Na^{24} present prior to the experiment and none of its constituent nuclei can form Na^{24}, one can have reasonable certainty that the Na^{24} activity measured after beam exposure is solely due to HNR particle deposition. As shown in Figure 3, the momentum transfer in the first step of the collision imparts a velocity, $\mathbf{v}$, in the forward direction. In the second step nuclear evaporation occurs, which imparts a velocity, $\mathbf{V}$, to the residual nucleus (now Na^{24}). The final velocity of the Na^{24} nucleus is the vector sum of $\mathbf{v}$ and $\mathbf{V}$. Since $\mathbf{v}$ is both forward peaked and non-zero there is a higher final activity, A_F, measured in the forward direction than in the backward direction. However, the magnitude of $\mathbf{V}$ can be greater than the magnitude of $\mathbf{v}$, resulting in substantial activity, A_B, measured in the backward direction as is shown in Figure 4.

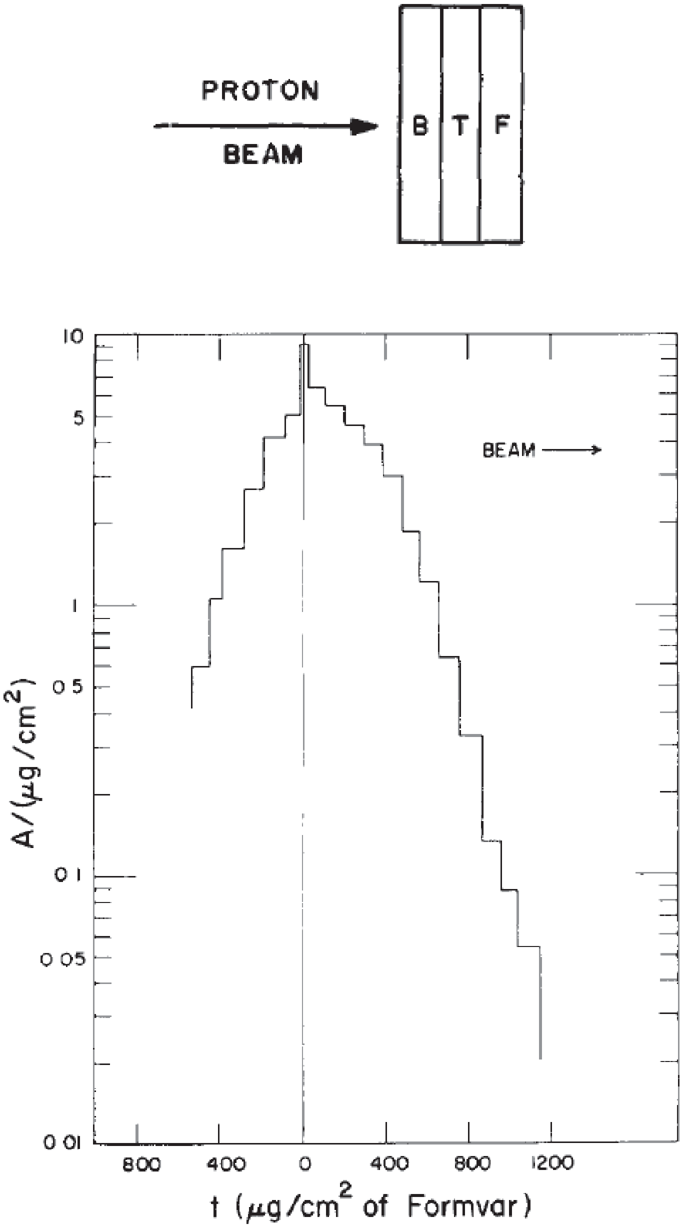

Figure 4. The upper diagram shows an example thick-target/thick-catcher experiment, the plot at bottom shows a typical analysis for a thin-target/thin-catcher type of experiment [Winsberg, 1978]. The reaction studied was $Al^{27}(p, 3pn)Na^{24}$ with 2.9 GeV proton energy. The vertical axis, A, is activity of Na^{24} .

Since radiochemical methods are only applicable for HNR particles with suitably long half-lives, they do not have the capability to provide information about the distribution in

Z of HNR particles formed in a given target. Additionally, a large dose of primary beam particles is needed for the exposure and since the half-lives of many possible HNR particles are short, considerable space and equipment are required at the beam facility to conduct these experiments.

The primary advantage of the radiochemical method is that it is based on direct measurements of many HNR particles. The detector stack used for this method is designed for placement in the primary ion beam, while active detectors used for HNR particle detection are saturated by beam signal if they are placed in this location.

2.2.2. Photographic Nuclear Emulsions

A photographic nuclear emulsion consists of a layer of silver halide emulsion deposited uniformly on a glass substrate. Similar in function to camera film, a photographic nuclear emulsion is developed following beam exposure. During exposure to an energetic particle beam, the primary ions undergo nuclear collisions with the nuclei present in the emulsion. Both primary beam particles, secondary particles formed from inelastic nuclear collisions, and secondary electrons (δ-rays) can leave nuclear tracks that are revealed in the development process. These tracks are then analyzed microscopically to reveal the properties of the particles that caused the tracks.

An advantage of this method is that it records individual tracks formed in inelastic processes, allowing detailed study of secondary particle trajectory, energy, and composition. Information from multiple layers of emulsion can be used together to reconstruct the features of individual events. This method has been applied to many experiments in nuclear physics, notably the experiments with energetic protons and neutrons [Bernardini et al., 1952]. The application of photographic nuclear emulsions is limited by the range of target Z elements that exist in the emulsion, primarily Ag, and halides, like Br, and by the time required for detailed analysis. Additionally, photographic nuclear emulsions are not useful for tissue equivalent dose measurements.

2.2.3. Active Detection

Active detectors have difficulty with HNR particle measurement, but techniques exist to infer the formation of an HNR particle. The types of active detectors used to indirectly detect HNR particles include magnetic spectrometers, tissue equivalent proportional counters (TEPC), and charged particle telescope arrays. A charged particle telescope consists of multiple active detectors used in coincidence to obtain particle information. As an example of a particle telescope are two thin silicon detector layers and a thick scintillator detector placed in a linear arrangement. If a high-energy, charged particle passes through the two silicon detectors, a coincidence gate signal is generated and the output of the scintillator is monitored. This arrangement allows for the rejection of noise pulses caused by other particles. For a large enough scintillator, the charged particle is likely to stop in the material. This provides an output signal that is proportional to the particle’s energy.

With an array of detectors it is possible to time resolve the arrival of particles and reconstruct the nuclear collision event. This reconstruction can be used to infer the formation of the HNR particles from the presence of knock-out protons and intermediate mass fragments (IMF) formed in the first step, and the presence of evaporation protons emitted in the second step. The HNR particle is not measured directly since this would require placing a sensitive active detector directly in the primary ion beam. Research using active detection methods has been primarily focused on the formation and detection of light charged particles and IMFs [Geissel et al., 1992; Viola et al., 2006; Ginger et al., 2008]. Active detector systems have the disadvantage that they are expensive.

2.2.4. Nuclear Track Detectors

It has been previously shown that CR-39 PNTD is capable of detecting short-range, high-LET HNR particles encountered in spaceflight [Benton et al., 2002a] and in proton therapy beams [Benton et al., 2001b] using a short duration chemical etching followed by AFM analysis. This pioneering work established the AFM as an alternative to OPT methods and is well suited to the measurement of CR-39 PNTD exposed to fluences in excess of 10^5 cm^{-2} and for charged particles with range ≤8 μm. The work described in this document reports recent improvements to the AFM analysis methods previously used.

2.3. HNR Particle Contribution to Dose

There is currently no means of directly measuring the dose to tissue due to secondary HNR particles formed in inelastic nuclear collision processes. Instead, computer modeling is used to estimate this dose. The method used to model dose delivered during proton radiotherapy uses a Monte Carlo simulation, e.g. GEANT3/4 or FLUKA

[Gottschalk et al., 1999; ICRU, 2000; Paganetti, 2002]. The treatment of HNR particle dose, which is expected to be small, compared to the primary beam dose, is based on the assumption that HNR particles deposit their energy at the point of formation and is not explicitly calculated over the HNR particle's range.

Gottschalk measured the charge deposition of secondary particles using a Cu/Kapton multi-layer Faraday cup (MLFC) in a 160 MeV proton beam [Gottschalk et al., 1999]. These results were compared to the results obtained using the FLUKA radiation transport code and reasonable agreement was found. However, this result can be considered a confirmation of the physics models of the transport code rather than as an accurate dose measurement.

CHAPTER III

CR-39 PLASTIC NUCLEAR TRACK DETECTOR

Polyallyldiglycol carbonate ($C_{12}H_{18}O_7$) is a thermoset crosslinked polymer that is commercially available under the trade name CR-39. CR-39 has characteristics that make it useful as a plastic nuclear track detector (PNTD) [Cartwright et al., 1978; Cassou et al., 1978]. CR-39 PNTD is optically transparent, homogenous, and sensitive to charged particles with $LET_{\infty}H_2O$ in a range between 5 keV/µm and approximately 1500 keV/µm. The formation of nuclear tracks by charged particles is discussed in this chapter, as well as limitations in the analysis of CR-39 PNTD when using optical microscopy.

In addition to CR-39 PNTD, there are many other materials useful as solid state nuclear track detectors, e.g. Lexan, mica, cellulose nitrate and cellulose acetate. Each type of track detector material has a minimum LET sensitivity threshold and a maximum LET threshold. Nuclear track detectors do not record damage due to gamma radiation or electrons. Track registration lower LET thresholds, sensitive LET ranges, and track evolution properties vary among the different detector types; a general discussion of these features is beyond the scope of the present work, but is well documented in the literature [Fleischer et al., 1964, 1967; Katz et al., 1968; Fleischer et al., 1975].

3.0 Nuclear Track Formation

A solid state nuclear track detector (SSNTD) is a dielectric solid that records the passage of charged particles. As a charged particle passes through CR-39 PNTD, the chemical bonds between its constituent atoms are broken. A latent damage trail, consisting of broken chemical bonds, is formed along the path of the charged particle as illustrated in Figure 5. A chemical etching process is used to enlarge the latent damage trail to a size that can be measured by optical microscopy or atomic force microscopy.

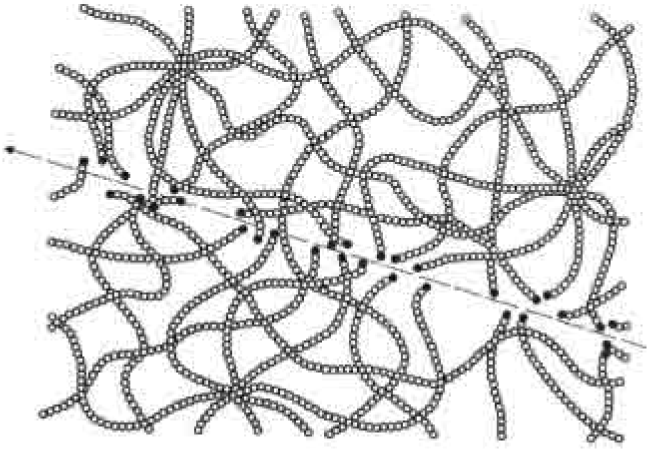

Figure 5. A charged particle, entering CR-39 PNTD at the lower-right, interacts with orbital electrons in the detector thereby breaking chemical bonds between molecules, leaving a latent damage trail along its path [Durrani et al., 1987].

In experimental applications, CR-39 PNTD is exposed to a radiation field and then subjected to chemical etching by 6.25 N NaOH, maintained at 50°C. The etching process enlarges the nuclear tracks (latent damage trails) to a size suitable for analysis, usually with an optical microscope. Following the etch period, the value of bulk etch, *B*, the thickness of bulk detector removed by chemical etching, is determined [Henke et al., 1986].

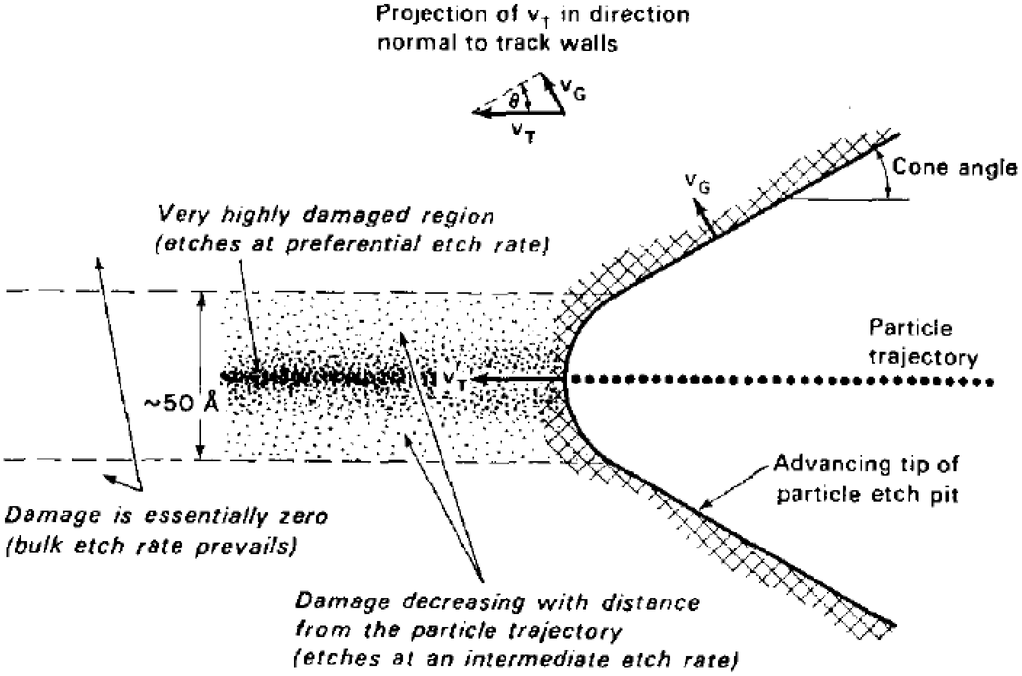

Figure 6. As chemical etching progresses, the latent damage trail is etched preferentially and a track cone is formed on the surface of the detector (figure from [Henke et al., 1971]).

The post-etch appearance of a nuclear track is that of an inverted cone, which intersects the surface with some dip angle, δ. The surface intersection of this cone can be circular ($\delta = \pi/2$) or elliptical ($0 < \delta < \pi/2$) [Henke et al., 1971; Somogyi et al., 1973; Somogyi, 1980]. The interior surface of the track cone is smooth and the tip of the track is pointed. The physical size of the track cone is proportional to the particle LET. Optical analysis methods (OPT) for CR-39 PNTD involve the manual or semi-automated scanning of a large surface area of the exposed detector followed by analytical interpretation of the dimensions of the nuclear tracks present in each field of view.

Chemical etching results in the bulk of the detector being chemically removed into solution at a rate, V_G, called the bulk etch rate. The bulk etch rate, V_G, depends on the properties of the chemical etch used, including temperature and chemical composition and concentration, as well as the properties of the detector material. For an etchable track (LET > 5 keV/μm for CR-39 PNTD), the track etch rate, V_T, the rate at which the latent damage trail reacts and is removed by chemical etchant, is greater than the bulk etch rate and varies with the LET of the charged particle that formed the latent damage trail. The inset at the top of Figure 6 illustrates the relationship between bulk etch rate, V_G, track etch rate, V_T, and cone angle θ, for a nuclear track. The bulk etch rate, V_G, is normal to the track cone surface, and leads to the relation:

$$\sin\theta = \frac{V_G}{V_T}. \tag{3.1}$$

The reduced etch rate ratio, V_R, is defined as the ratio, V_T/V_G, so that equation (3.1) can be rewritten as:

$$\sin\theta = \frac{1}{V_R}. \tag{3.2}$$

Empirically, the quantity V_R is found to be proportional to charged particle LET and is the primary variable of interest in nuclear track measurements with CR-39 PNTD. In theory, a measurement of the cone angle, θ, would be useful to calculate V_R, but there is no direct means by which to make such a measurement.

3.1. Nuclear Track Geometry

As illustrated in Figure 7, the post-etch appearance of a nuclear track is that of a conical etch pit with an elliptical or circular opening at the surface of the detector. For increasing particle LET, the size of the etch pit increases. Interpretation of the post-etch nuclear track and the properties of its elliptical surface intersection are required to determine the charged particle LET. In reference to Figure 7, the semi-major axis, *a* and the semi-minor axis, *b* are measured quantities for which the following relations hold [Henke et al., 1971]:

$$a = \frac{B\cos\theta}{\sin\delta + \sin\theta}, \tag{3.3}$$

and,

$$b = B\left[\frac{\sin\delta - \sin\theta}{\sin\delta + \sin\theta}\right]^{1/2}, \tag{3.4}$$

where δ is the dip angle and θ is the cone angle. The measured values of *a* and *b*, are used to calculate V_R in the relation [Benton, 2004]:

$$V_R = \sqrt{1 + \frac{4\left(\frac{a}{B}\right)^2}{\left[1 - \left(\frac{b}{B}\right)^2\right]^2}}\ . \tag{3.5}$$

For circular track cones, e.g. *a* = *b*, equation (3.5) reduces to the form:

$$V_R = \frac{1 + \left(\frac{a}{B}\right)^2}{1 - \left(\frac{a}{B}\right)^2}\ . \tag{3.6}$$

The track length, L_R, after etch time, t, can be expressed as:

$$L_R = \int_{t_0}^{t} V_T \, dt \, . \tag{3.7}$$

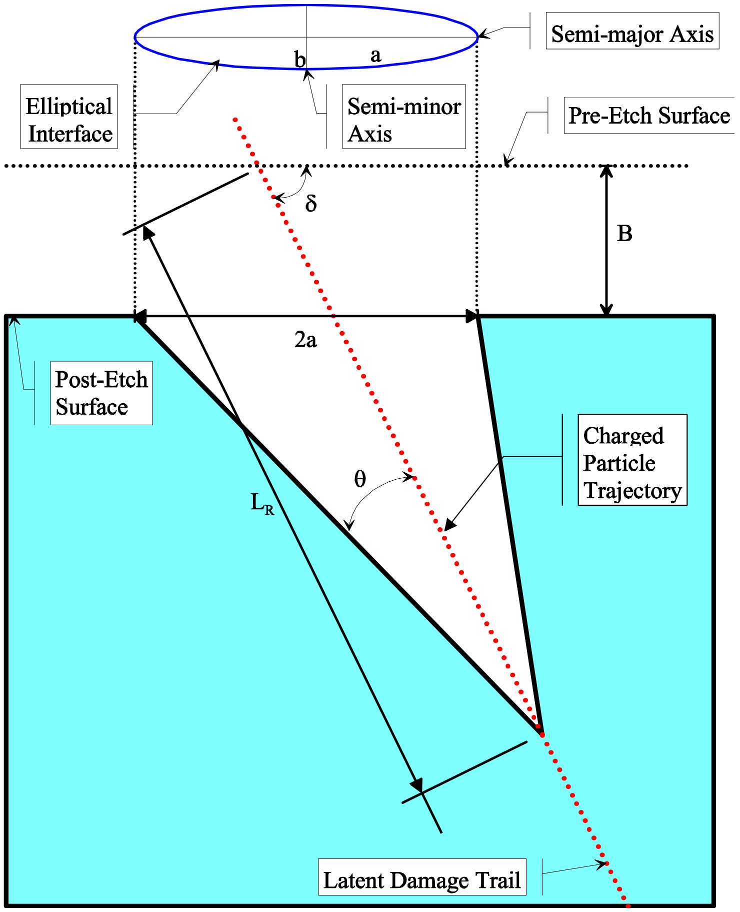

Figure 7. Profile of an etched nuclear track cone intersecting the planar surface of the detector with an elliptical opening. The physical measurements of a and b, are needed to calculate V_R.

Since charged particle LET, in general, is not constant as it passes through the detector (LET increases as particle energy is lost in the detector), the track etch rate, V_T, and track cone angle θ, could be expected to vary along the trajectory of the charged particle. In this work, the assumption is made that charged particle LET does not change appreciably as it passes through the bulk etch layer of CR-39 PNTD and that measured tracks are conical in shape with straight track cone walls, as opposed to curved walls in the case of changing LET. For charged particles in the plateau of the Bragg curve, the LET (and therefore θ and V_R) do not change rapidly. Additionally, since the layer removed by etching is typically small, charged particle LET does not vary much over such a short scale.

3.2. Bulk Etch Determination

The bulk etch, B, is obtained from the equation:

$$B = \int_{t_0}^{t} V_G dt \ , \tag{3.8}$$

where t_0 is the etch start time, t is the etch stop time, and V_G is the bulk etch rate. For a homogenous detector material and constant etch conditions, the bulk etch rate is a constant and equation (3.8) can be rewritten:

$$V_G = \frac{B}{t} \ . \tag{3.9}$$

Since it is not possible to measure V_G during the etching process, B is determined by direct measurements after etch completion.

Following the chemical etch, the bulk etch, B, must be measured for use in equation (3.5). For the OPT analysis method, the standard means to determine B is the Henke–Benton method [Henke et al., 1986]. This etch determination method requires accurate measurements of detector mass, m_1 and m_2, before and after chemical etching, respectively, as well as surface area, A, perimeter, P, and mean thickness, t, after etching. These measurements are used in the formula:

$$B = \frac{(m_1 - m_2)t}{2m_2}\left[1 - \frac{Pt}{2A}\right]. \tag{3.10}$$

For AFM analysis of CR-39 PNTD, the Henke-Benton method fails to perform well for calculation of B. For short duration chemical etching, the difference between detector masses, m_1 and m_2, before and after chemical etching, are on the order of measurement error in mass. Another method was developed [Yasuda et al., 1998] for direct bulk etch measurement using AFM, and is discussed further in Chapter 4. This is the bulk etch determination method used for the detectors analyzed in this work.

3.3. Etch Parameters for OPT and AFM

In order to study short-range, high-LET tracks in CR-39 PNTD, the bulk etch must be limited to a value that will preserve these tracks for analysis. Standard methods of analysis using optical microscopy [Nikezic et al., 2004] require a long duration chemical etch to achieve ~40 μm bulk etch. This amount of etch will remove many short-range tracks of interest. To preserve the short-range tracks, a 0.5 μm bulk etch could be used, but this would leave tracks too small to evaluate with optical microscopy methods. To overcome this problem AFM is used to analyze the etched detectors. Following a 0.5 μm etch, the post etch track dimensions are on the order of a few hundred nanometers, a scale well within the measurement resolution of AFM.

3.4. Sources of Error Related to Prolonged Etch Duration

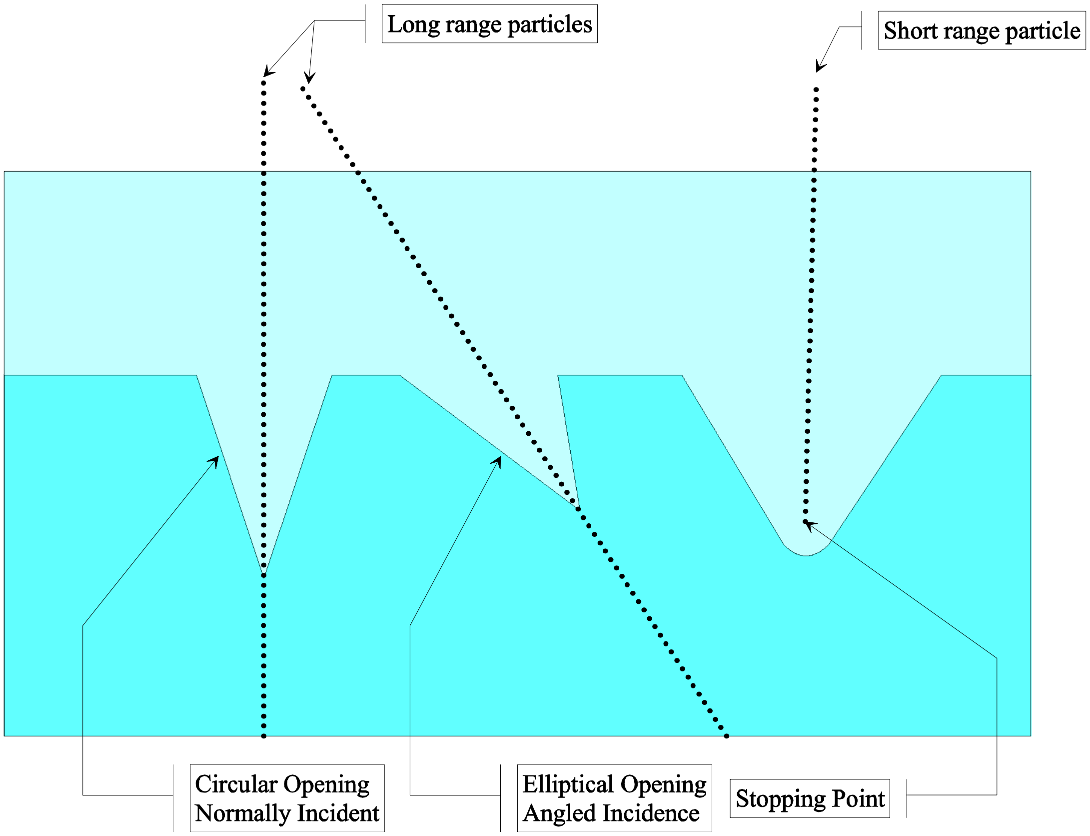

Figure 8. Variety of nuclear track cones formed by charged particles that originated outside the CR-39 PNTD sensitive volume. The track on the right is over-etched since the particle stopped in the region of detector removed by chemical etching.

As chemical etching progresses past the stopping point of a charged particle’s trajectory, the track etch rate is reduced to the bulk etch rate, and the shape of the track cone attains a circular shape. If etching progresses further, the track can become over-etched. Over-etched tracks are more difficult to analyze correctly than normally etched tracks and this is a source of analytical error. An example of an over-etched track is shown in Figure 8. For a given bulk etch value, it is possible to completely remove tracks that have a track length shorter than the bulk etch. The net effect of removed tracks is that the measured particle fluence on the surface of the detector is lower than the fluence due to the actual conditions of the experiment.

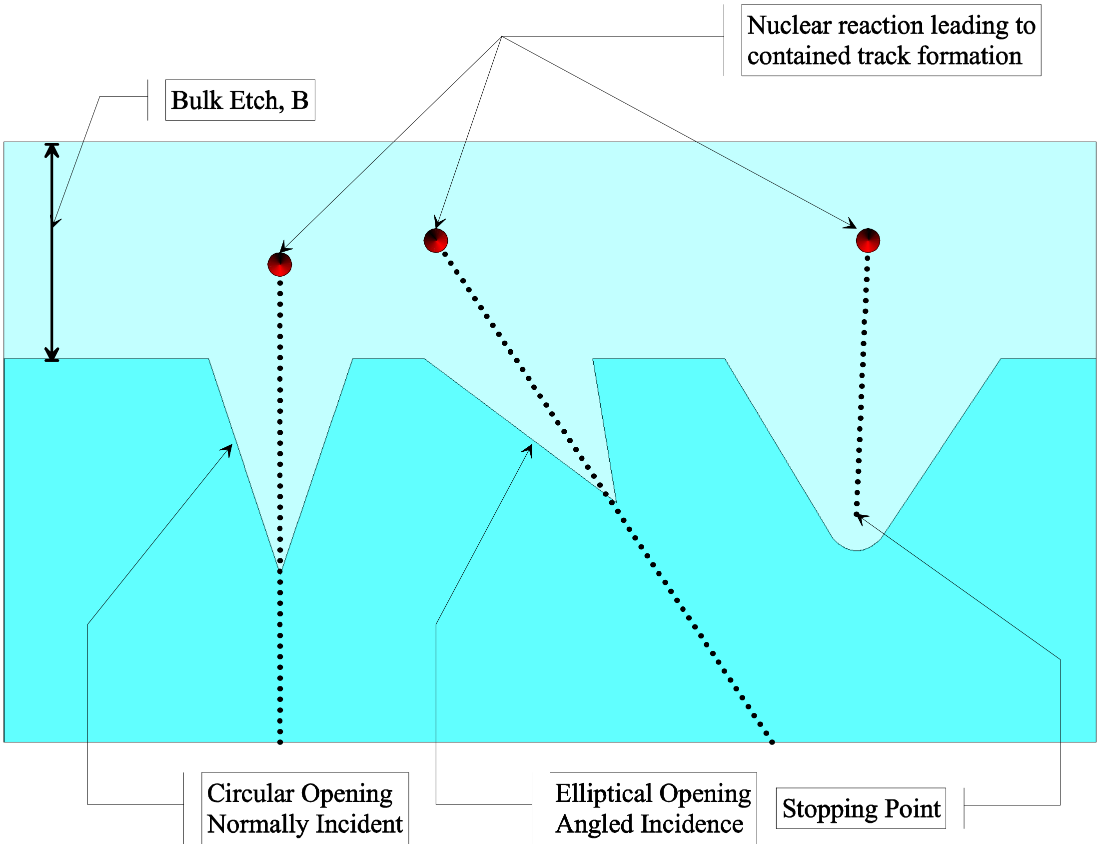

Figure 9. Nuclear track cones formed by contained events. In general, it is not possible to distinguish between contained and non-contained tracks. By limiting the bulk etch value, the possibility of etching a contained track is reduced, thereby improving experimental accuracy.

Overlapped tracks form when two unrelated nuclear tracks are etched past the point of track cone intersection, when one track cone merges with another. As the length of chemical etching increases, the number of overlapped tracks will increase for a given set of experimental conditions. Overlapped tracks are more difficult to interpret and can introduce additional error. The appearance of overlapped tracks imposes particle fluence limitations on the analytical methods used to analyze the post-etch surface of the PNTD.

Contained tracks present another source of error in CR-39 PNTD analysis. A contained track is formed when a target fragmentation reaction occurs inside the layer of CR-39 PNTD removed by chemical etching, rather than in the target layer under scrutiny in the experiment. As the bulk etch, *B*, is increased, there is an increased likelihood of encountering contained tracks, as shown in Figure 9.

3.5. Advantages and Limitations of CR-39 PNTD

Once exposed and etched, CR-39 PNTD serves as a stable record of ionizing radiation exposure that will not lose accuracy over time, provided the detectors are stored properly. Exposed detectors can be analyzed repeatedly without degradation. As technology progresses, the detectors can be re-read to obtain a more detailed analysis.

The CR-39 PNTDs used for astronaut dosimetry are low-cost, low mass, and have a small footprint and can easily be worn by space crew members. When used in combination with thermoluminescence detectors or optically stimulated luminescence detectors total dose and dose equivalent received during a space mission can be determined.

There are some active detectors that provide broad spectrum LET measurement capabilities, including the TEPC. However with these instruments, power requirements and data storage are additional concerns. No power is required for CR-39 PNTD operation and the analysis can be done at some later time.

CR-39 PNTD has the advantage that it functions best in accelerator experiments when placed directly in the primary beam with normal incidence angle. Most active detectors used for measurement of secondary particles cannot tolerate direct beam exposure at the intensity used in proton therapy and must be placed off-axis to avoid saturation. Other active detectors that are designed for beam monitoring, e.g. parallel plate ionization chambers, do not provide detailed information about individual particles.

When using CR-39 PNTD for dosimetry or an experiment, there is no time resolution regarding when the ionizing particles reached the detector. This is a distinct disadvantage of passive detectors, in general, as compared to active detectors. In experiments in which real-time coincidence information is needed, an array of active detectors must be used.

Another limitation of SSNTDs is that for track registering charged particles, a determination of the charged particle properties requires detailed analysis of the track cone. Since different combinations of Z and energy can have the same LET, it is difficult to use a track detector as a spectroscopy tool in a mixed field environment. Under certain circumstances, the precise direction of travel of a charged particle may be determined if an analysis of the track cone is sufficiently detailed to resolve the interior curvature of the cone.

3.6. Dosimetric Quantities

The near tissue equivalence of CR-39 PNTD when used for dosimetry measurements is a distinct advantage over other detection systems, which require careful calibration and conversion to provide a tissue equivalent dose measurement capability. As described in the previous sections, the analysis of CR-39 PNTD involves measurement of the post-etch properties of elliptical etch pits, which are used to calculate the LET of the charged particle that caused the track. The completed analysis includes a range of LET values obtained from each measured nuclear track within a given area on a detector. The measured LET values, taken together, form the LET spectrum. The LET spectrum is often the desired result for a given set of experimental conditions and can be used to calculate other quantities of interest, such as absorbed dose and dose equivalent.

3.6.1. Fluence

Particle fluence, Φ, is defined as the number of particles, dN, that cross a planar surface with area, dA [ICRU, 1998]:

$$\Phi \equiv \frac{dN}{dA} \; . \tag{3.11}$$

Particle fluence has units of m^{-2} in SI notation. The planar surface component of fluence approximates the surface of CR-39 PNTD or an active detector. Since detectors typically have increased sensitivity to normally incident particles, a solid angle correction is performed to account for missed counts in an isotropic radiation field. In this case the units are modified, typically $cm^{-2}sr^{-1}$.

3.6.2. Absorbed Dose

The deposition of energy in matter by ionizing radiation is of fundamental interest in this work. Absorbed dose is the measure of energy absorbed, per unit mass, resulting from exposure to ionizing radiation. The expressions for dose and dose rate are [ICRU, 1998]:

$$D = \frac{dE}{dm} \ , \tag{3.12}$$

and

$$D' = \frac{dD}{dt} \ . \tag{3.13}$$

Radiation dose units in the SI are joules per kilogram of material. Absorbed dose is more frequently reported in units of Gray (Gy), 1Gy ≡ 1J/kg, or in units of Rad (R), 100 R = 1 Gy. Since energy deposition in matter can vary greatly depending on the properties of the exposed material, it is important to note the material in which the dose measurements are being made, e.g. dose in H_2O or dose in tissue.

3.6.3. Linear Energy Transfer

The CR-39 PNTD used in this work does not directly measure radiation dose, rather it measures the linear energy transfer, or LET of individual particles, which can then be used to calculate the dose received on the sensitive plane of the detector. The quantity LET in a material is closely related to the mass stopping power, S/ρ [ICRU, 1998]:

$$\frac{S}{\rho} = \frac{1}{\rho} \times \frac{dE}{dx} \ , \tag{3.14}$$

where ρ = density (units: g/cm^3). In the SI, mass stopping power has units J m^2 kg^{-1}, but in the literature the units MeV cm^2 g^{-1} are often used. The linear stopping power, S, is given by:

$$S = \frac{dE}{dx} \ . \tag{3.15}$$

The total mass stopping power, in the general case, includes contributions from electron interactions, which are described by the Bethe-Bloch formula, elastic and inelastic nuclear interactions, and, for electrons, radiative losses, e.g. Bremsstrahlung. The sum can be expressed as:

$$\frac{S}{\rho} = \frac{1}{\rho}\left(\frac{dE}{dx}\right)_{electronic} + \frac{1}{\rho}\left(\frac{dE}{dx}\right)_{nuclear} + \frac{1}{\rho}\left(\frac{dE}{dx}\right)_{radiative} \ . \tag{3.16}$$

For an energy threshold, Δ in eV, the restricted linear energy transfer, L_Δ, excludes the sum of kinetic energies for all electrons ejected with E > Δ from consideration. This relationship is expressed in the formula:

$$L_\Delta = \frac{dE_\Delta}{dx} = \frac{dE_{TOT}}{dx} - \frac{dE_{\geq\Delta}}{dx} . \tag{3.17}$$

In equation (3.17), the term dE_{TOT}/dx represents the energy loss of a charged particle in transit through matter, over the infinitesimal distance dx, from electromagnetic collisions with electrons at all kinetic energies. The last term, $dE_{\geq\Delta}/dx$, includes only the ionized electrons with kinetic energy over the threshold energy, Δ. In this notation, the restricted linear energy transfer, or LET, is expressed as LET$_\Delta$ with units typically given in keV/μm. In general, LET is material dependent, which requires additional notation, e.g. LET$_{200}$CR-39 is the linear energy transfer of a charged particle traversing CR-39 PNTD and neglecting electrons released with kinetic energy in excess of 200 eV. Another common notation is $LET_\infty H_2O$, which represents the linear energy transfer for all collisions between the primary charged particle and the target electrons in water.

3.6.4. Restricted Energy Loss

Primary ionization along the trajectory of a charged particle, known as specific primary ionization per unit path length, was evaluated as the damage source responsible for nuclear track formation [Fleischer et al., 1967]. It was later found that only a portion of the total charged particle energy deposition is responsible for the formation of a nuclear track [Benton et al., 1969b]. The restricted energy loss (REL) model has a functional form similar to the Bethe-Bloch equation for stopping power [Bethe, 1930] and accounts for the fraction of ionization events that contribute to track formation. The REL expression is:

$$\left(\frac{dE}{dx}\right)_{\omega<\omega_0} = \frac{2\pi n\left(z^*\right)^2 r_0^2 m_0 c^2}{\beta^2}\left[\ln\left(\frac{2m_0c^2\beta^2\gamma^2\omega_0}{I_{adj}^2}\right)+\beta^2+2\left(\frac{C}{Z}\right)-\delta\right]. \quad (3.18)$$

In equation (3.18), n is the density of electrons in the stopping material, $z*$ is the effective charge of the ionizing particle, β is the ratio of particle velocity to the speed of light v/c, m_0c^2 is the rest energy of an electron (0.511 MeV), $r_0 = \left(e^2/m_0c^2\right)$ is the classical electron radius, I_{adj} is the mean excitation potential in the stopping material, C/Z is the tight binding shell correction, δ is the correction for the density effect, and $\gamma = \left(1-\beta^2\right)^{-1/2}$. For CR-39 PNTD, it has been empirically determined that ω_0 = 200 eV [Henshaw et al., 1981]. This usage necessitates the notation $LET_{200}CR\text{-}39$ when referring to restricted energy loss in CR-39 PNTD, which is the quantity measured in our experiments, as opposed to $LET_{\infty}H_2O$, which is the total (unrestricted) stopping power in water for charged particles.

3.6.5. Calculation of Absorbed Dose from LET

Using LET information obtained from a detector, it is possible to calculate absorbed dose. For a mono-energetic particle beam with precisely defined LET and fluence, dose in Gy is obtained from the formula:

$$Dose = LET_{\Delta}\frac{\Phi}{\rho}\times 1.602\times 10^{-9}\ , \tag{3.19}$$

where ρ is density and the factor of 1.602×10^{-9} accounts for unit conversions.

In general, for a mixed radiation field with a variety of particles of varying LET, the following equation is applicable:

$$Dose = \frac{1.602\times 10^{-9}}{\rho}\sum_{i}\Phi_i LET_i\ , \tag{3.20}$$

where the summation over i adds up the contributions of all particles with Φ_i and LET_i. Since the measurement results from CR-39 PNTD analyses include a range of LETs, this is the formula most commonly used to calculate absorbed dose.

The extension of our methods for the measurement of short-range, high-LET charged particles to include the calculation of other dosimetric quantities, such as dose equivalent, will require an extensive study of the rate of change in particle LET, knowledge of microdosimetry, and more detailed measurements of the nuclear tracks themselves to obtain more detailed LET information. As such the discussion of these biologically weighted quantities is beyond the scope of present work.

CHAPTER IV

AFM METHODS FOR CR-39 ANALYSIS

The 1980's saw the emergence and rapid growth of the field of scanning probe microscopy (SPM), of which AFM technology is a subset. Following the invention of the scanning tunneling microscope (STM) [Binnig et al., 1982] and the AFM [Binnig et al., 1986], many new and innovative variants of SPM have been developed [Veeco Instruments, 2005b]. The various SPM methods have been broadly applied to basic research and manufacturing with great success [Sarid, 1997; Ratner et al., 1998; Morris et al., 1999; Bonnell, 2001]. The continued size reduction of microprocessor features, for example, has been in part due to the introduction of AFM techniques used in the design stage for failure analysis, quality control, and process development [Bailon et al., 2005]. This chapter discusses the application of AFM technology to the study of CR-39 PNTD by previous investigators and the new methods developed as part of this work.

Optical microscopy methods (OPT) utilize transmitted or reflected light from a region of interest on a specimen to resolve surface and subsurface (for transparent materials) details. In contrast, the principle feature of AFM is the direct measurement of surface features using the physical interaction of a suitable probing mechanism, in this case a silicon cantilever with a very sharp tip (radius of curvature ~10 nm), as it is moved about an area of interest. An example of the type of AFM tip used in this research is shown in Figure 10. The AFM used for this work is the Veeco Instruments Dimension 3100, shown in Figure 11.

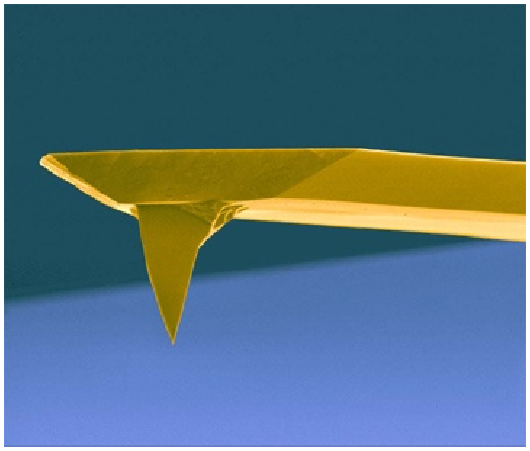

Figure 10. SEM image of a silicon AFM cantilever [Drexel, 2008] with an inverted pyramidal tip similar to the type used in this work.

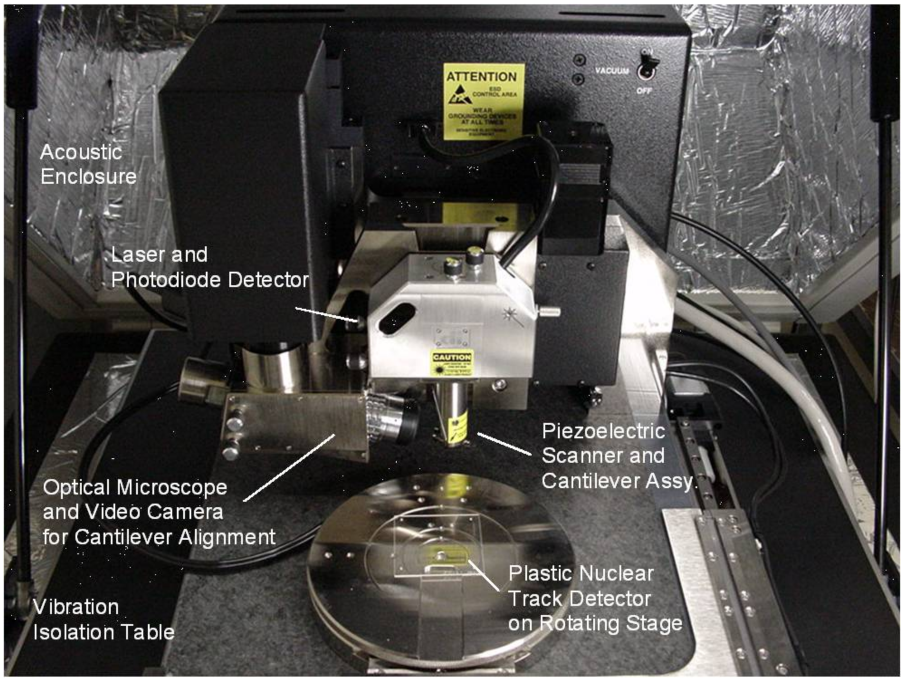

Figure 11. The Veeco Instruments, Dimension 3100 Atomic Force Microscope. The motorized stage is shown in the foreground and the scanner head is shown in the middle of the image.

AFM tip motion in X, Y, and Z is achieved via a tubular, 5 section piezo-crystal driver, as shown in Figure 12. The controlled application of voltage (0 to +200 V) to one segment of the piezo-tube (X or Y), accompanied by the application of an equal voltage of opposite polarity (0 to −200 V) to the opposing piezo-tube segment ($\bar{X}$ or $\bar{Y}$), causes a deflection of the AFM tip by the piezo-electric effect. The scanner head deflection is roughly proportional to the voltage applied. However, this relation is known to be non-linear near deflection extremes, where an increased voltage is required to achieve the same deflection. Compensation for piezo-tube non-linearity is accomplished in the AFM system calibration such that the applied voltage is modified to approximate a linear response from the scan head.

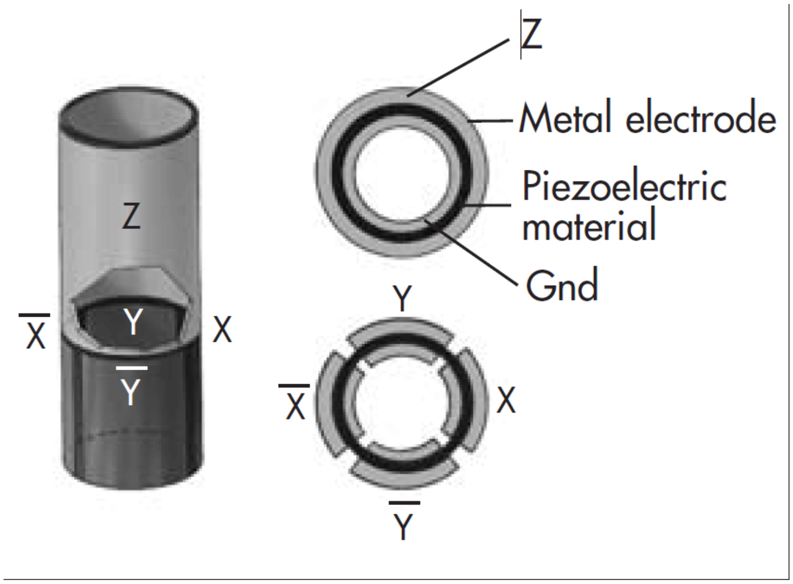

Figure 12. This is an illustration of the 5 segment piezoelectric drive tube that provides a three dimensional range of motion for the AFM tip [Veeco Instruments, 2005a].

The scanning of a surface takes the form of consecutive lines parallel to the X axis, with each line spaced uniformly along the Y axis. This is often referred to as raster scanning.

In general, some parameter of interest, such as height Z (but also contact force, capacitance, etc.) varies with both X and Y. The X and Y values during the scan are known, since they are provided by the SPM control system, while the third parameter is measured and recorded during the scan operation, resulting in a 3-dimensional data set.

While both OPT (gray scale imaging) and AFM produce 3-D data files, the critical distinction between OPT and AFM data is that AFM data is deterministic. With OPT methods, many surface features can yield the same gray scale value. AFM data is based on a very precise physical height measurement, typically accurate to within a tenth of a nanometer, and only a small range in surface height in Z will result in the corresponding 16-bit digitized value. The 3-D matrix of data collected by the AFM during a scan contains height with respect to X and Y, and is therefore a “topographic map” of the surface.

To obtain an AFM image, a false color mapping is used to assign a color value to surface features based on the Z value of the data matrix, as shown in Figure 13. This color mapping can be a linear gray scale, but more commonly other colors are used with a non-linear color gradient. Color map non-linearity assists the visualization of subtle surface features by changing the color more rapidly near the surface, which corresponds to the zero height value.

Using the various existing color maps or custom designed color maps, each with contrast (the steepness of the color map near zero height) and offset (the vertical position of the color map’s middle value) adjustments, there are nearly infinite display options for data visualization. However, the array of data visualization options complicates the interpretation of AFM data. Instead of frequently adjusting display settings, it is preferable to use one color map with the same settings applied to each scan. This greatly assists in feature comparison between AFM images.

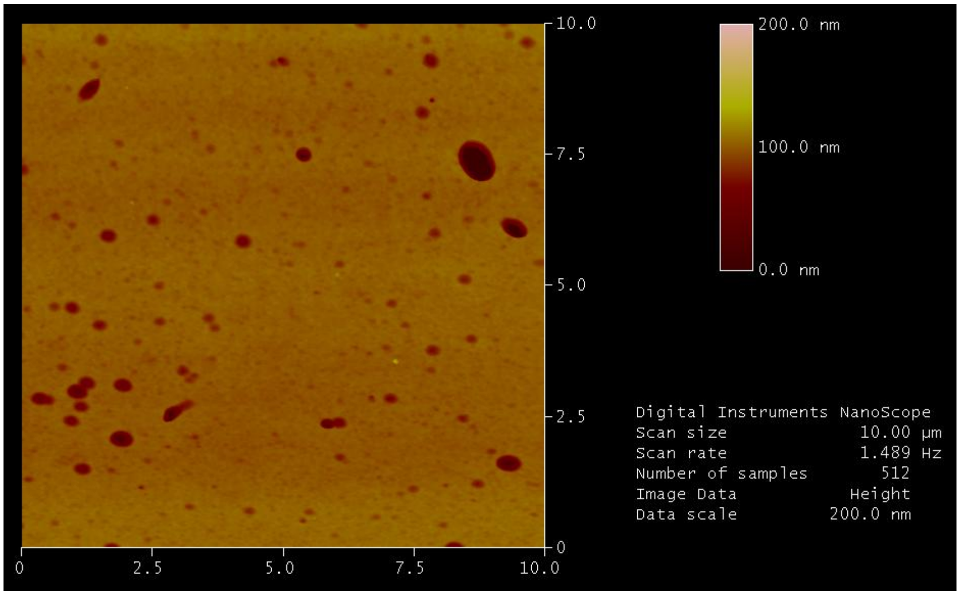

```
Digital Instruments NanoScope
Scan size               10.00 µm
Scan rate               1.489 Hz
Number of samples          512
Image Data              Height
Data scale            200.0 nm
```

Figure 13. Sample AFM scan from a typical CR-39 PNTD after exposure and etching. The color map scaling is shown in the upper right and various scan settings are displayed on the lower right.

4.0 AFM Principle of Operation

The AFM measures surface height by reflecting a laser off of the top side of the cantilever during the surface scan, as shown in Figure 14. Small changes in the cantilever angle, which are proportional to surface height, are detected using a position sensitive photo diode (PSPD) array. There is a fixed distance between the cantilever and the PSPD which is large compared to the scale of the AFM tip. This distance provides mechanical amplification similar in principle to the operation of a torsion pendulum. In a torsion pendulum, a small mirror is often attached to a fine wire. By reflecting a laser off of the mirror and onto a scale mounted a meter or more away, one can measure very small changes in angle with high accuracy. A similar usage of mechanical amplification by the AFM yields a very high measurement resolution in Z, typically a tenth of a nanometer.

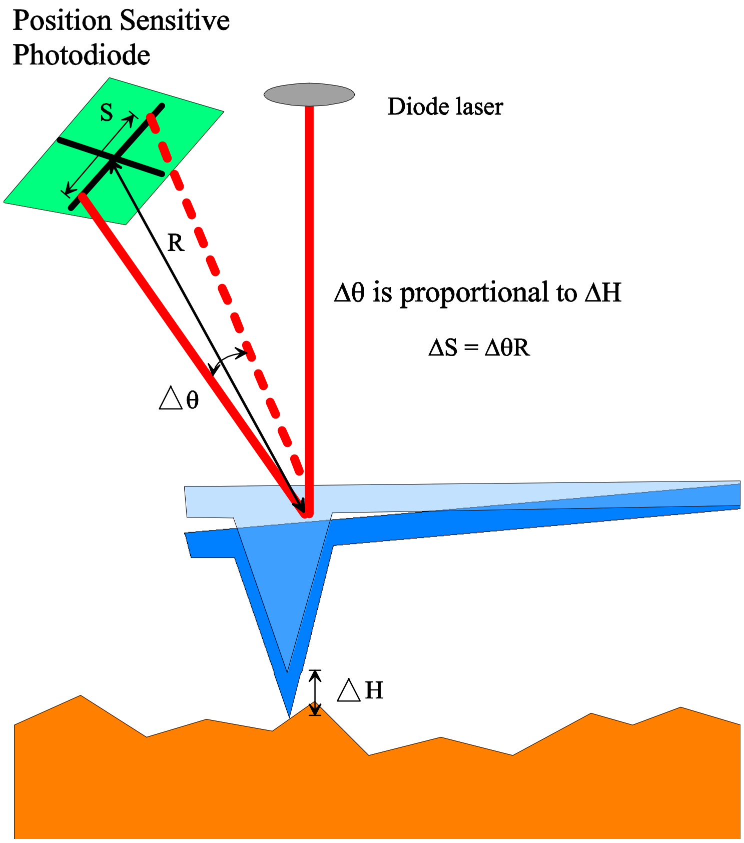

Figure 14. Scan head internal view showing PSPD detail. A small change in height, ΔH, shifts the laser reflection angle, Δθ, by a small amount. At the position of the photodiode, a distance, R, from the cantilever, the detected laser spot is moved by S = R × Δθ.

Lateral measurement resolution with the AFM is also potentially very high, but this is closely related to the cantilever tip geometry (intrinsic effects), as well as the sampling interval across the surface (extrinsic effects). The effects of scan size and sampling interval on lateral resolution are discussed later in this chapter.

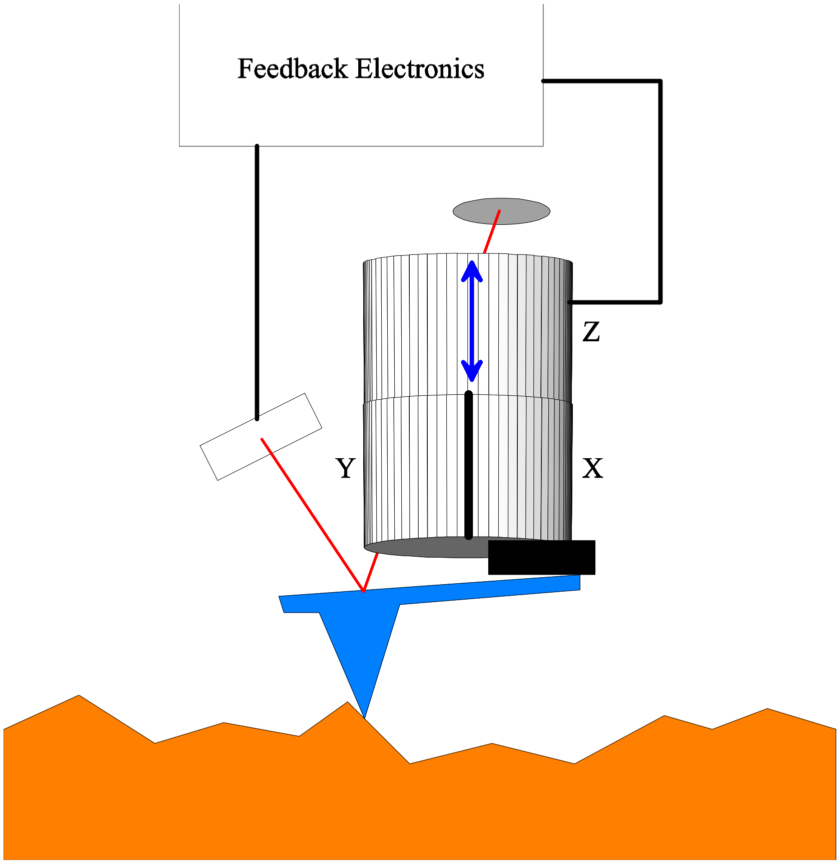

Figure 15. The feedback loop drives the Z piezo element during scanning to achieve fine positioning adjustments that are necessary to maintain surface tracking.

The AFM hardware has features that provide real time feedback during scanning to ensure surface tracking is maintained, as shown in Figure 15. Because the AFM needs to operate over a range of values in Z, it must compensate for local variations that may be encountered with each scan line. This is accomplished by adjusting the scanner head vertical position during the scan (up to 6 µm range of motion). The effects of scanner head adjustments must later be removed from the AFM data.

4.1. Tapping Mode AFM

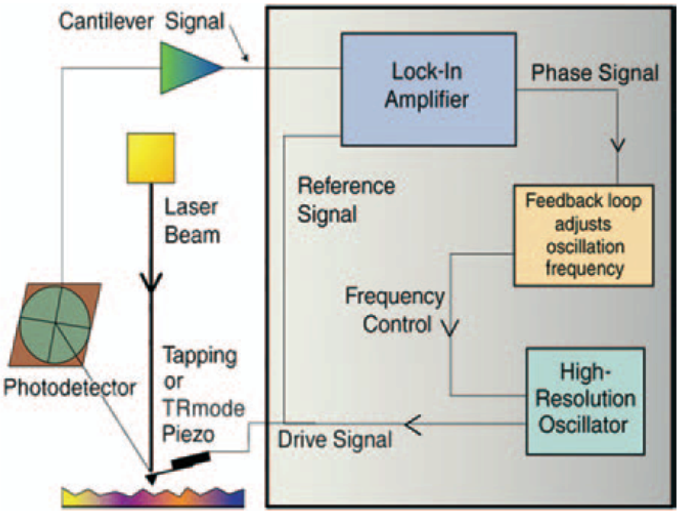

Figure 16. This diagram illustrates the AFM scanner feedback loop used to drive the AFM tip vibration during scanning [Veeco Instruments, 2005a].

The mode of AFM scanning used in this work is exclusively tapping mode AFM [Magonov et al., 1997]. In this mode of operation the silicon cantilever is vibrated at or very near its natural resonant frequency by a control circuit as shown in Figure 16. This resonant frequency is typically in the range of 200 – 400 kHz for the etched silicon cantilevers used in this work. As the vibrating tip is scanned across the sample surface, its vibrational amplitude is reduced in proportional to surface height, as shown in Figure 17. The reduction in vibrational amplitude is then used to determine the surface height. The early work done by our group evaluated the various scanning modes, including contact mode [Benton et al., 2001b] and it was found that tapping mode AFM was superior for the scanning of CR-39 PNTD.

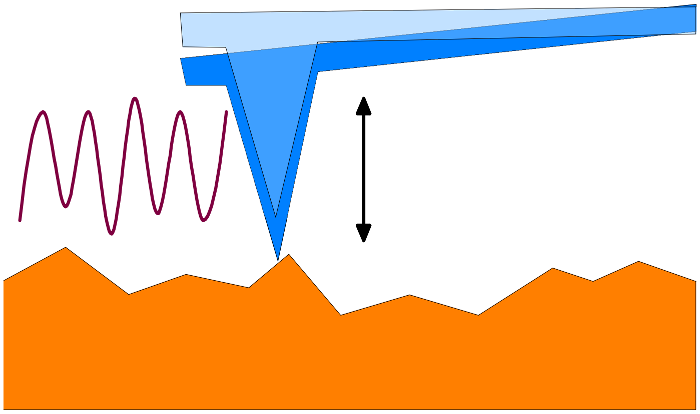

Figure 17. Simplified diagram illustrating tapping mode AFM. The vibrational amplitude of the silicon cantilever is reduced near surface peaks and increases near troughs.

Tapping mode scanning is generally more robust than contact mode for scanning sample surfaces that contain sharp or irregular features. In contact mode, the tip is maintained at a near constant contact force with the sample surface for the duration of the scanning operation. This can lead to jumps by the AFM tip when sharp edges are encountered, similar to releasing stored energy from a spring. These effects are recorded in the AFM data and will be seen as AFM image artifacts. Care must be taken when setting up a scan to minimize this effect. Tapping mode adapts to nuclear track edge transitions and other topographic variations, using the vibrational feedback previously mentioned.

Tapping mode scanning is also recommended for extended scanning periods in order to reduce tip wear. In contact mode scanning, since the AFM tip is dragged along the sample surface and is thus in constant contact with the surface, there is increased tip wear due to surface friction. However, even during tapping mode scanning it is normal for the tip to eventually become worn by extended use, typically after one week of continuous scanning. In addition, rough or improper usage can destroy an AFM tip very rapidly. New AFM cantilevers (Veeco Probes, P/N RTESPA) have a nominal radius of curvature at the tip of 8 nm. As the tip becomes worn, its radius increases, resulting in a reduction in surface feature sharpness, which reduces the quality of the measured AFM data.

Another detrimental effect normally encountered during routine AFM scanning is the accumulation of small dust particles on the tip. Since the AFM is scanning in air outside of a clean room, some dust accumulation is inevitable. As the tip is scanned across the PNTD surface, it can encounter tightly adherent dust particles that can attach to the tip, effectively changing the tip radius and leading to surface sampling errors seen as distortions in the AFM image. Frequent monitoring of the scan operation is necessary to identify and correct such tip fouling. On several occasions it has been possible to ‘scrape’ off accumulated dust by scanning a surface with very sharp features (either on purpose or during automated scanning). Normally, the best solution for a fouled or worn AFM tip is replacement.

In scanning a sample surface with the AFM, AFM parameters are adjusted specifically for the material under scrutiny. The contact force of the AFM tip is adjusted by setting a parameter called the amplitude set-point. As the amplitude set-point is decreased, contact force increases. For soft materials, this must be adjusted to a value high enough to avoid surface deformation or damage by contact with the cantilever tip. Harder surfaces can tolerate a low amplitude set-point, but at the expense of increased tip wear. It is common for AFM parameters to require frequent adjustment, even during a single scan, due to the occurrence of localized differences in surface composition. There are hundreds of parameters that require proper settings for the scanner to collect reliable data, but only a few need to be modified following initial calibration. The most frequently modified scanner settings are the scan rate, amplitude set-point, integral gain, proportional gain, Z range, and scan area [Veeco, 1998]. Scan area and scan rate combine to determine the scan speed. This is the approximate velocity of the AFM tip. The faster the tip is moved across a surface, the less time there is for the tip's vibrational amplitude to react appropriately.

An AFM image artifact is a sampling error that occurs during surface scanning that is then saved to the AFM data. If the AFM is operated with incorrect settings, image artifacts are likely to occur. It is our experience that the frequency and severity of artifacts increases with scan speed. For this reason, scans are performed at a relatively slow 50 µm/s or less. A detailed review of the known image artifacts present in AFM images is beyond the scope of the present discussion; these issues are well documented in the manufacturer's publications and in the literature [Veeco Instruments, 2005a, 2005b]. However, much effort was expended at the beginning of this project to determine optimal ranges of the various parameters and settings for accurate and reproducible scanning of the surface of CR-39 PNTD following chemical etching.

4.1. Initial AFM Applications to Nuclear Track Detection

The first commercially produced AFMs became available in 1989 [Veeco Instruments, 2005b]. The AFM was recognized early on as a tool that could be used to enhance understanding of the track formation and etching process in SSNTDs. The first use of AFM for nuclear track analysis was performed on un-etched mica samples exposed to energetic Kr nuclei [Thibaudau et al., 1991]. The first detailed application of AFM to the study of etched tracks was performed by Price et al. [Price, 1993; Snowden-Ifft et al., 1993], in which α-particle tracks in mica were examined. Using AFM, it was possible to physically resolve internal track details including the ~2 nm steps between crystalline planes inherent in mica, for the first time. The utility of the AFM for scanning etched nuclear track detectors was established by this analysis, but a great deal of work remained to attain a new comprehensive, quantitative analysis methodology.

The interaction of energetic heavy ions with a crystalline lattice was shown to form ‘crater-like’ features [Kopniczky et al., 1994; Kopniczky et al., 1995] on surfaces in which no chemical etching was used, a result that has importance to understanding nuclear track formation mechanisms and structure. In more recent observations, the charge dependence of this effect has been observed [Papaleo et al., 2008]. In other early experiments, nuclear tracks formed by 1-10 keV/amu Si ions in CR-39 PNTD were analyzed [He et al., 1995], establishing the AFM as a tool to study nanometer scale features in CR-39 PNTD with high accuracy. Track evolution during etching [Drndic et al., 1994; Yamamoto et al., 1999], detector sensitivity [Yamamoto et al., 1997; Yasuda et al., 1999], and various chemical etching variables [Yasuda et al., 2001] were all studied by investigators seeking to take advantage of the enhanced spatial resolution of the AFM.

Since the AFM requires 35 minutes, on average, to capture a surface scan, the AFM is not seen as a viable replacement for OPT methods. Indeed, due to prolonged scanning time, established OPT methods will almost certainly remain the primary tool for routine CR-39 PNTD analysis. Only in special cases are AFM methods warranted. For particle fluences $\geq 10^5$ cm^{-2} or for measurements of high LET, short-range particles (≤ 8 μm), the AFM has been shown to have clear advantages [Benton et al., 2002a].

The first broadly applicable work with the AFM pertinent to CR-39 PNTD was conducted by Yasuda [Yasuda et al., 1998], who developed a method for directly measuring the bulk etch, *B*, with the AFM. In what is now called the 'step method' [Kodaira et al., 2007], a portion of the PNTD is masked by epoxy (Araldite, Showa Highpolymer Co.) prior to chemical etching. The layer covered by epoxy does not come into contact with the etch solution and will experience no etching, while the exposed surface area of the PNTD will etch normally. After etch completion, the epoxy is removed and a scan is performed in a region containing both masked and exposed PNTD surface. The height transition between the masked and exposed surface is measured during the scan, yielding the bulk etch, *B*. Additionally, this work quantified the increase in post-etch surface roughness as a function of etch time. For most CR-39 PNTD used in this work, a 2 hour etch in 50° C, 6.25 N NaOH was used. Using the step method proposed by Yasuda for determination of *B*, this etch protocol was found to achieve a bulk etch of approximately 0.5 µm (i.e. 0.25 µm/hr).

4.2. AFM Limitations: Track Depth Measurements

An important limitation to AFM application to CR-39 PNTD analysis is the measurement of track depth. Due to the shape of the AFM tip, it is not generally possible to directly measure the bottom of a nuclear track, even for normally incident particle trajectories. A thorough analysis of this issue has been performed [Nikezic et al., 2002] and its relevance to our work is further discussed in the next chapter. While direct depth measurement would be a powerful tool for LET determination, there are major obstacles presented by the respective geometries of the cantilever tip and the etched nuclear track, and no such implementation has been made in the present work.

4.3. AFM Advantages in CR-39 PNTD Analysis

As an analytical tool, CR-39 PNTD has several limitations as mentioned in the previous chapter. It is important to observe that many of the limitations are directly related to the amount bulk etch required for analysis of etched tracks with an optical microscope. Application of AFM to the analysis of CR-39 PNTD allows the use a much smaller bulk etch, ~0.5 µm as opposed to 8 µm or more for OPT, which can improve the analytical accuracy by reducing the occurrence of over-etched tracks, as illustrated in Figure 18, minimizing the occurrence of overlapped tracks, reducing analysis plane ambiguity, and retaining tracks formed by short-range, high-LET particles.

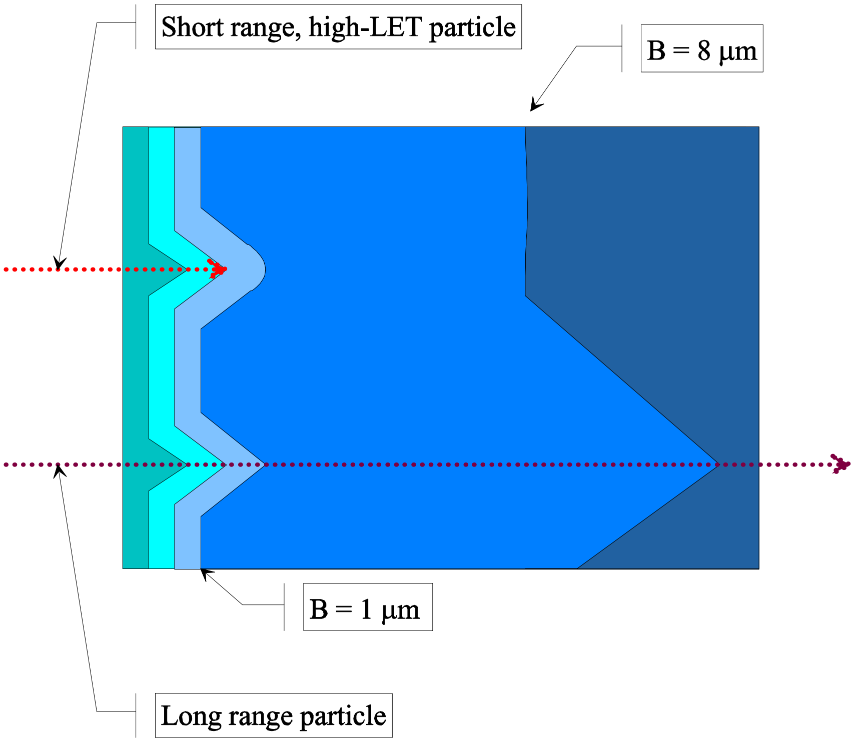

Figure 18. Illustration of etch progression with the bulk etch, *B* increasing from left to right. Short-range, high-LET nuclear tracks are completely removed for large values of *B*, such as those used for optical microscopy methods as discussed in Chapter III.

The post-etch surface of PNTD is a record of the passage of charged particles. Not all of the registered tracks originate outside of the detector. A contained track is the result of a nuclear reaction between a primary beam particle and a nucleus in the CR-39 PNTD itself, within the region of the detector removed by etching. As the bulk etch is increased, the likelihood of encountering a contained track increases. This is effect is illustrated in Figure 19. In this work, contained tracks are referred to collectively as the internal component of the nuclear track population measured during an analysis.

The layer of CR-39 removed by chemical etching between pre-etch and post-etch surfaces can be considered the analytical plane of the detector. The detector can only provide information about particles with sufficient LET that pass through this layer or those that are formed inside it, e.g. contained tracks. As the thickness of the analysis plane is reduced by reducing the bulk etch, uncertainty with respect to particle origin is reduced as well. The reduction in the potential for internal track formation, and the associated reduction in ambiguity with respect to particle origin, is another advantage of this method.

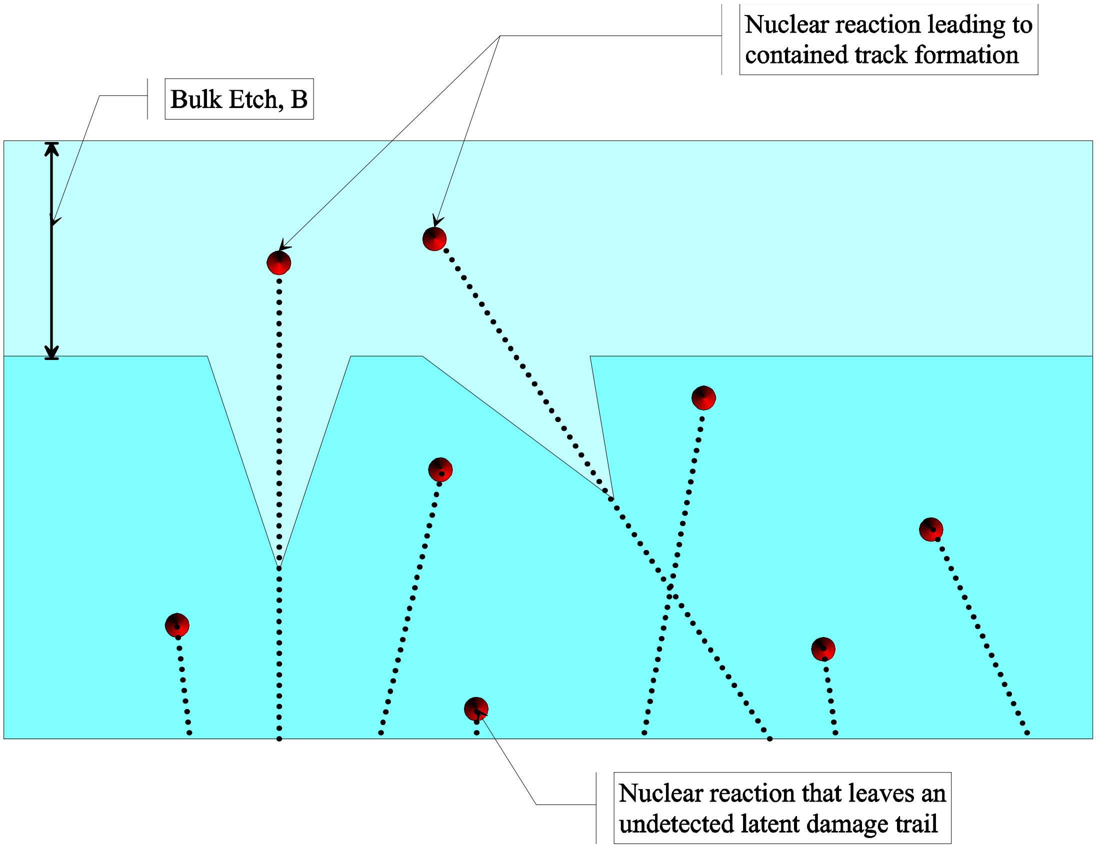

Figure 19. As bulk etch, *B*, is increased, an increased number of contained tracks, formed as a result of nuclear interactions with C and O nuclei in the CR-39 PNTD, will be measured on the post-etch detector surface.

Over-etched tracks are formed when the bulk etch becomes greater than the track length. These tracks are identified by a circular opening and bowl shaped interior. With a 0.5 µm etch, only particles already in the process of stopping very near the surface would have the potential to become over etched. This type of event is comparatively rare with respect to the vast majority of observed tracks when a 0.5 µm etch is used. However, it is a major component in CR-39 PNTD exposed to proton beams and then analyzed following 8 µm bulk etch.

With a small bulk etch there is also insufficient increase in etched track size for neighboring tracks to overlap. With OPT analysis, the fluence limit of $\sim 10^5$ cm^{-2} is a result of the difficulty in analyzing overlapped tracks. AFM analysis of CR-39 PNTD permits fluences of $\sim 10^8$ cm^{-2}. CR-39 PNTD exposed to high particle fluences, such as on the exterior of spacecraft (for long duration and under low shielding) cannot be analyzed by OPT methods, but are amenable to AFM analysis. In addition, with AFM/CR-39 PNTD analysis, since overlapped tracks are much less likely, the tracks that are overlapped are more likely to be related to the same nuclear process. This has the potential of opening new research directions through studying nuclear reactions with multiple knock-outs.

4.4. Sampling Theory and Resolution Issues

Analogous to the Nyquist-Shannon sampling theorem in signal processing, to analyze a track, sufficiently many data points must be collected to test a surface feature for acceptance as a track. The Nyquist frequency is the minimum frequency of sampling to avoid aliasing when taking digital samples of an analog signal. The frequency of digital sampling must be at least twice the maximum frequency present in the analog signal, otherwise a falsely low frequency (hence an alias) can be recorded. Typically the sampling rate is much higher than the highest frequency of the signal. For example, to sample a 100 Hz square wave properly, a 1-10 kHz sampling rate would be used.

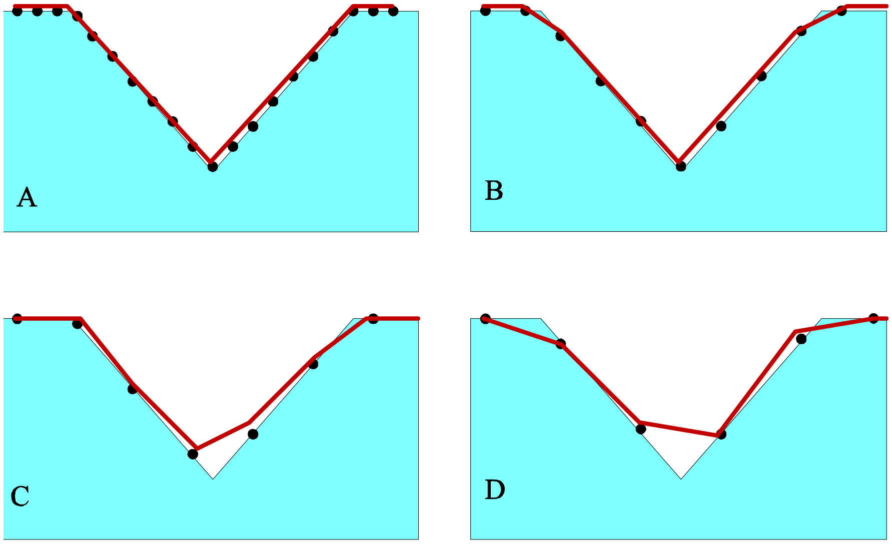

Figure 20. Increased spacing between data points (black dots) reduces the measurement resolution of the AFM. The red line indicates the measured surface shape. The four sampling examples are discussed in the text.

With respect to sampling of the etched PNTD surface by AFM, aliasing is not encountered in the same manner as in digital signal processing. Rather, the aliasing effect is manifested as a reduction in measured sharpness for sharp edged surface features. This effect becomes more pronounced as the spacing between data points is increased, as shown in Figure 20. Referring to Figure 20, in A, the nuclear track is well sampled and accurate interpretation can be performed. In B, with half of the data points of A, the track is not as sharply defined, but analysis is still possible. In C and D, the sampling begins to become inadequate, e.g. it is aliased as a shallow rounded track, and accurate analysis becomes difficult.

For a given scan size on a detector processed for a given bulk etch, *B*, the physical limitation of sampling on resolution imposes a lower limit on the smallest feature, and therefore the lowest LET, that can be reliably measured. The precise definitions of sufficient sampling and reliable, accurate, and reproducible analysis for AFM scanning of etched nuclear track detectors were established in the early phases of this work.

The Dimension 3100 AFM has a maximum scanning resolution of 512 samples per line. Each of these samples is a 16 bit digital value. For a 10 µm × 10 µm scan, the linear spacing between samples is 19.5 nm. An examination of the sampling matrix in X and Y for the 10 µm × 10 µm scan, shows that it contains a mesh of 262,144 data points separated by about 19.5 nm in each direction.

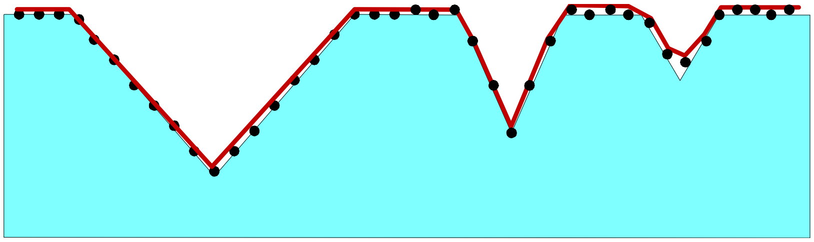

Figure 21. With a fixed sample interval between height measurements, as nuclear track size decreases (from left to right), the accuracy of the analysis decreases since fewer measurements are made for smaller nuclear tracks.

The analysis of sampling capacity begins at the extremes of very large and very small features which are to be measured. For very large features, those that occupy more than ~5% of the scanned surface, a large number of samples will be involved and adequate sampling is readily attained. At the other extreme, for very small features, a small number of samples are involved and adequate sampling is certainly not attained.

A question which must be addressed is for what value of feature size and sampling interval does the transition from inadequate to adequate sampling occur? To answer this question, the degree of accuracy required for track analysis in a particular experiment or application must first be established. The ellipse fitting algorithm (described in the next chapter) requires a minimum of 5 data points for an accurate result. However, as will be shown at least 15 points are chosen so that sufficient information is acquired to perform additional analysis based on the dimensions of the track interior. For a circular track present in a 10 µm × 10 µm scan, with the points evenly distributed around the circumference, the minimum measureable track has approximately a 95 nm diameter. This track corresponds to LET ≅ 5 keV/µm when a 0.5 µm etch is used, which is close to the lower threshold of sensitivity for CR-39 PNTD.

For 50 µm × 50 µm scans, a similar analysis yields a lower $\mathrm{LET}_{200}\mathrm{CR}$-39 detection threshold of 60 keV/µm ($\mathrm{LET}_{\infty}\mathrm{H_2O}$ = 90 keV/µm). This theoretical value is qualitatively consistent with our analysis results obtained from the AFM scanning of many detectors. For 50 µm × 50 µm scans, a reduction in measurement capacity has been observed for low LET tracks, e.g. those with $\mathrm{LET}_{\infty}\mathrm{H_2O} \lesssim 200$ keV/µm. This is most likely due to the fact that nuclear tracks are not generally circular, but can have a range of elliptical eccentricity. In summary, to obtain data from low LET nuclear tracks, small scan sizes are used due to the LET threshold imposed by scan size selection.

4.5. Methods for Measuring the Full LET Spectrum with AFM

As mentioned above, the scan size selection imposes a lower threshold of LET measurement capability that is not related to the characteristics of CR-39 PNTD, but is due to the measurement limitations of the AFM. The maximum scan size for the Dimension 3100 AFM is 90 µm × 90 µm. Due to the effects of piezo-tube hysteresis at large scan sizes, it is not recommended to collect scans near the limits of the instrument and instead a scan size of 50 µm × 50 µm is used. Since smaller scans, e.g. at 10 µm × 10 µm are unlikely to measure many high LET tracks, a combination of large and small area scans is needed to obtain the entire LET spectrum from a given detector.

Large area scans are needed to get sufficient statistics for high LET particles. This type of event is comparatively rare. Typically there are ≲10 high LET (≥200 keV/µm) tracks per 50 µm × 50 µm scan. Small area scans (10 µm × 10 µm or less) adequately sample smaller, more common nuclear tracks, with sufficient resolution for analysis. At large scan sizes, however, these tracks are grossly under sampled so accurate analysis is not possible. The small and large scans are analyzed independently to obtain proper fluence information. The two LET spectra, obtained with different scan sizes, are merged together to obtain the complete LET spectra for a single detector. This is a time consuming process that is only required or beneficial for certain experiments. In this work, the primary focus is on short-range, high-LET HNR particles, so a 50 µm × 50 µm scan size is used. For analysis of CR-39 PNTD exposed under minimal shielding on the exterior of spacecraft, a combination of small and large area scans was used.

4.6. Automated AFM Scanning Methods

Evident from the preceding discussion is the need for many AFM scans to collect sufficient track data to attain statistically significant measurements across the range of LET. Manually starting the AFM for each scan is both time consuming and problematic in that avoiding the locations previously scanned can be difficult. It is important to avoid scanning the same area twice in order to prevent measurement errors. AFM scan automation has been implemented using two software commands native to the Veeco AFM software: Auto Scan and Programmed Move, both of which are capable of preventing duplicate scans with proper operation.

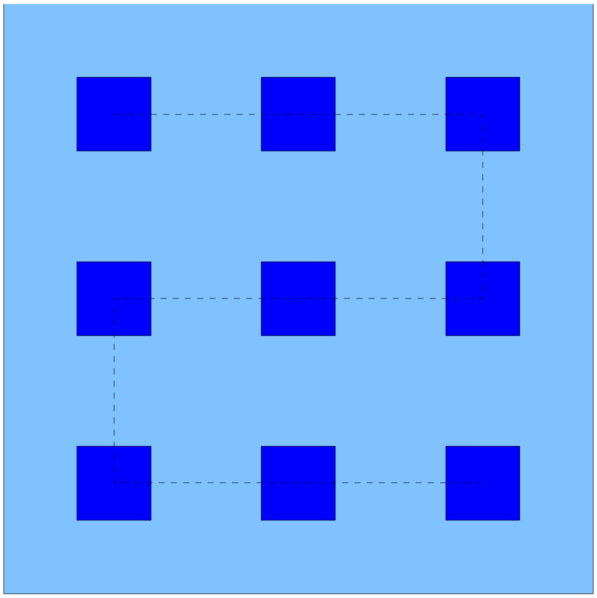

Figure 22. The Veeco Auto Scan function can be used to obtain multiple, non-overlapped AFM scans in the same stage position. This function is useful to increase the sampling resolution in an area of interest.

The Auto Scan function is useful to acquire many scans in one small region. Since the scan head can cover a full range of 90 µm × 90 µm in one stage position, it is possible to break up each scanner position into sub-scans of smaller area. The primary advantage of this function is improved sampling resolution for the same scan area. The resolution of the AFM is fixed at 512 samples per line. If this is distributed over 100 µm then there is a measurement made every 195 nm. Instead, if an Auto Scan is used with four sub-scans each measuring 50 µm × 50 µm, a measurement is recorded every 98 nm. This increases the resolution by a factor of two at the expense of a scan time increase. Typically, nine evenly separated sub-scans in a 3 × 3 matrix are used, as in Figure 22, with each scan measuring 10 µm × 10 µm to achieve a measurement resolution of 19.5 nm in the area scanned.

The Programmed Move feature differs from Auto Scan in that the motorized stage of the AFM physically repositions the detector for each scan frame taken. With this function, it is possible to scan up to 99 consecutive frames without operator action. The Programmed Move command used for this work, was designed to perform a scan, disengage the scan head, move 500 µm laterally, reacquire the surface and perform another scan. This sequence continues across the surface in the X coordinate until 10 scans are complete. Then the stage is moved 500 µm in Y and the previous process is reversed. Once the scan head has returned to the starting X column, another Y step is made and so on. The resultant scan pattern obtains 99 consecutive scan frames, which are spaced in a grid with 500 µm separation between each frame. Typically multiple Programmed Move operations are performed in different positions to yield $\gtrsim$ 200 scan frames for analysis of a given CR-39 PNTD.

For a given Programmed Move command, the AFM scan size, which is the range in µm for both the X and Y axes, is set at the beginning of the execution of the command. Once the Programmed Move has started, this parameter and other scan parameters cannot be adjusted. The separation between scan locations can be altered, but this requires manually programming a new Programmed Move command.

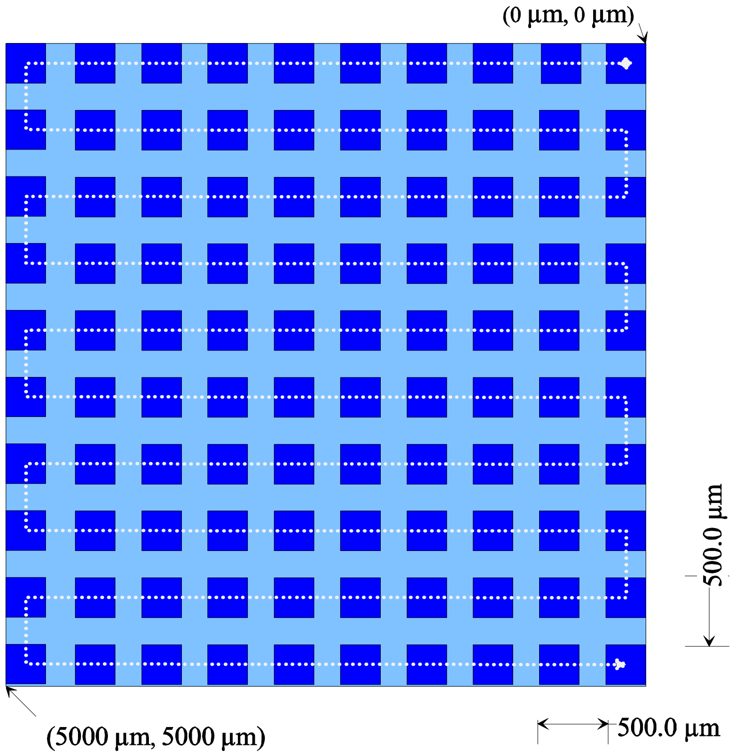

Figure 23. The Veeco Programmed Move command is useful to obtain multiple, non-overlapped AFM scans in different stage positions. This function is useful to automate data acquisition for large area measurements. A 500 µm pitch is used between scans to avoid scanning overlap. The AFM scans can be of varied scan size.

To preserve image quality during long duration scanning, i.e. the execution of a Programmed Move command, the automated drive feedback feature can be used. With this setting enabled the scan head is adjusted continually during scanning such that proper scan settings are maintained between consecutive scan frames. Without using automatic drive feedback during extended scanning, the scan head will no longer track the surface properly after the first few scan locations and poor data will be collected.

The scan rate/scan speed relationship is;

$$speed = 2 \times rate(Hz) \times size(\mu m), \qquad (4.1)$$

where the factor 2 arises due to the fact that the scan head crosses the scan field twice (in the trace and retrace directions) for each scan line measurement. A maximum scan speed of ~50 µm/s was found empirically to be optimal for CR-39 PNTD with a bulk etch, *B*, of 0.5 µm and minimizes the occurrence of AFM image artifacts. With proper observation of the speed limit, the AFM operator may adjust scan size (10, 25, or 50 µm as needed for statistical purposes) without danger of excessive artifacts. Typically if one increases the scan size without reducing the scan rate, the effect is immediately observable due to the appearance of artifacts.

With proper cleanliness and handling precautions (to avoid finger oil surface contamination) an AFM tip can be expected to scan roughly 200 or more frames before wear becomes intolerable. As a routine check of tip condition, a scan was performed on a TiO_2 coated specimen (available from Tip-Check™). This specimen has small, angular features, as shown in Figure 24, that will not be resolved well if a worn or fouled tip is used. After this diagnostic scan is complete the small features present in the Tip-Check™ specimen provide a tool to verify tip shape.

Veeco software includes a function called Automatic Tip Qualification that estimates the tip geometry based on surface details. The tip qualification process infers (calculates) the shape of the AFM tip from the local maxima present on a scanned surface. For tip qualification to be reliable, a material with many small features must be used as the input file, hence the use of the Tip-Check™ specimen. Once the tip is shown to be worn by the tip qualification process, or by direct operator observation of poor scan data, the tip is replaced.

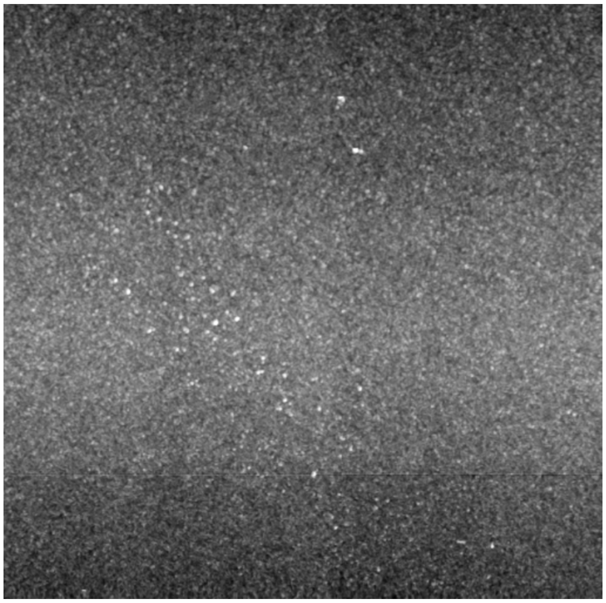

Figure 24. AFM image taken from the TiO_2 coated Tip-Check™ specimen. With this image, cantilever tip radius can be checked using Automatic Tip Qualification.

Blurred features, repetitive shapes, loss of small details, and changing shape near the surface of conical tracks are indications of tip wear, damage, or fouling. The experienced operator will notice immediately when tip integrity has been compromised. Additionally, it is possible to calculate the surface roughness using the installed software library or an external code, in order to check image quality during analysis.

4.7. AFM Scanner Calibration

Frame orthogonality is very important for accurate measurement of track ellipticity. The Veeco software includes a calibration procedure for performing adjustments to the scanners various settings. This was completed early in our work. Once the instrument is properly calibrated, there is very little variation in scanner response over time. If the AFM were to be improperly calibrated with respect to orthogonality, then a nuclear track with a circular surface opening would be measured to be elliptical, additionally an elliptical track would be measured with an incorrect eccentricity. This would result in an incorrect LET measurement for the track. Due to the importance of proper calibration, the system calibration was verified at the beginning of data collection and frame orthogonality was verified frequently thereafter.

A grid standard is used in the AFM calibration procedure and for routine checks of frame orthogonality. This grid is s silicon specimen that has 10 µm × 10 µm squares etched in a continuous array (10 µm pitch) across its surface. The squares are 200 nm deep. Since this grid specimen has a known regular spacing and depth it can be used to validate the scan parameters used in a particular scan process. This grid is the most frequently scanned item in our laboratory.

CHAPTER V

ANALYTICAL TOOLS FOR AFM DATA

One of the primary objectives of this work has been to develop a quantitative analytical method, consisting of the necessary hardware and software tools, for AFM analysis of prepared CR-39 PNTD. The experimental procedure for AFM analysis of a given CR-39 PNTD used in this work is shown in Figure 25. This chapter describes the work carried out and the algorithms developed to meet the requirements of step 7, ‘Analyze AFM Data’.

Any analysis system for CR-39 PNTD must be capable of accurately measuring the physical dimensions of multiple nuclear tracks present in each AFM scan, while rejecting surface features that are not nuclear tracks. The analysis system must perform such that it can be applied to multiple AFM scans in a timely manner. In the initial phases of this work, a number of AFM data analysis methods were evaluated. AFM data analysis tools developed by the manufacturer (Veeco Instruments, Inc.) were found to possess significant limitations and proved to be unsuitable for the analysis of large numbers of AFM frames from a given CR-39 PNTD. Methods based on 2-D image analysis, while initially promising, were also found to have only limited applicability, largely due to the inherent differences between a 2-D grayscale image and the 3-D topographic matrix of the AFM data frame. Ultimately, it was determined that the best solution was to create from scratch a set of AFM data analysis tools that were optimized to the analysis of CR-39 PNTD.

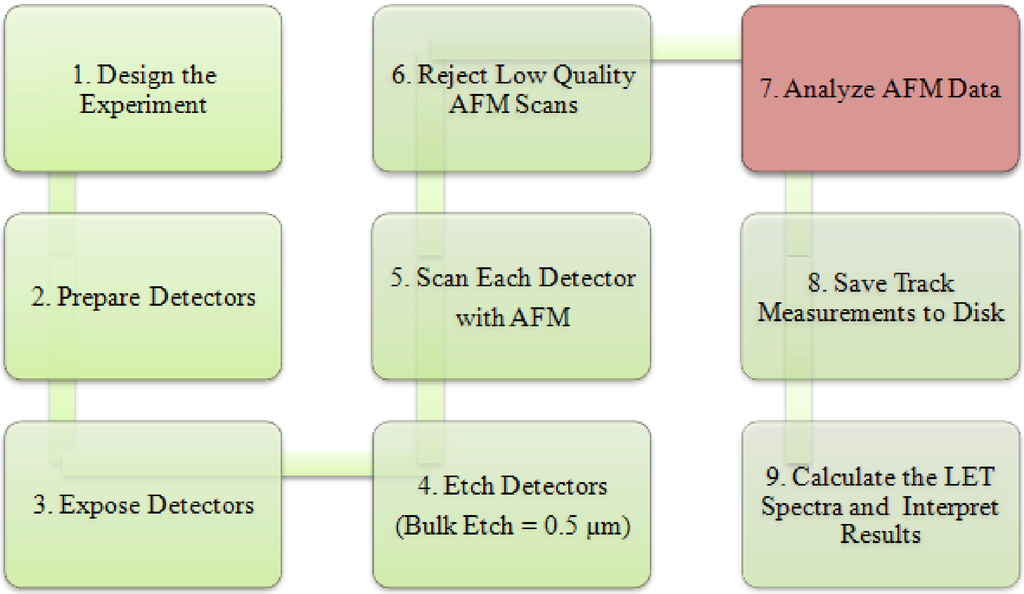

Figure 25. Flowchart depicting the order of analysis steps for a given experiment. This chapter focuses on step 7, Analyze AFM data.

Quantitative AFM methods exist in many fields of study including lateral force measurements [Cain et al., 2001], ligand-receptor binding forces [Isralewitz et al., 2001], switching analysis of ferro-electric materials [Jesse et al., 2006], as well as the more common contact force and surface roughness methods [Veeco Instruments, 2005b]. To the best of our knowledge, this work is one of the first efforts to develop tools for the quantitative analysis of surface features obtained from segmented geometrical primitives (shapes) in data acquired from large numbers AFM data frames obtained from scanning a single sample or object.

In the following discussion, the terms AFM data, AFM scan, and AFM image are closely related but not synonymous. The term AFM scan is used when discussing the data acquisition process of the AFM. The output of the AFM scan is AFM data, which contains the 3-D matrix of points obtained from the interaction of the scanner head with the surface. An AFM image, for example Figure 26, is the result of applying a false-color map to AFM data.

Figure 26 shows a representative sample of an AFM image from exposed and etched CR-39 PNTD and many types of features can be seen in AFM data. A general problem of AFM data analysis consists of distinguishing between features in the data that represent nuclear tracks and those features that are attributable to surface noise, dust, scratches and other non-track features. Additionally, nuclear tracks found with a portion of the track cone lying outside the scan frame, and other tracks that are obscured completely by dust or anomalies in the PNTD surface must be rejected. The nuclear track data, once extracted from the AFM data, must be analyzed to determine the reduced etch ratio of each track.

In the analysis of the AFM data, there are several attributes that can be utilized to distinguish between nuclear tracks and non-track surface features. Nuclear tracks can have a variety of depths, typically greater than 50 nm, while surface noise is usually contained within ± 10 nm of the surface. Additionally, etched nuclear tracks generally form well-defined cones that intersect the CR-39 PNTD surface to form elliptical or circular features, while non-track features tend to be amorphous. Nuclear tracks occasionally overlap, complicating analysis as an accurate analysis method must recognize each distinct track.

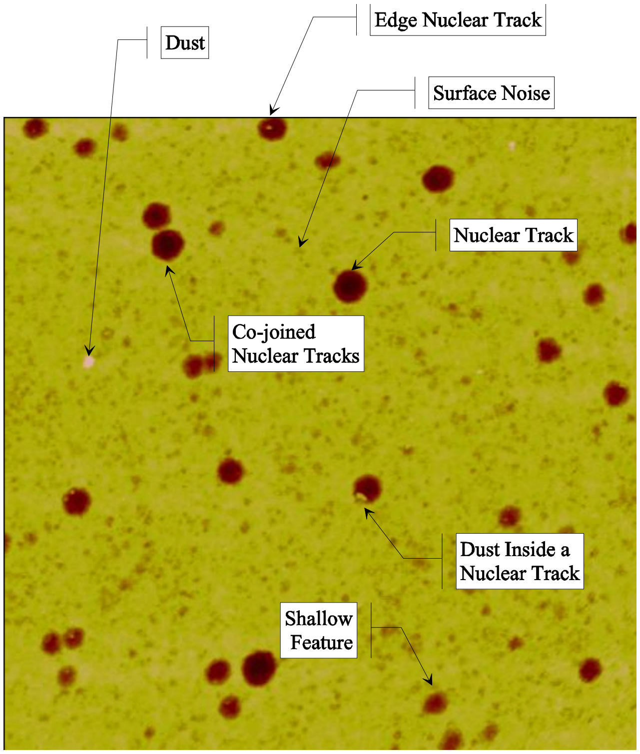

Figure 26. AFM image obtained from a detector that was exposed in low earth orbit, containing a range of particle LET values and incidence angles. Various features are labeled to illustrate the various difficulties in AFM data analysis.

5.0 Veeco Analysis Tools

The standard Veeco software analysis tools have several major limitations that make them unsuitable for AFM/CR-39 analysis. The only standard Veeco function useful for nuclear track measurements is the section analysis tool, illustrated in Figure 27. With this tool, the operator can place a line across the scanned data and then position markers at selected points restricted to that line. A data panel display on the section analysis tool's display shows the various physical parameters that are calculated between the two markers. If a marker is placed at each end of an elliptical opening, the distance between markers is the major axis. A second marker set can be used to measure the length of the minor axis. The values reported in the section analysis tool's data panel must be manually recorded to a spreadsheet to conduct further calculations. This process must be repeated for each track present in an AFM image. After the tracks are analyzed in this fashion, the reduced etch rate ratio, V_R, can be calculated, as discussed in Chapter III, and further analysis can then be performed.

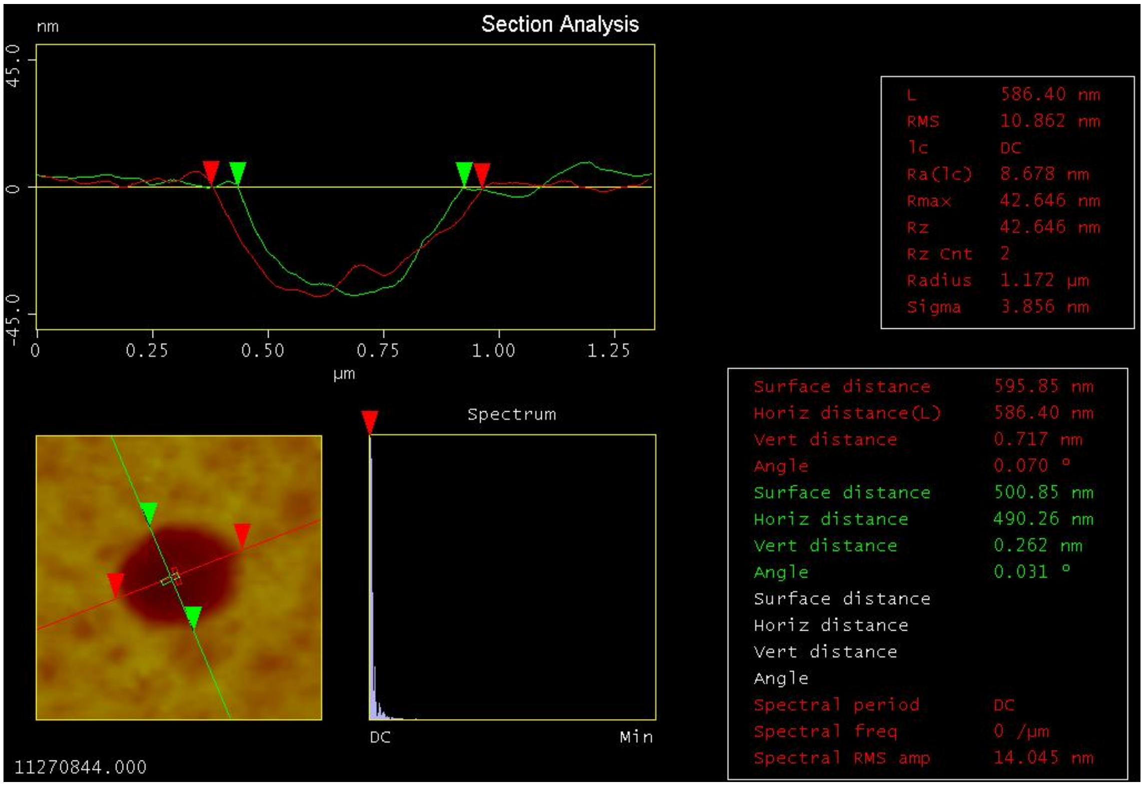

```
L            586.40 nm
RMS          10.862 nm
lc           DC
Ra(lc)       8.678 nm
Rmax         42.646 nm
Rz           42.646 nm
Rz Cnt       2
Radius       1.172 µm
Sigma        3.856 nm
```

```
Surface distance       595.85 nm
Horiz distance(L)      586.40 nm
Vert distance          0.717 nm
Angle                  0.070 °
Surface distance       500.85 nm
Horiz distance         490.26 nm
Vert distance          0.262 nm
Angle                  0.031 °
Surface distance
Horiz distance
Vert distance
Angle
Spectral period        DC
Spectral freq          0 /µm
Spectral RMS amp       14.045 nm
```

Figure 27. Screen capture of the section analysis tool in use to measure an elliptical track. The red markers are in position to measure the major axis and the result is displayed in the data panel on the lower right hand side.

For each track to be analyzed with Veeco's section analysis tool, the analyst must choose the placement of the sectioning lines manually. Usually multiple attempts are required to attain proper positioning. Additionally, it may be necessary to adjust the color mapping contrast during this process to accurately reveal the track's edge. Sometimes it is useful to perform a zoom operation to isolate the track from other features. The involvement of a human analyst, regardless of skill, introduces measurement uncertainties due to manual establishment of major and minor axis positions and section marker edge placement.

In order to obtain good (Poisson) statistics across the full range of particle LET, hundreds of tracks must be analyzed. It is difficult for a human analyst to maintain a high level of concentration and objectivity for the time required to complete the analysis. These factors also lead to large time requirements for AFM data analysis which are prohibitive.

5.1. Image Processing Approach

As an alternative to the section analysis tool, various traditional 2-D image processing methods were evaluated. In image processing, an example of which is shown in Figure 28, the AFM data is converted to an AFM image file using a false color mapping and saved to computer disk. The AFM image is then analyzed with edge detection, watershed segmentation, or other morphology tools. The drawback to this approach is that the false color mappings typically do not have linear scales from one color extreme to the other. Instead there is usually a more rapid change in color near the surface zero value. This type of color map is useful to highlight subtle surface effects for qualitative work, but it complicates image analysis in quantitative applications.

In image analysis, it is necessary to apply a discrimination threshold, which is tantamount to single layer analysis. An accurate analysis method needs to identify circular and elliptical features on a surface and then provide tests for acceptance as a track. Image processing tools work well for edge detection, but fail to provide additional tests required for track acceptance. In addition, information needed to discriminate between track and non-track features is often lost. It would be possible to implement an analysis package for CR-39 PNTD based entirely on an image processing approach, but it would be unnecessarily complicated and limited. For this reason, the traditional image processing approach was rejected.

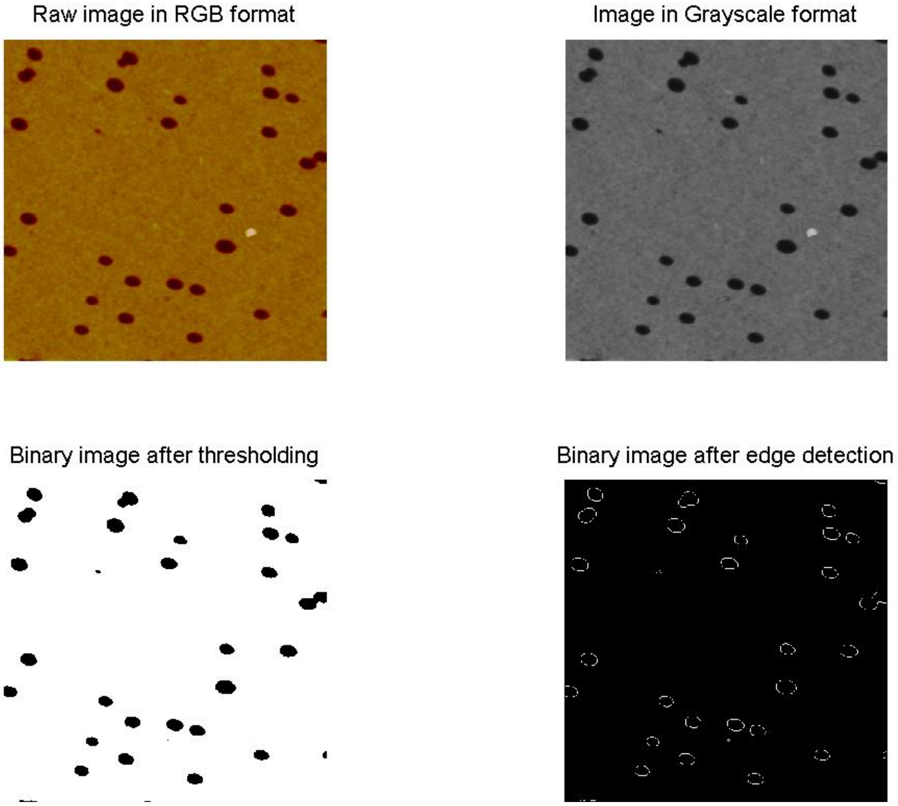

Raw image in RGB format

Image in Grayscale format

Binary image after thresholding

Binary image after edge detection

Figure 28. An AFM image processed with traditional image processing methods.

5.2. Data Filter Usage

In the initial stages of this work, various noise reduction filters were evaluated for use in processing AFM data. There are many filtering options available. Data filtering algorithms compute an output matrix of points in which each point is the result of a computation applied to a set of points from the original matrix. The set of points from the original matrix is called an analysis neighborhood. Analysis neighborhoods can be of various shapes and sizes. The data filter types evaluated in this work included Gaussian, median, Wiener, and others with varied neighborhood selections.

After evaluating the effects of data filters with respect to overall analysis performance, no clear benefit was recognized and the decision was made to discontinue their use. The filtering process alters the data such that edge details are rounded off, making interpretation more difficult. The smoothing of data by a filter has an effect that is similar to a reduction in AFM resolution, which is not desirable in this application.

5.3. Initial Topographic Analysis Efforts

A major conceptual breakthrough in this effort occurred when we realized that despite the way in which we normally see AFM data on the computer screen, i.e. as a 2-D false color image (Figure 26), the 3-D AFM data matrix contains fundamentally different information than a 2-D grayscale or false color image. Rather, it is more akin to the data matrix needed to describe a 3-D topographic map of a section of the Earth’s surface. As such, the AFM analysis tools developed in this work are based on a 3-D topographic approach.

New analysis tools were developed to surpass the aforementioned analysis issues and create a robust analysis system. Initially, a manual track analysis approach was developed that would provide enhanced feature identification with final track acceptance decisions made by the analyst. The various algorithms needed were designed and implemented in the Matlab software environment as command line functions. This method can be summarized as follows:

- convert the AFM data to a topographic map;
- manually select points on the edge of the track;
- calculate a least squares ellipse fit to the selected points;
- record ellipse features to a spreadsheet program;
- calculate reduced etch rate ratio and convert to LET.

To analyze an AFM scan of an area on a CR-39 PNTD, the AFM data file must be loaded from computer disk and the data parsed to separate the header information from the data matrix. The header data for an AFM scan file contains a listing of all of the system variable settings used to obtain the scan and is needed to convert the X, Y, and Z values in the data matrix to nanometers.

To analyze the 3-D data matrix, it is first converted to a contour plot. The contour plotting algorithm assigns regularly spaced isoclines to the data, resulting in a topographic map of surface features. A comparison between an AFM image and its associated contour plot is shown in Figure 29. When viewing AFM data in a contour plot, as opposed to a false color image, we observe that the most striking features are now related to nuclear track interiors as opposed to the surface of the detector. The isocline spacing can be readily interpreted visually, as in the reading of a topographic map, to understand changes in slope and to directly see the difference between conical and bowl shaped tracks. In an AFM image, it is common for all track interiors to appear to be the same dark color, which can easily be misinterpreted. Using the contour plot, the same track interiors are shown to be highly detailed. Surface roughness and dust are very apparent in an AFM image, since the color map is designed to enhance all surface details. In the topographic display, all contours lying above the mean surface value can be rejected, making analysis less difficult.

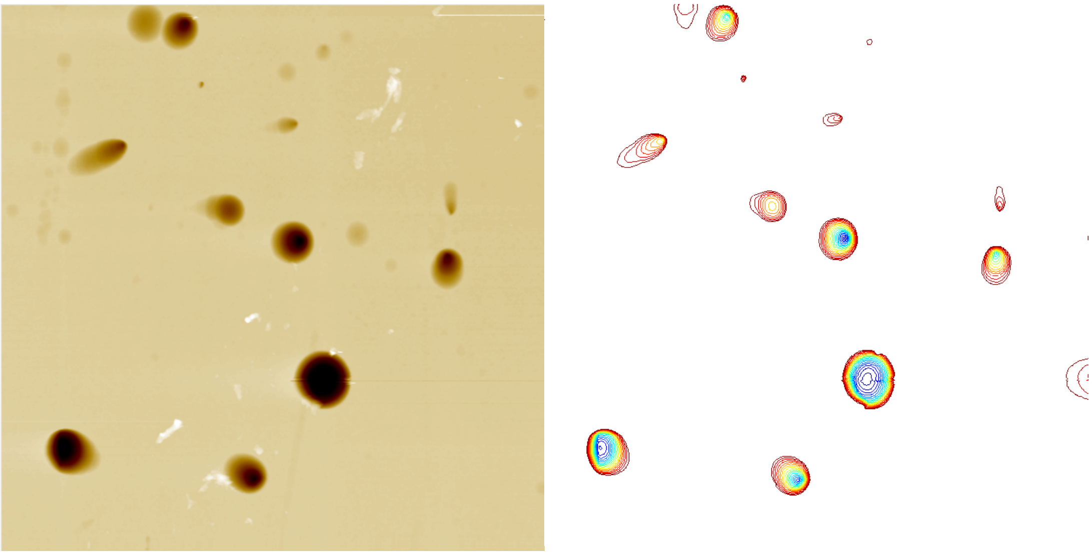

Figure 29. Comparison between AFM data shown in a false color image (left) and in a topographic mapping (right). Regularly spaced isoclines permit examination of the change in slope inside nuclear tracks. Additionally, minor surface features lying above the average surface contour are rejected.

Following generation of the contour plot, an algorithm was used to manually collect a series of points (>15) around the perimeter of each track [Doke, 2005]. Then, an over-determined least squares ellipse fitting [Halíř et al., 1998] is applied to the set of selected points. With least squares fitting applied to the ellipse edge points, the track interpretation is much less reliant on analyst skill or color map properties. The topic of ellipse-specific, least squares ellipse fitting is discussed in greater detail in the next section.

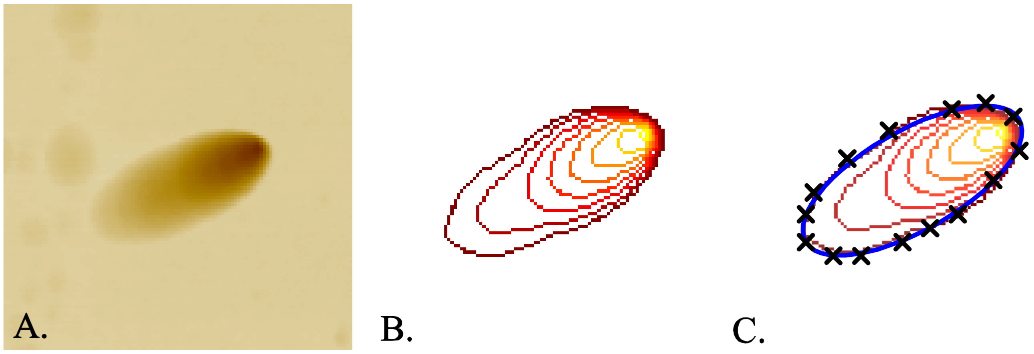

Figure 30. This figure shows an elliptical nuclear track in the amber color map at left (A) and in topographic display (B). The top-most contour can be used to identify the track edge and select points (×'s in black) for an ellipse fit, as in C.

The overall process used in the first topographic analysis method, summarized in steps A, B, and C in Figure 30, is labor intensive and time consuming, primarily due to the manual selection of track edge points. On the other hand, topographic analysis, coupled with least squares ellipse fitting, immediately proved to be a more accurate and effective approach, in comparison to the use of the section analysis tool. It was clear that further improvements could be made that would automate the selection of track points along the tracks perimeter, as well as improve other aspects of the analysis.

5.4. Second Effort: Semi-Automated Topographic Analysis

The semi-automated analysis method presented here uses several algorithms to prepare the AFM data, isolate track candidate (TC) data from the matrix of AFM data, and calculate ellipse properties needed for LET determination. The net result is a method that no longer requires manual edge point selection for each TC, but requires analyst acceptance for each analyzed AFM scan, hence the term “semi-automated”. In AFM data processing, it is important to manipulate the AFM data as little as possible, which precludes the use of false color mappings (except for graphic display purposes), data filters, or the implementation of phase correction algorithms. The semi-automated methods presented in this section are designed to modify the source data as little as possible.

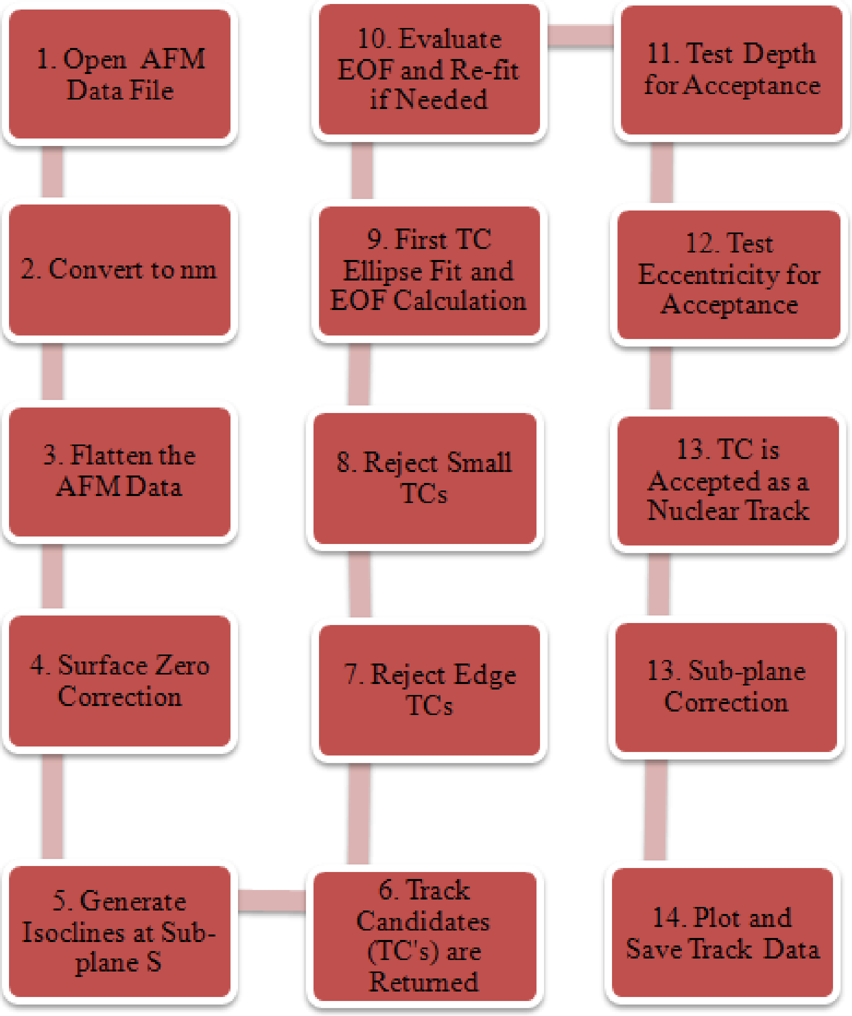

Figure 31. Flowchart showing the steps performed in the semi-automated AFM data analysis process.

5.4.1. Algorithm for AFM Data Analysis

The process flow-chart for the AFM data analysis algorithm is shown in Figure 31. The order of operations is critical with the exception that the depth and ellipticity criteria can be applied in either order. Portions of this process were described in Section 5.3, specifically Step 1: ‘Open AFM Data File’, and Step 2: ‘Convert to nm’. Additionally, Step 14: ‘Plot and Save Track Data’ is trivial and is not discussed.

5.4.2. Flattening Algorithm

This section discusses the execution of Step 3: ‘Flatten the AFM Data’ in Figure 31. After opening the AFM data file and isolating the scan data matrix from the header data, it is necessary to remove the effects of scanner head drift that occur during scanning. Scanner head movements are normal and expected as the scan head is adjusted to ensure proper surface tracking. The adjustments are evident in the AFM data as horizontally oriented lines. These lines are normalized to the mean surface value by performing a line-by-line polynomial subtraction. For each row in the scan data matrix, a third order polynomial least squares fit is made to the data. This polynomial is then subtracted from the row of data. This process is sometimes referred to as polynomial de-drifting, flattening, or flatting. A composite output matrix consisting of the corrected row data is produced for further analysis. The flattening process has no discernable influence on the interpretation of nuclear tracks in later steps.

The problem of obtaining a least squares fit to data is of general interest, with many varied approaches [Björk, 1996]. Solutions to this problem were originally proposed by

Gauss in 1795. For this application, a computationally efficient fitting process was required. The flattening algorithm used in this work [Pastushenko, 2006] uses a Vandermonde matrix approach to the least squares polynomial fitting [Gemignani, 1999]. Each AFM scan line is fitted by finding the solution to the general least squares problem:

$$\min_{x} \|Vx - b\|_2 \ , \tag{5.1}$$

where the notation, $\|...\|_2$, denotes the Euclidean vector norm. In this case the vector 2 norm is simply the Euclidean length of the vector. In equation (5.1), V is an $n \times n$ Vandermonde matrix of the form:

$$V = \begin{pmatrix} x_1^{n-1} & x_1^{n-2} & \dots & x_1 & 1 \\ x_2^{n-1} & x_2^{n-2} & \dots & x_2 & 1 \\ \dots & \dots & \dots & \dots & \dots \\ x_n^{n-1} & x_n^{n-2} & \dots & x_n & 1 \end{pmatrix}, \tag{5.2}$$

and the matrices x and b are column matrices of length n. The solution to (5.1) takes the form:

$$Vx = b \, , \tag{5.3}$$

to which matrix left division is applied. This is the same as the matrix inverse of b times V, yielding:

$$x = b \backslash V \, . \tag{5.4}$$

The elements of the matrix, x, are the coefficients of the polynomial fitted in the least squares sense.

5.4.3. Surface Zero Correction

This section discusses the details of Step 4, in Figure 31. For consistent application of analysis system variables to AFM data, it is important to present the same zero level for each AFM scan in the later analysis steps. It is common for the apparent surface plane to shift up and down by 100 to 200 nm between successive scan frames. This effect can be problematic when calculating track depth, for example, which is used as a track acceptance criterion. To remove the effect of planar offsets, an algorithm was developed to identify the actual surface height and then subtract this value from the entire AFM data matrix. The input AFM data matrix, I_{in}, is modified as follows,

$$I_{out} = I_{in} - I_{offset}, \tag{5.5}$$

where, I_{offset} is determined using a histogram to sort the AFM data matrix height values from lowest to highest, as shown in Figure 32. The maximum value of this histogram, e.g. the peak count bin corresponds to the actual surface of the detector. An exception to this condition occurs when the AFM data contains many nuclear tracks or surface artifacts, but this is a rare occurrence with proper scanning techniques.

In Figure 32, (top-left) AFM data were obtained from a scan of a 10 μm × 10 μm grid reference, which has ~ 200 nm deep square pits etched in an array. The histogram of the height data (top-right) shows the surface value at 50 nm and the pit depths to be at -130 nm. The surface zero correction is implemented, in this case by subtracting 50 nm from the data, thereby presenting a data set with the surface value at zero. The bottom-left figure shows data from an AFM scan of a CR-39 PNTD and its histogram on the bottom-right shows that the uncorrected surface height is approximately 105 nm prior to surface zero correction.

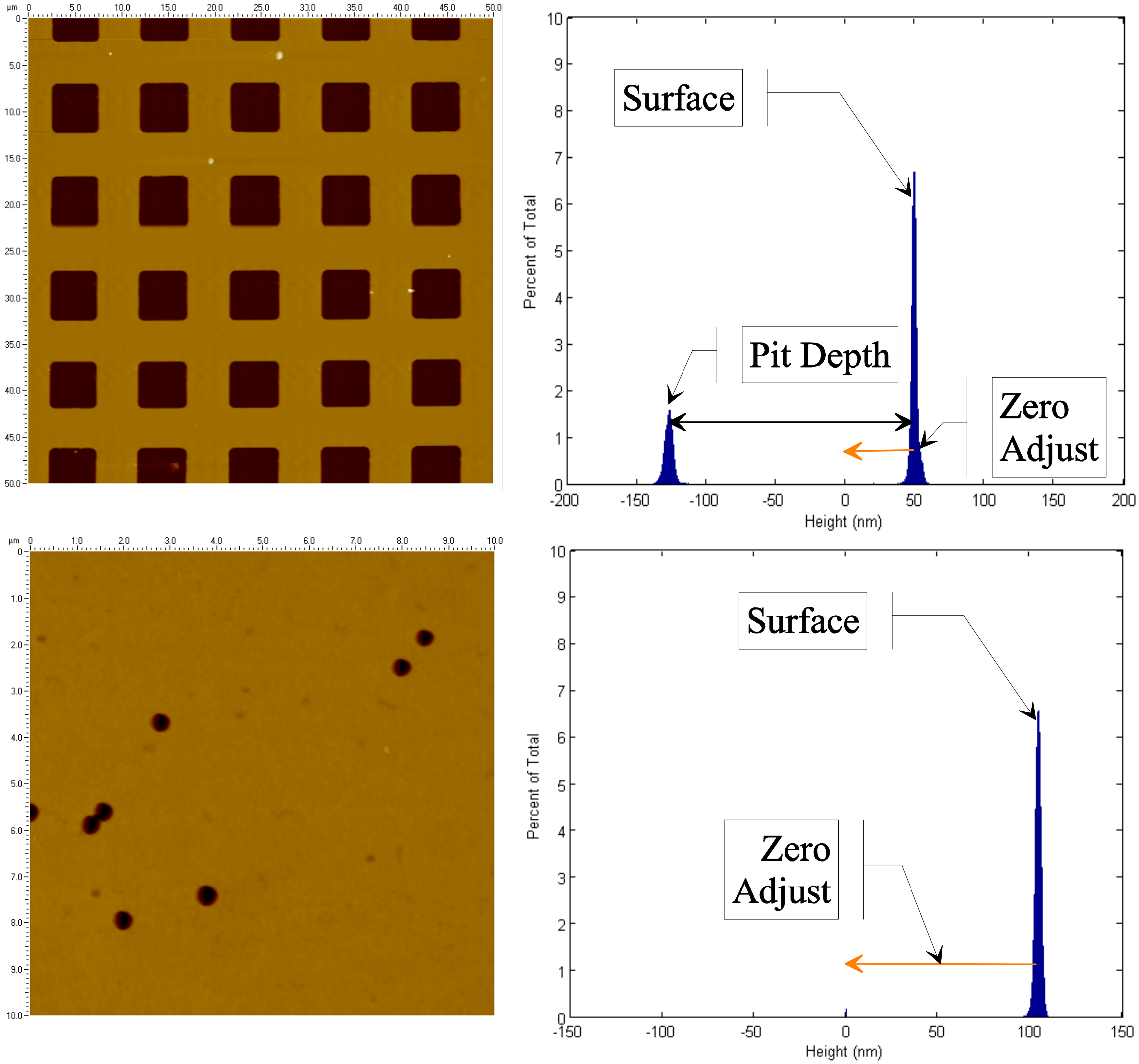

Figure 32. The surface height correction algorithm calculates a histogram of the AFM data to determine the peak count bin, which corresponds to the surface zero value.

5.4.4. Topographic Analysis

In this section, Steps 5 through 8 of Figure 31 are discussed. After scanner drift effects and surface zero offset have been corrected, a topographic analysis is performed. This analysis generates a set of track candidate (TC) matrices at a fixed depth below the surface for each AFM data matrix. A general algorithm for contour generation parses the matrix for each value within some small range of the desired depth. The depth below the surface is called the analysis sub-plane, *S*. The algorithm for finding the i^{th} point, *P*, on an isocline has the form (in set notation):

$$P_i\left(x_i, y_i, z_i\right) = \left\{z_i \in I : S - \delta \leq z_i \leq S + \delta\right\}, \qquad (5.6)$$

where δ is a small, but non-zero value ($\delta = \ S$) and *I* is the set of source data. For each AFM scan, a set of TC matrices are returned in which each TC matrix contains the contiguous points *P* belonging to a single surface feature. This operation accomplishes Steps 5 and 6 of Figure 31.

For data from 50 μm × 50 μm scans of CR-39 PNTD with a *B* of 0.5 μm, the optimal value of *S* is typically 5-10 nm. This was found empirically to produce the fewest false tracks. If *S* is chosen to be too close to the detector surface plane, very many small features attributable to surface noise are passed to the subsequent analysis steps. If *S* is chosen to be too large, some tracks could be excluded from analysis or the measured track shape may be altered by the appearance of the AFM tip artifact, as discussed later in Section 5.5 and illustrated in Figure 35.

TCs with fewer than 15 points in the matrix are automatically omitted from analysis, thereby accomplishing Step 7. Such TCs can represent small, lower LET tracks. Even though the least squares ellipse fit would work with as few as 5 points, there would be insufficient data present in the track interior to enable further testing for acceptance. Due to the slope of the AFM tip edges, and the surface sampling separation, a TC with less than 15 points would be indistinguishable, both from another similarly sized TC and from surface noise normally present on the surface of the etched detector.

To accomplish Step 8 of Figure 31, tracks near the edge of the scan frame are rejected. It would be technically feasible to attempt an ellipse fit to a portion of a TC, but the fitting error would increase and further tests for acceptance would, in general, not be possible. The area rejected in this step is accounted for in later analysis steps to ensure that the total area scanned on a given detector is correct.

5.4.5. Least Squares Ellipse Fitting

After the contour plot operation is complete, the matrix is analyzed to locate and isolate all TCs present in the scan. Each TC has an associated matrix of edge points in X and Y that were obtained at the depth *S*, below the detector plane. The collection of TC matrices is then iteratively processed and a least squares ellipse fit, as shown in Figure 33, is applied to each TC matrix to achieve Step 9 of Figure 31. This ellipse fit, and the verification of its accuracy using an estimate of fitting algorithm (see section 5.4.6), increase analytical accuracy and represent a significant advantage of this method. The TC matrix analysis results in the determination of *a* and *b* for the ellipse fitted to the TC data points. Taken together, *a*,*b*, and *B* are used to calculate V_R, which is, in turn, proportional to LET.

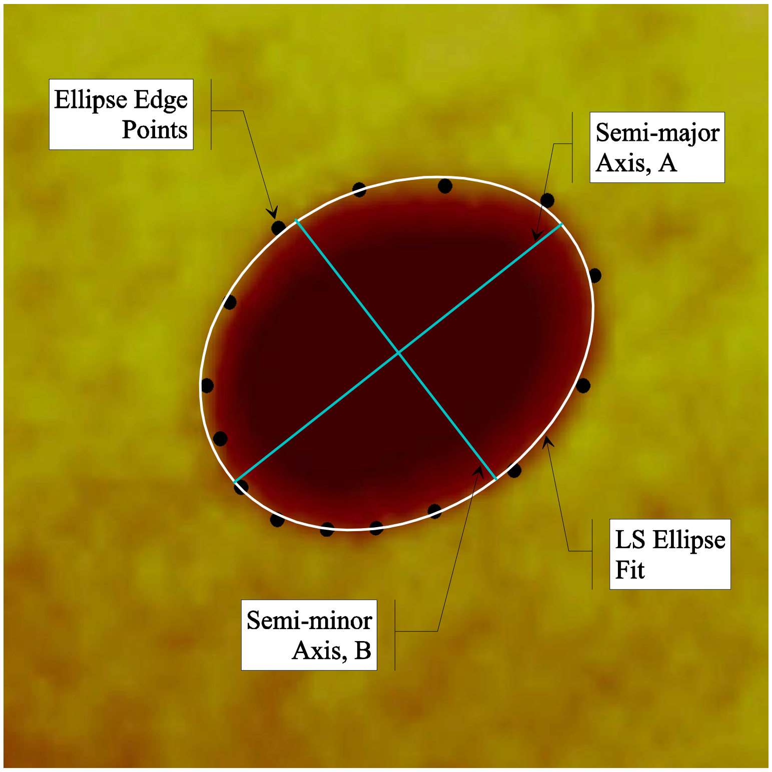

Figure 33. Ellipse specific least squares fitting applied to non-uniformly spaced data points.

There are numerous methods for fitting conic sections to data [Bookstein, 1979; Zhang, 1997; Haliř et al., 1998; Fitzgibbon et al., 1999]. An ellipse specific least squares method was implemented, which assumes that the data to be fitted represents an ellipse or possibly a circle, and not a hyperbola. This approach emerged in parallel with applications of machine vision systems. The mathematics of precisely locating a motherboard on a conveyor belt using a machine vision system or of locating the cranium of a fetus in ultrasound data are very similar to that of identifying nuclear tracks on the surface of an etched CR-39 PNTD. More sophisticated conic fitting algorithms have been developed, such as those based on Hough Transforms [Lu et al., 2008]. These algorithms are less sensitive to noise, but have not been necessary in this work since AFM data, when collected properly, are relatively artifact free.

The ellipse specific least squares fitting algorithm used in our analysis algorithm was developed by Fitzgibbon et al. [Fitzgibbon et al., 1995; Pilu et al., 1996] and later refined by Haliř et al. [Haliř et al., 1998]. Their method reduces the problem of least squares ellipse fitting to one of finding the solution to an eigenvalue problem, which is particularly attractive for computational purposes. The general equation of a conic section, in implicit form is:

$$\mathrm{F}(a, \mathbf{x}) = \mathrm{ax}^2 + \mathrm{bxy} + \mathrm{cy}^2 + \mathrm{dx} + \mathrm{ey} + \mathrm{f} = 0, \tag{5.7}$$

where the matrix, *a*, containing the ellipse parameters, and the vector **x** are defined as:

$$a = \begin{bmatrix} \mathrm{a} \\ \mathrm{b} \\ \mathrm{c} \\ \mathrm{d} \\ \mathrm{e} \\ \mathrm{f} \end{bmatrix}, \ \mathbf{x} = \begin{bmatrix} x^2 \\ xy \\ y^2 \\ x \\ y \\ 1 \end{bmatrix}. \tag{5.8}$$

The ellipse specificity is provided by the constraint, $\mathrm{b}^2 - 4\mathrm{ac} < 0$, which can be rewritten as $\mathrm{b}^2 - 4\mathrm{ac} = 1$ under the proper scaling. Defining the N×6 design matrix D and the 6×6 constraint matrix C:

$$\mathrm{D}=\begin{bmatrix} x_1^2 & x_1y_1 & y_1^2 & x_1 & y_1 & 1 \\ \cdots & \cdots & \cdots & \cdots & \cdots & \cdots \\ x_i^2 & x_iy_i & y_i^2 & x_i & y_i & 1 \\ \cdots & \cdots & \cdots & \cdots & \cdots & \cdots \\ x_N^2 & x_Ny_N & y_N^2 & x_N & y_N & 1 \end{bmatrix},\ \mathrm{C}=\begin{bmatrix} 0 & 0 & 2 & 0 & 0 & 0 \\ 0 & -1 & 0 & 0 & 0 & 0 \\ 2 & 0 & 0 & 0 & 0 & 0 \\ 0 & 0 & 0 & 0 & 0 & 0 \\ 0 & 0 & 0 & 0 & 0 & 0 \\ 0 & 0 & 0 & 0 & 0 & 0 \end{bmatrix}, \qquad (5.9)$$

and imposing the rewritten constraint as $a^T\mathrm{C}a=1$, Halíř et al. found that the least squares ellipse fitting problem became equivalent to finding:

$$\min_a \|\mathrm{D}a\|^2 . \qquad (5.10)$$

The solution to (5.10) is obtained by the use of Lagrange multipliers:

$$\mathrm{S}a=\lambda\mathrm{C}a , \qquad (5.11)$$

where S is the scatter matrix:

$$\mathrm{S}=\mathrm{D}^T\mathrm{D} . \qquad (5.12)$$

The solution is found by:

$$\|\mathrm{D}a\|^2 = a^T\mathrm{D}^T\mathrm{D}a = a^T\mathrm{S}a = \lambda a^T\mathrm{C}a = \lambda , \qquad (5.13)$$

in which the selection of $a_k^T\mathrm{C}a_k=1$ has been made in the final step. The ellipse defined by the elements of a_k is the least squares fit to the matrix of points provided. If the matrix of points to be fitted contains erroneous points, e.g. noise, surface aberrations, or points that belong to another nuclear track, the fitting process can be improved considerably by rejecting these points provided a reliable means exists to identify them as such.

The mathematical requirements to complete an ellipse specific fit are that a minimum of five points of data be used. This is due to the fitting algorithm; five points are needed for a well determined system since there are five unknown coefficients in the ellipse formula. In this work, a stricter limitation of 15 points minimum was chosen, leading to an over determined system, with the additional restriction that the 15 points be uniformly spaced around the ellipse perimeter. The increased degree of fitting restriction is primarily implemented to increase the overall accuracy of the analysis.

5.4.6. Estimation of Fit Accuracy

Following application of least-squares fitting to the data, the goodness of the fit is computed as part of Step 10 in Figure 31. The estimation of fit, or EOF [Rosin, 1996], represents the accuracy of an ellipse fit to the data presented. Operationally, the EOF algorithm computes the algebraic distance between each point of the data matrix to be fitted and the points of the fitted ellipse represented by:

$$EOF' = Q(x_j, y_j) = Ax_j^2 + Bx_j y_j + Cy_j^2 + Dx_j + Ey_j + F \ . \tag{5.14}$$

This fit is weighted by the gradient [Agin, 1981; Sampson, 1982; Taubin, 1991] as follows,

$$EOF = \frac{Q(x_j, y_j)}{\left|\nabla Q(x_j, y_j)\right|} \ , \tag{5.15}$$

where,

$$\nabla Q(x_j, y_j) = \left[\left(2Ax_j + By_j + D \right)^2 + \left(Bx_j + 2Cy_j + E \right)^2 \right]^{1/2} . \tag{5.16}$$

As the ellipse fit is improved, e.g. by omitting matrix points that do not actually belong to the elliptical track, the values returned by the EOF calculation get smaller because the distance between the fitted ellipse and the data points fitted is smaller.

5.4.7. Separation of Overlapping Tracks

Since an accurate ellipse fit is known to have small EOF values, it is possible to indentify both poor ellipse fits and bad regions within an ellipse fit by observing regions of a given fit with a high value of EOF. This property was used to develop an overlapped track separation algorithm. Overlapped tracks are separated in two steps. First an ellipse is fitted to the TC representing the overlapped tracks. The EOF is then calculated. Fortuitously, the maximum values of EOF, which are the regions of worst fit, exactly match the points at which two tracks intersect. Using this result, the original TC matrix is separated into two smaller matrices and a second ellipse fit is performed on each sub-matrix. Some of the edge points near the track intersection are rejected to enhance the accuracy of the second fitting. It was found that this algorithm works extremely well in identifying and separating overlapped tracks. The TC separation algorithm has also proven effective in instances where dust or artifacts are present on the edge of a track. In such cases, the algorithm removes regions of non-track data from the TC, which improves the accuracy of the fit.

Since triple overlapped tracks are extremely rare, the separation algorithm as currently implemented is only capable of separating two overlapped tracks. It would be possible to extend this algorithm to separate multiple overlapped tracks via an iterative process.

5.4.8. Track Acceptance Criteria

Following least squares ellipse fitting and separation of overlapped tracks, the track candidate (TC) is evaluated for acceptance as a nuclear track. There are many features that can have a post-etch appearance that is circular or elliptical. The advantage of topographic matrix analysis methods over image processing methods is most evident in this step. By performing direct matrix manipulations, it is possible to make many local calculations without having to correct for color mapping, contrast, brightness, etc. The following tests for track acceptance can be modified to suit the needs of the analysis. Additionally, new tests for track acceptance can be easily added to the process.

5.4.8.1. Depth

Some circular post-etch features are artifacts in the CR-39 PNTD from the plastic casting (manufacturing) process. These features can be found alone or are often found oriented together in a linear region on a detector. Actual nuclear tracks have a depth which is easily calculated for both circular and elliptical cases. For each TC, the depth is calculated at three points: the track center and at each of the two foci. The deepest point of the three is then compared to an empirically determined depth cut-off. Only tracks that are deeper than this value are accepted. The measurement of actual track depth from AFM data is not generally possible, as discussed in section 5.5. Rather the depth calculated here is used to eliminate shallow surface features that are not actual nuclear tracks, thereby accomplishing Step 11 in Figure 31.

5.4.8.2. Eccentricity

The eccentricity of an ellipse is defined as:

$$e \equiv \sqrt{1-\left(\frac{b^2}{a^2}\right)}, \tag{5.17}$$

where is a is the semi-major axis and b is the semi-minor axis. The values of eccentricity can be $0 < e < 1$ for ellipses, and for a circle, $e = 0$. The eccentricity of an ellipse is a measure of its elongation. Actual nuclear tracks have a limited range of eccentricity due to the nature of track formation and chemical etching process. As the dip angle of a track increases, the track becomes more elliptical for a given LET. This parameter is used as an acceptance criterion because some non-track surface features and image artifacts can also be highly elongated and elliptical in appearance. An example of this is situation occurs when there has been incomplete image flattening that leaves behind horizontal features which are not nuclear tracks.

For each TC, the eccentricity is calculated and only TCs with eccentricity below an empirically determined threshold are accepted, thereby completing Step 12 in Figure 31. This threshold is called the eccentricity cut. It was found empirically that the semi-major axis, a, of real nuclear tracks is rarely greater than 8 times the value of the semi-minor axis, b. The eccentricity cut can be set to a smaller value, e.g. if one is interested in only the nuclear tracks of normally incident particles.

5.4.9. Analysis Sub-plane Correction

A TC matrix that has passed the previous tests for acceptance is now considered a nuclear track matrix. After a TC has been confirmed to be a nuclear track, the effect of the analysis sub-plane, *S*, must be removed. Since the TC matrices were obtained below the surface, the measured ellipse dimensions will be slightly smaller than the dimensions that would be obtained at the surface. This fact arises since the AFM measurement is made on the interior surface of an inverted cone. To compensate for this effect, the surface gradient is calculated in the track interior, and the slope value is used to project the ellipse up from the analysis plane, *S*, and onto the actual surface to obtain the correct values of the semi-major axis and semi-minor axis for each ellipse. It was observed that for a modest range of *S* values, roughly 5-15 nm below the surface, the same final ellipse is obtained. This is an expected result, since the interior of the track cone typically has uniform slope, unless LET is changing rapidly. Following projection onto the surface, the final values of ellipse semi-major axis, *a*, and semi-minor axis, *b*, are calculated to accomplish Step 13 in Figure 31.

As one final acceptance criteria, nuclear tracks with a semi-minor axis, *b*, greater than the bulk etch, *B*, are rejected. High LET charged particles, e.g. those with $\text{LET}_{200}\text{CR39} \geq 1500$ keV/μm, are known to saturate the detection capability of the CR-39 PNTD. The result is that all LET's above the saturation value will have nearly the same cone angle. It is assumed that real nuclear tracks will always have $b \leq B$. Occasionally there is a circular or elliptical TC with $b > B$. Such features are not common, but must be rejected as they cannot be tracks consistent with the calibration. This criterion is applied last to avoid eliminating actual nuclear tracks from analysis.

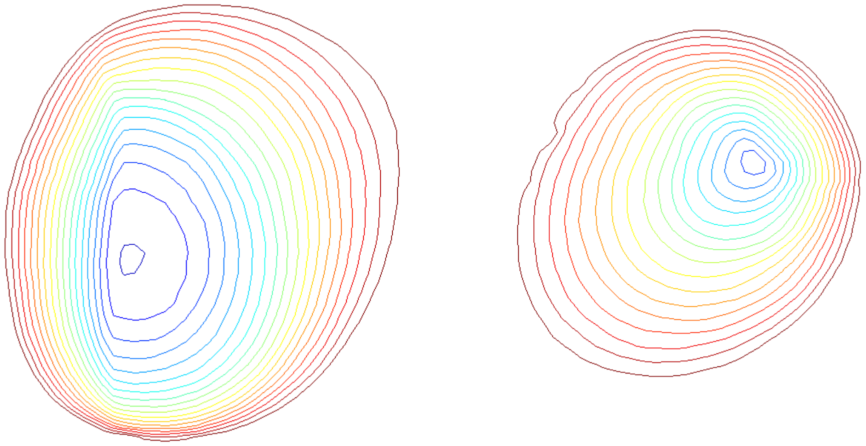

Figure 34. The AFM tip artifact is shown inside two nuclear tracks from the same AFM scan. The right hand portion of the track on the left is well sampled, while the left hand portion has a constant slope below the fifth contour. This slope is the tip profile and not the actual track interior slope. The track on the right appears to be well sampled for most of the track cone except for a portion in the upper right side.

5.5. Interpretation of Depth Measurements

The track interior measurements, including track depth, must be interpreted with caution. Since the AFM tip has a radius of curvature that is fixed, no detail finer than that allowed by the shape of the tip can be measured. Additionally, the shape of the tip is roughly an inverted pyramid with an elongated profile. In the scanning of nuclear tracks, a breakdown of measurement accuracy is encountered below a certain depth inside the track as shown in Figures 34 and 35. This is an artifact of the sampling process and the shape of the AFM tip, and cannot be overcome by making scanner setup adjustments. We refer to this as an AFM tip artifact. Ellipse fitting and other operations must not be based on data below the region of the tip artifact. For an annular region, near the post-etch surface of the CR-39, accurate measurements can be made.

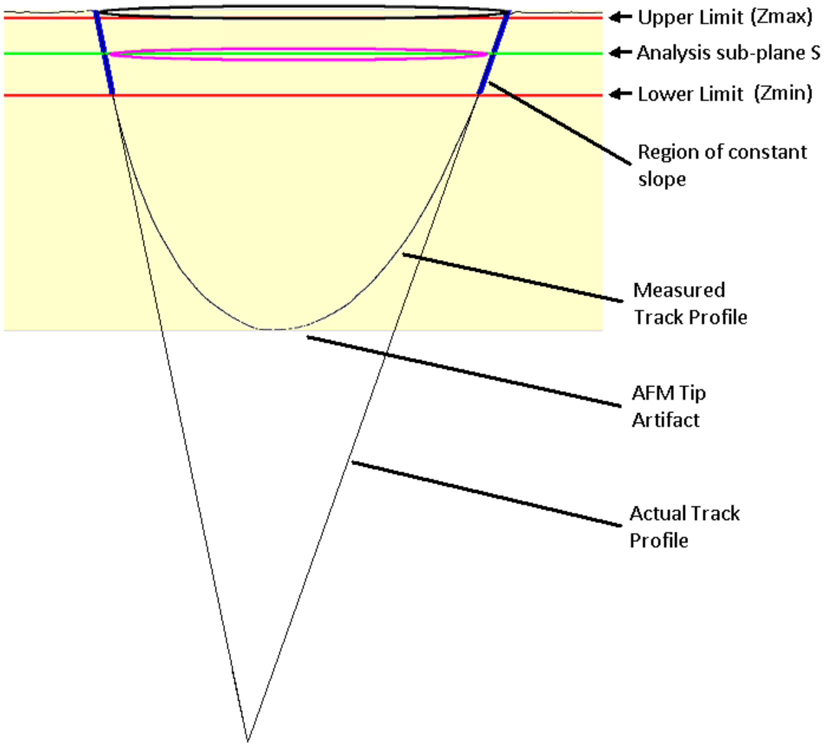

Figure 35. Cross sectional view of a nuclear track with the AFM trace shown to illustrate the tip artifact. The analysis of the track must be performed such that $Z_{min} < S < Z_{max}$ for accuracy.

5.6. Calibration of AFM/CR-39 PNTD Analysis Methods

A calibration or response function is needed to convert the analysis results, i.e. the individual track measurements of reduced etch ratio (V_R-1), into units of LET_{200}CR-39 (keV/μm). This is accomplished by using detectors exposed to various mono-energetic heavy ion beams, each with a different but known value of LET_{200}CR-39. The particle beams are selected such that their collective LET range spans the sensitive range of CR-39 PNTD. Following beam exposure, the detectors are etched and scanned with the AFM using settings identical to those used in analysis of experimental CR-39 PNTD. Any systematic analysis error is thereby incorporated into the calibration curve.

For each calibration detector, the semi-automated analysis system was used to measure the population of nuclear tracks present on its surface. Figure 36 shows calibration data for a detector exposed to 421 MeV/n Fe^{56}, which has LET_{200}CR-39 of 273.8 keV/μm. From this analysis, it is found that the mean V_R for this LET is 2.113 ± 0.112.

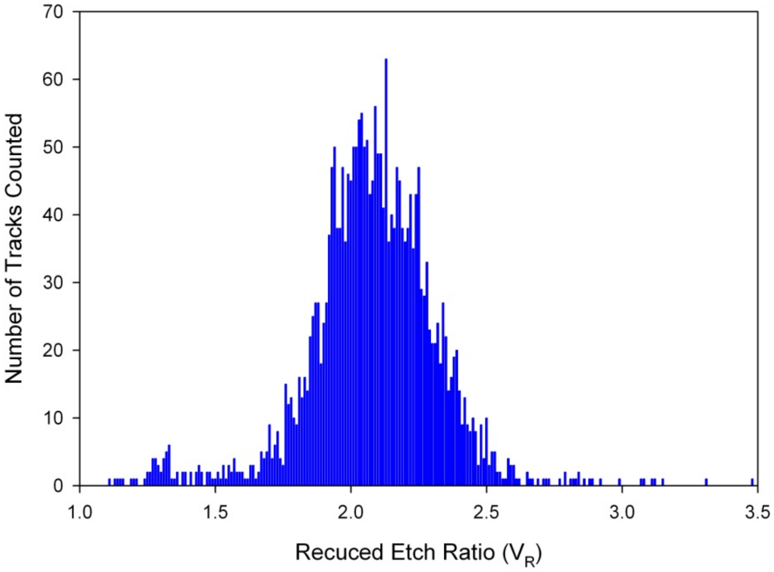

Figure 36. Track data obtained from a calibration detector exposed to 421 MeV/n Fe^{56} and analyzed using semi-automated analysis methods.

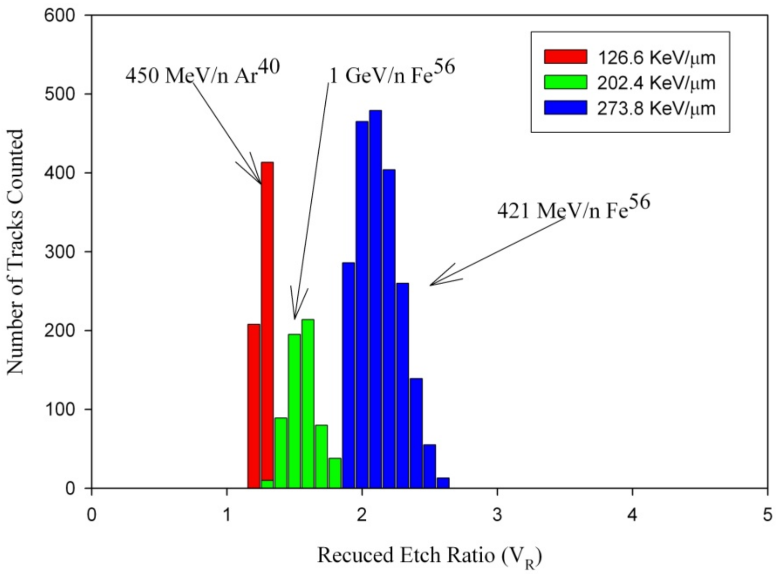

Figure 37. Histograms of data obtained for three different LET values used for calibration.

In the semi-automated analysis method, since all of the nuclear tracks present on a detector’s surface are measured, the potential exists to introduce track measurements from charged particle sources other than those constituting the primary beam. A second, smaller population of tracks with measured V_R ~1.3 can be seen to the left of the main peak in Figure 36. Tracks contributing to this population likely originated from projectile and target fragmentation reactions and do not represent the primary beam LET. These tracks are omitted from the data prior to determination of the average reduced etch rate ratio, V_R. Figure 37 shows histograms for three calibration detectors.

Measured average values of V_R-1 from each calibration detector are plotted against the known values of LET_{200}CR-39 and a least squares polynomial is fit to the resultant points. Figure 38 shows the analysis results from all calibration detectors and the calibration curve obtained from least squares fitting to the data. The calibration curve is of the form:

$$y = \log_{10}(LET_{200}CR - 39)\,, \tag{5.18}$$

$$x = \log_{10}(V_R - 1)\,, \tag{5.19}$$

$$y = A_1 + A_2 x + A_3 x^2 + A_4 x^3\,. \tag{5.20}$$

For CR-39 PNTD used in this work and etched for a *B* of 0.5 μm, the coefficient values were determined to be; A_1 = 2.3085583, A_2 = 0.6574401, A_3 = 0.442262, and A_4 = 0.4392032. This functional form is integrated into the analysis software.

It is necessary to convert the measured data from $\mathrm{LET_{200}CR\text{-}39}$ to $\mathrm{LET_{\infty}H_2O}$ in order to make comparisons to measurements made by other detectors. This conversion is achieved using the following formula [Benton, 2004]:

$$\log_{10}(LET_{\infty}H_2O) = 0.1689 + 0.984\log_{10}(LET_{200}CR - 39)\,, \tag{5.21}$$

in which the coefficients have been empirically determined. This conversion was based on an analysis of the Range/Energy relations [Benton et al., 1969a]. For the remainder of this document, LET will be used in the place of $\mathrm{LET_{\infty}H_2O}$ unless otherwise noted.

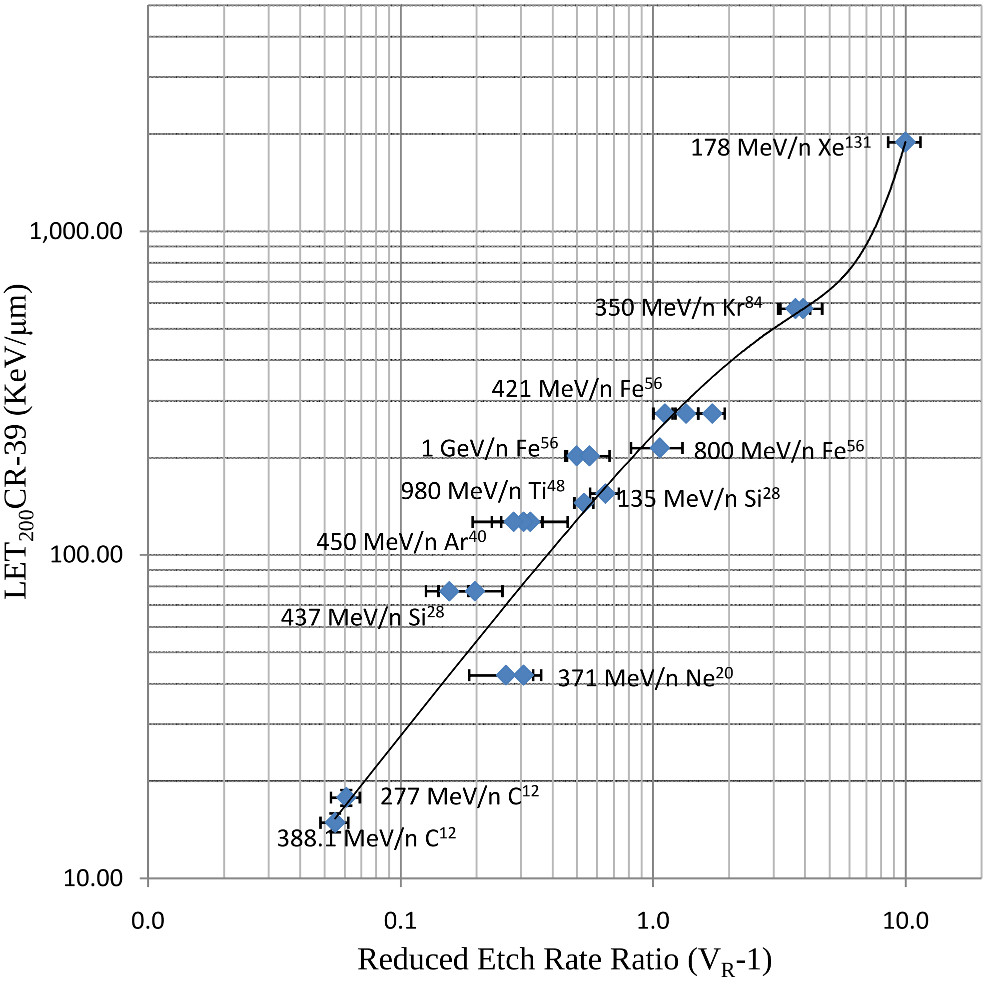

Figure 38. The calibration curve for AFM/CR-39 PNTD semi-automated analysis method is shown with the particle beam composition and energy values used.

As previously mentioned, AFM scan size selection imposes a limit on the minimum LET the AFM is capable of measuring. Therefore calibration detectors exposed to low LET beams cannot be reliably analyzed using large area scans, e.g. 50 µm × 50 µm, and must be scanned at a suitable scan size, such as 20 µm × 20 µm or less. Multiple calibrations for each scan size were found to not be needed however, since nuclear track measurements made with AFM are consistently in nanometers and are accurate regardless of scan size.

A variation in analysis parameters, such as an increase or decrease in bulk etch value, requires determination of a new calibration curve obtained under the new conditions. Due to the time and expense of obtaining a new calibration function, experimentation with various etch parameters is prohibitive. There are some instances in which it would be worthwhile though, e.g. for a 4 hour (1 μm) etch which would provide low LET_{200}CR-39 sensitivity for 50 μm × 50 μm scans.

5.7. Further Improvements

The methods presented in this chapter can be naturally extended to provide additional information about the particles that form nuclear tracks. Preliminary work has been completed on enhanced analysis tools that repeatedly sample the AFM data matrix at multiple levels, as shown in Figure 39. The least squares ellipse fit is applied to the data at each of the levels in turn and the resulting value of track LET can be derived from the analysis of hundreds of data points instead of the minimum 15. This could be used to calculate the track length, *L*, which is also proportional to LET.

While a multiple level, volumetric approach would have obvious advantages, its implementation would require extensive modifications to the current procedure. The value of bulk etch currently used would more than likely need to be increased from 0.5 μm to 1 or 2 μm. The reason for this is that the post-etch track appearance for most tracks is too small to be sampled adequately for reliable multi-layer analysis. Instead of increasing the bulk etch value, smaller scan sizes could be used, but smaller scan sizes would fail to adequately sample short-range, high-LET tracks unless many such scans were performed, resulting in a large quantity of scans and increased scan time. A multi-layer analysis approach based on this method will require robust discrimination between actual track interior data and AFM tip artifact related data.

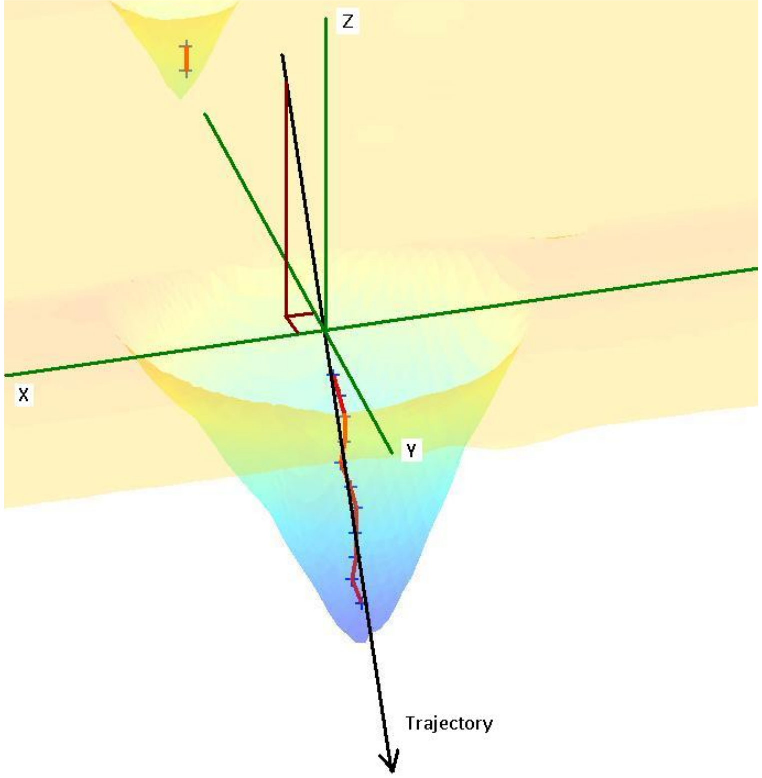

Figure 39. A novel track reconstruction algorithm has been developed that is capable of extracting all relevant nuclear track properties. The algorithm is currently only effective under certain conditions and further development would be required to integrate this method into a calibrated analysis system.

One possible extension of the volumetric approach would be to use the multi-layer analysis previously discussed to extract input data for a three dimensional cone fitting algorithm such as the 3L algorithm [Blane et al., 2000]. Using the 3L algorithm, as few as 3 layers of analysis (based on our existing method), could be used to perform a conic section fitting. If the 3 input surfaces were selected above the height of the tip artifact, the fitted cone would represent the track cone with reasonable accuracy. In the general case, in which the interior of the track cone attains a measurable curvature, such as the case for charged particles with rapidly changing LET, another algorithm will be needed.

CHAPTER VI

PROTON BEAM EXPERIMENTS

In this chapter, the experiments carried out to demonstrate the efficacy of the CR-39 PNTD/AFM analysis methods and to collect preliminary data on HNR particle tracks in CR-39 PNTD are described, with an emphasis on the techniques used while exposing detectors at particle accelerator facilities. A track classification schema is introduced that is useful to categorize the various types of track-producing charged particles. A complete detector analysis using the methods of the previous chapters is presented, and the features of the resulting LET spectra are explained. The results from the remainder of the protons beam experiments are then discussed.

6.0 Detector Preparation and General Considerations

To study short-range, high-LET HNR particle tracks in CR-39 PNTD, experiments were carried out using the 250 MeV proton synchrotron at LLUMC and the 1 GeV proton beam at the BNL NSRL. The detectors exposed to particle beams were arranged in a stack configuration, which consisted of two CR-39 PNTD layers with a known material placed between them, as shown in Figure 40. Target materials included a range of materials, primarily metal foils ranging in Z from 3 to 80. For each combination of proton beam and target, a separate detector stack was prepared, exposed, etched (see

Chapter III), scanned with the AFM (see Chapter IV), and then analyzed using the methods presented in Chapter V.

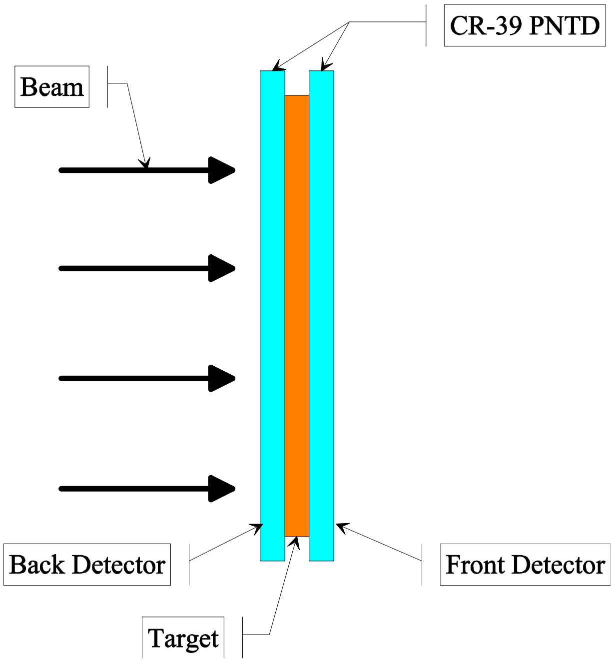

Figure 40. CR-39 PNTD stack with a target inserted between two detector layers. The sensitive sides of the PNTDs face the target material. The detector on the right is called the front detector because particles that enter this detector from the target are traveling in the forward direction (with the beam).

Target foils are held in position during beam exposure by small pieces of adhesive tape applied on the edges. Careful attention was given to detector positioning and beam monitoring during the beam exposures. It was also necessary to scribe a unique serialization onto each detector for identification during later processing steps. Additionally, all activities at the accelerator facility were recorded in a log for later reference.

Because target fragmentation reactions can occur in both the target and the detector, the exposed CR-39 PNTDs contain HNR particle tracks from nuclear interactions that occurred in both materials. It is necessary to distinguish between secondary particles produced in the target layer and those produced in CR-39 PNTD itself. Secondary particles produced within the PNTD itself are referred to as the internal component. To measure the internal component, detector stacks are exposed in which target material is omitted and the CR-39 layers serve as both detector and target. The contribution of the internal component is subtracted from that of the target layer as described below.

The beam exposure is monitored at each accelerator facility and recorded in units of dose in water. From the measured beam dose, the beam fluence is calculated using equation (3.19), since the primary beam can be considered mono-energetic. The fluence for each beam exposure is then used to determine the normalized differential fluence for each experiment.

6.1. Secondary Particle Formation Regions

Track forming charged particles can be produced in a number of regions throughout the detector/target assembly during a given exposure. In Figure 41, a number of possible nuclear track producing events are illustrated with respect to depth through a given detector stack. The detector/target assembly is divided into four regions. Region 1 consists of the detector closest to the beam source and is referred to as the back detector. Region 2 encompasses the interface between the back detector and the target, while Region 3 encompasses the interface between the target and the detector farthest from the beam source (referred to as the front detector). Finally, Region 4 consists of the front detector.

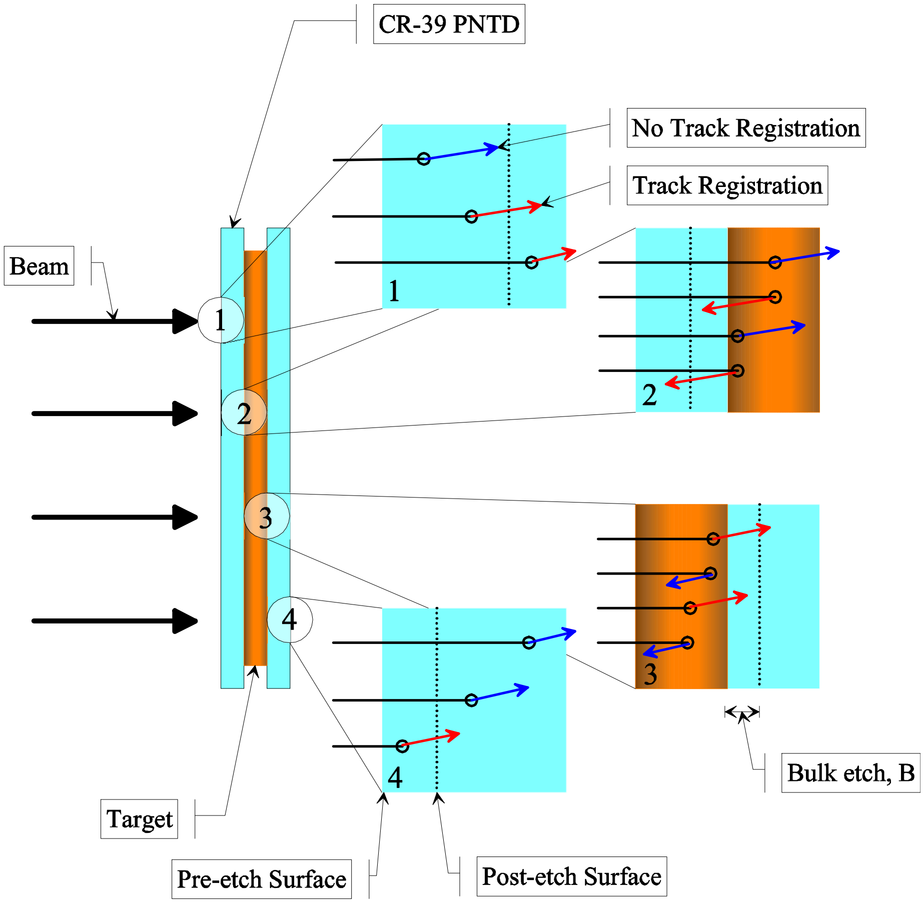

Figure 41. Diagram showing the various possible nuclear reaction outcomes at four separate depths (regions) inside the detector stack. Nuclear reactions that generate secondary particles are shown as black circles. If the secondary particle registers a nuclear track in a PNTD, it is shown with a red vector; otherwise a blue vector is shown. The length and direction of the red and blue vectors are for illustrative purposes only.

In Region 1, primary beam particles penetrate the back detector and can undergo inelastic nuclear collisions as discussed in Chapter II. Secondary particles formed in these collisions can vary in composition (Z), can be emitted in any direction, and can have a range of velocities. As shown in the Region 1 inset, the possibilities include, from top to bottom: undetected internal secondary particles, detected internal secondary particles that stop traveling inside the volume of detector material later removed by etching, and detected internal secondary particles formed inside the volume of detector material removed by etching and that pass into the target layer.

In Region 2 of Figure 41, in order to produce nuclear tracks in the back detector, secondary particles produced in the target layer must travel in the backward direction (relative to the primary beam). The nuclear tracks measured in this region consist of forward traveling secondary particles produced in the back CR-39 PNTD layer (internal) and backward traveling secondary particles produced in the target layer. This latter component consists of the HNR particle tracks of interest in our analysis. Region 3 is similar to Region 2 except that the directions of travel for the internal and target secondaries are reversed. Again, it is the forward moving HNR particles produced in the target and registering tracks in Region 3 that are of interest. Additionally, in Region 3, a greater component of forward travelling knock out particles, light charged particles, and intermediate mass fragments are expected, all of which have momentum peaked in the forward direction (parallel to the primary proton beam).

Region 4, the inset detail of the front detector, shows internal nuclear reactions that produce detected and undetected secondary particles. In this region, the detected internal secondary particles must travel in the backward direction, this places a constraint on the type of particle that can cause an internal nuclear track in this region. Since knock-out particles are peaked in the forward direction, few of these particles are expected to produce tracks in the front detector, leaving backward traveling HNR particles as the predominant internal component in this region.

6.2. Track Classification Schema

The following track classification schema was created to categorize the various possible track producing reactions. The purpose of the track classification schema is to exhaustively categorize all events which produce tracks in CR-39 PNTD in this type of experiment. Despite the exhaustive categorization, it is understood that nuclear tracks found in the post-etch surface of a detector are not generally identifiable as belonging to one group or another, although in some instances this identification is possible. The need for a track classification schema arises from the issue of separating the CR-39 PNTD internal component from the component produced in the target. This subtraction is analogous to measurements of background radiation level used by low background counting facilities to make corrections in laboratory counting experiments.

In beams with a particle and energy combination that results in an LET in excess of 5 keV/µm, a primary particle will produce a nuclear track in CR-39 PNTD. Tracks of primary particles are readily distinguishable from other tracks due to the fact that they will have an LET consistent with the beam LET and they will be normally incident on the surface of the detector. The post-etch appearance of this track type is a conical pit with a nearly circular opening at the surface of the detector. This type of nuclear track is classified as RP, for track registering primary particle. An example of this type of track is found in the calibration detectors used in our work, in which most tracks present can be classified as RPs.

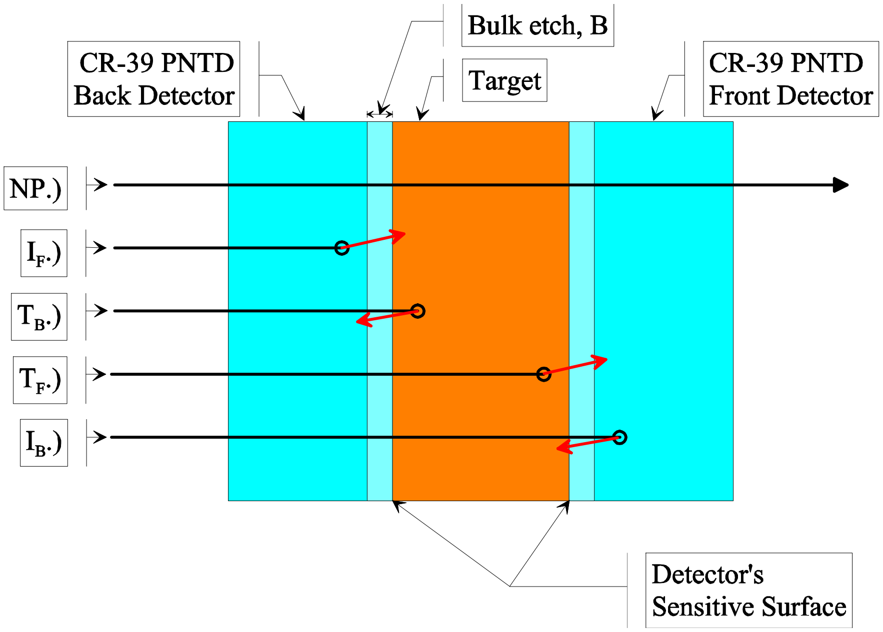

Figure 42. Illustration showing the various possible source locations of nuclear track producing charged particles within a detector stack. The most common event classification for proton beam exposures is NP, i.e. no nuclear reaction occurs. The remaining classes are discussed in the text.

For the majority of beam exposed detectors analyzed in this work, e.g. proton exposures, the primary particles do not register. In Figure 42, this situation is depicted as the NP trajectory (an abbreviation for non-registering primary particle), in which the primary particle passes through the detector without generally undergoing an inelastic nuclear reaction. NP class events are by far the most common in proton beam exposed detectors by a factor of approximately 1000.

Table 6.1- Classification of nuclear tracks in CR-39 PNTD exposed in target fragmentation experiments.

Event Class	Origination Layer	Constituents	Characteristics
I_F	Back detector	Intra-nuclear cascade knock out particles Intermediate mass fragments Evaporation nucleons HNR particles	HNR particles from C and O nuclei only
I_B	Front detector		
T_F	Target layer's, outer surface near front detector		HNR particles with Z up to target Z
T_B	Target layer's, outer surface near back detector		

Target fragmentation reactions that occur inside the detector have the classification I and can be emitted in the forward or backward direction. The nomenclature I_F and I_B, are used to distinguish forward and backward traveling internal tracks, respectively. For target fragmentation reactions occurring inside the target layer, the classification T is used. The classifications T_F and T_B represent forward travelling and backward travelling particles, respectively. Using this classification, the front detector (on the right hand side of Figure 42) will register nuclear tracks from classes T_F and I_B only. Similarly, the back detector will only register nuclear tracks of types T_B and I_F. The various types of tracks occurring in CR-39 PNTD exposed in target fragmentation experiments are summarized in Table 6.1.

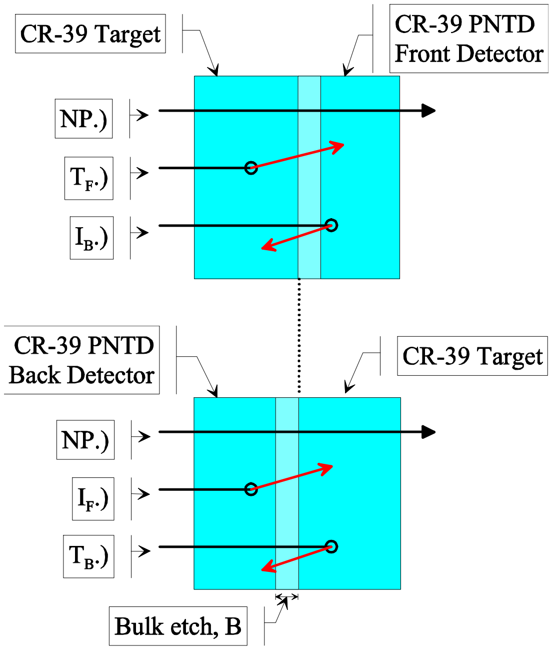

Figure 43. Illustration showing the possible types of detected tracks for the case where target material has been omitted. For the front detector (top) the back detector is the target, and for the back detector (bottom) the front detector is the target. The dotted line in the center represents the analysis plane of each detector.

The result of an individual detector analysis is expressed in terms of normalized differential fluence (particles cm^{-2} ion^{-1}) as a function of LET. The fluence measured in the front detector surface can be written:

$$\Phi_{Front} = \Phi_{T_F} + \Phi_{I_B}, \tag{6.1}$$

and the fluence measured in the back detector surface can be written:

$$\Phi_{Back} = \Phi_{T_B} + \Phi_{I_F}. \tag{6.2}$$

The contributions to measured fluence from the target component and the internal component are not known and cannot be determined from a single CR-39 PNTD layer. A separate detector stack, with a CR-39 PNTD target layer added, is needed to estimate the internal component and its contribution to measured fluence.

To measure the CR-39 PNTD internal component, detector stacks without target material placed between the PNTD layers, are exposed to each beam energy used in this work, as shown in Figure 43. For this arrangement where CR-39 layers function as both the target and the detector, T_F and I_B are equivalent to the I_F and T_B components measured in the back detector. Hence, the two detectors necessarily yield the same LET spectrum measurement. Another approach that arrives at the same conclusion is that for CR-39 PNTD, the only charged particles detected are those that pass through the sensitive surface and if two such sensitive surfaces on adjacent CR-39 PNTD layers are positioned at the same depth in a detector stack, they will be exposed to exactly the same radiation field. In this type of detector stack, the population of particles measured can be expressed as:

$$Front = Back \Rightarrow \mathrm{T_F} + \mathrm{I_B} = \mathrm{I_F} + \mathrm{T_B} . \tag{6.3}$$

Expressed in terms of fluence:

$$\Phi'_{Front} = \Phi'_{T_F} + \Phi'_{I_B} , \tag{6.4}$$

and,

$$\Phi'_{Back} = \Phi'_{T_B} + \Phi'_{I_F} , \tag{6.5}$$

where the prime superscript indicates that this measurement was made from an internal component determination detector. Thus:

$$\Phi'_{Front} = \Phi'_{Back} . \tag{6.6}$$

This result provides an important measure of experimental accuracy and also serves as a confirmation of the analysis methods used.

Measurements of the charged particles in classes T_F and T_B for various target materials and beam energies are the quantities of interest. However, for any given experiment the actual measurement result consists of $T_F + I_B$ or $T_B + I_F$, respectively. Thus, the internal component subtraction must be performed for each measurement. An assumption is adopted, that Φ_{I_B} (and Φ_{I_F}) in a detector stack with a target included, is equal to half of the fluence, $\Phi'_{Front} = \Phi'_{T_F} + \Phi'_{I_B}$ measured in a detector stack where CR-39 is both target and detector. This assumption is valid for sufficiently high beam energy due to the small momentum transfer in the first step of the nuclear reaction. In terms of fluence, this assumption can be expressed:

$$\Phi_{T_F} = \Phi_{Front} - \Phi_{I_B} = \Phi_{Front} - \frac{1}{2}\Phi'_{Front}, \tag{6.7}$$

$$\Phi_{T_B} = \Phi_{Back} - \Phi_{I_F} = \Phi_{Back} - \frac{1}{2}\Phi'_{Front}. \tag{6.8}$$

It may be possible to refine this correction for increased accuracy at lower energies by using carefully prepared detectors and additional beam exposures. Through the application of this relationship, the desired fluence correction to account for the internal component of nuclear tracks formed in the CR-39 PNTD itself has been achieved.

6.3. Measurement Limitations

For each of the four track classifications, the depth of nuclear collision and associated charged particle formation inside the detector layer or target layer is unknown. Since charged particles lose energy passing through matter, the particle’s associated LET is changed as a result. In this case, the resulting LET measurement in CR-39 PNTD is higher for an HNR particle formed at some arbitrary depth than the LET measured for the same HNR particle formed at or near the target surface. If a nuclear reaction occurs deep enough in the target layer, the resulting secondaries will completely range out and not leave the target layer. HNR particles formed within the outer 1-10 µm of the target layer have sufficient range to pass into the detector and register as nuclear tracks. The result of this effect is that various HNR particles generated by the same charged particle source, e.g. the reaction $^{27}Al(p,2pn)^{24}Na$ (which is known to have a Maxwellian velocity distribution [Winsberg, 1978, 1980a]), will register a range of nuclear track sizes and lead to a broadened spectrum of LET distributions. This experimental difficulty could possibly be overcome by using very thin layers of target material formed by sputter deposition or other techniques.

There are several additional types of target fragmentation secondary particles that can register as nuclear tracks. It is possible for knock-out protons, neutrons, and α-particles formed in upstream nuclear reactions to undergo nuclear reactions themselves with other nuclei downstream (along the beam direction) resulting in HNR particle formation. To limit this contribution source, the detector stack is as thin as possible.

Since our detector stacks are exposed to the proton beam in air at STP, it is possible for a nuclear reaction to occur in the air in front of the detector stack, resulting in HNR particle formation. Since the detector's sensitive side is facing away from the air upstream, it is unlikely that this HNR particle will have sufficient range to register a track. Also, inside the detector stack, surrounding the target material's edges, there is a small air gap. If a primary particle undergoes a nuclear reaction in this region, it is possible for a HNR to form and register a track in either the front or back detector. Since the detector is marked, showing the location of the target during exposure, and no data is collected outside of this region, this type of reaction can be neglected. Between the target material and detector, when placed in close contact, there still exists a very thin layer of air and perhaps an adsorbed water film. It is possible for a HNR particle to form in this layer and register a track. However, the areal density of this air/water layer is small with respect to the target material, so this type of reaction is neglected.

6.4. Application Methods Overview

In this section, the analysis methods previously presented herein are applied to LET spectrum determination from an experiment performed with a beam of 230 MeV protons on an aluminum target. For this experiment, two detector stacks were exposed, one stack with an aluminum target and another stack with no target material placed between detectors for use as an internal component detector. Following beam exposure, each detector was etched for 2 hours in 6.25 N NaOH maintained at 50° C for the duration of etching. The bulk etch value, *B*, for this etch is 0.5 μm. Following chemical etching, the detectors were allowed to dry in air for at least 24 hr. The detectors were then scanned by AFM (Veeco Instruments, Dimension 3100) using a series of Programmed Move commands with 50 μm × 50 μm scan size and 0.4 Hz scan rate. The AFM data was analyzed for nuclear track physical properties using the algorithms documented in Chapter V.

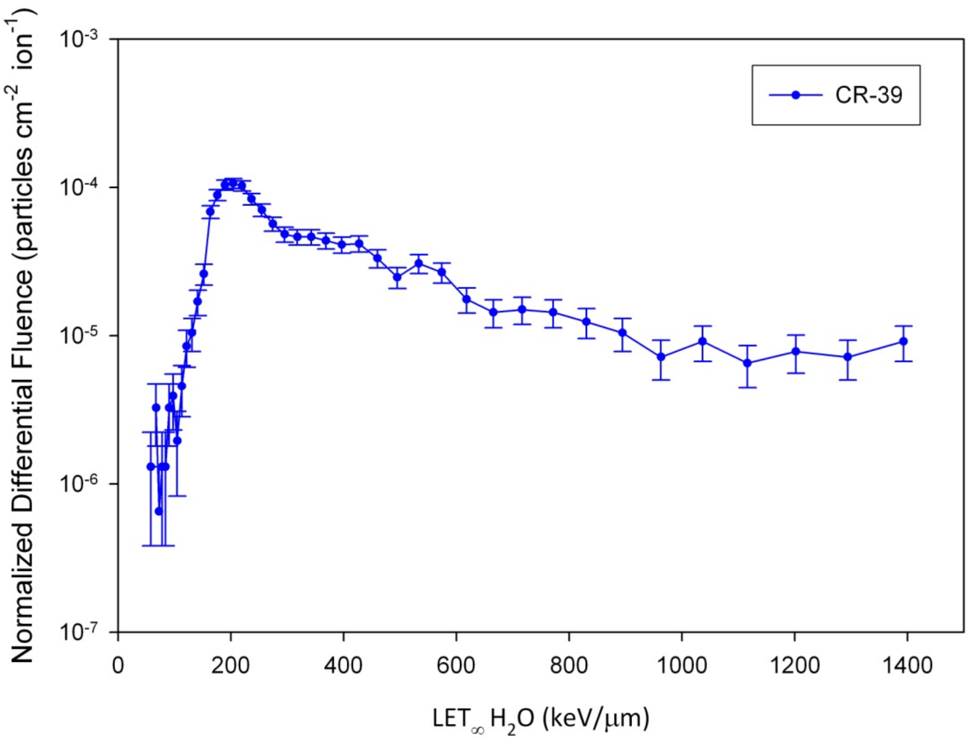

Figure 44. Differential LET fluence spectrum for 230 MeV protons on CR-39 PNTD and normalized to primary proton fluence.

The results of the analysis for the internal component determination detectors are shown in Figure 44. For LET below approximately 220 keV/µm, there is a marked decrease in events recorded. This feature, discussed in Chapter IV, is the result of decreased measurement resolution of the AFM at larger scan sizes (50 µm × 50 µm). Smaller AFM scan sizes and/or increased etching (or alternatively existing OPT methods) could be used to obtain accurate results in the lower LET range. Since tracks produced by short-range, high-LET HNR particles are of primary interest in this work, additional scans to measure the LET spectrum at lower LET were not performed.

For this experiment, the LET of the primary beam protons is 0.4 keV/µm, which is less than the 5 keV/µm LET required for nuclear track registration in CR-39 PNTD.

Therefore, the resulting LET spectrum consists of secondary particles produced in inelastic nuclear collisions, e.g. target fragmentation reactions, with the C and O nuclei present in CR-39 PNTD.

To improve statistics across the LET spectrum, the relation $\Phi'_{Front} = \Phi'_{Back}$ has been applied in obtaining Figure 44, by adding the track analysis results from both front and back detectors together. The individual spectra were observed to have the same qualitative features, prior to this addition, thereby confirming the relation.

The analyses of the front and back detectors with an Al target are shown in Figure 45. The results from Figure 44 are included for comparison. While all three curves have the same basic appearance, there are subtle differences that arise from the introduction of the Al target layer. The Al nuclei present in the target layer have a greater cross section for inelastic nuclear collisions, than do the C and O nuclei in CR-39 PNTD, increasing the number of secondary particles detected. In addition, the Al nuclei extend the range HNR particle Z. In Figure 46, the results are shown after subtracting the internal component as determined from the CR-39 target shown in Figure 44.

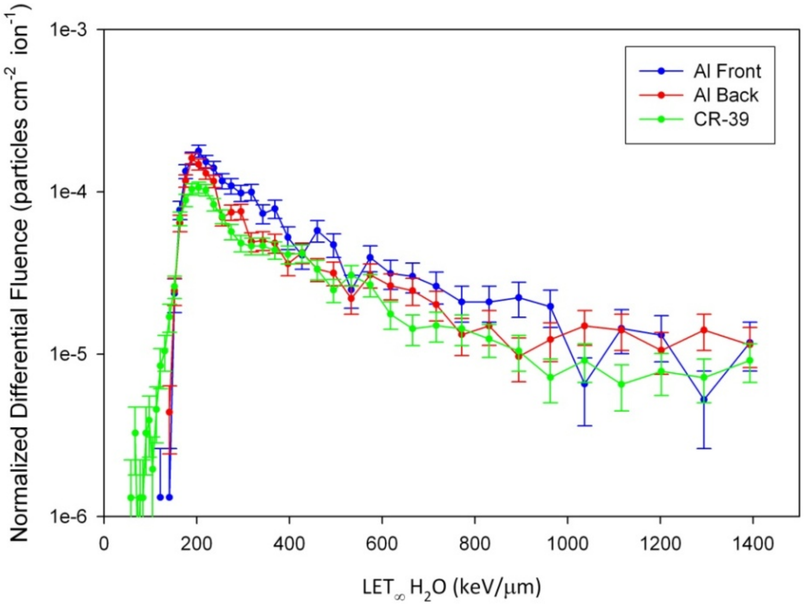

Figure 45. Results of analysis for 230 MeV proton on Al, front and back detectors. The result obtained with CR-39 as target is shown for comparison.

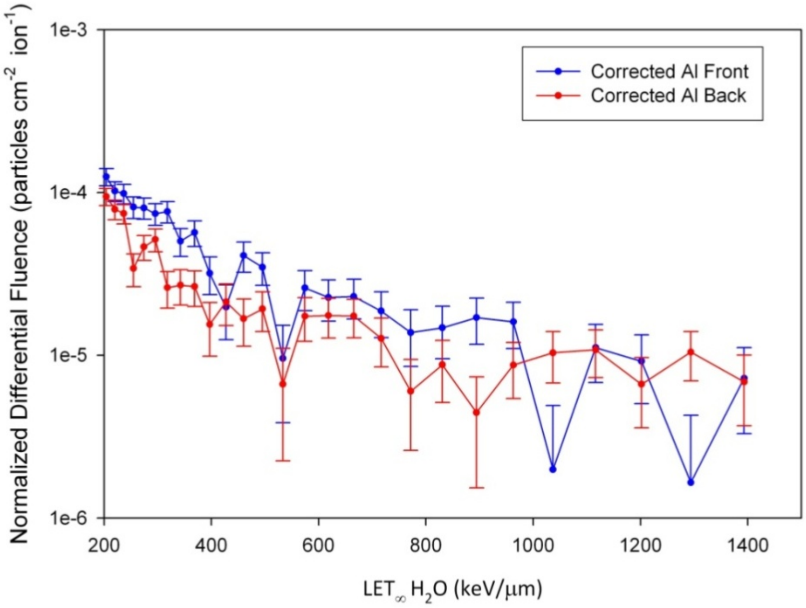

Figure 46. Final analysis results, with front and back spectra after correction for the internal component, for 230 MeV proton on an Al target.

The data in Figure 46 represent the short-range, high LET charged particles produced by target fragmentation reactions between primary beam protons and the Al nuclei in the target layer. The possible HNR particles produced in these reactions include (but are not limited to) the nuclei ^{24}Na, ^{22}Na, ^{18}F, ^{11}C, ^{8}Li, and ^{7}Be. The Na and F reactions are not possible in CR-39 as a target.

In Figure 46, the differential fluence measured in the front detector lies above that measured in the back detector over most of the measured LET spectrum. This feature is expected due to the forward peaked velocity distribution for knock-out particles and IMFs. At approximately 1000 keV/μm, the front and back spectra begin to coincide. At higher LET values the statistics are noticeably worse due to low numbers of events measured. Further experiments are required to improve statistics in this highest LET region.

6.5. Additional Experimental Results

The study of proton-induced HNR particle formation included detectors exposed to 60, 230, and 1000 MeV proton beams. For each of the proton beams, exposures were made with CR-39 PNTD target layers for internal component determination and with Al and Cu target layers. The results from these experiments are presented and discussed in this section.

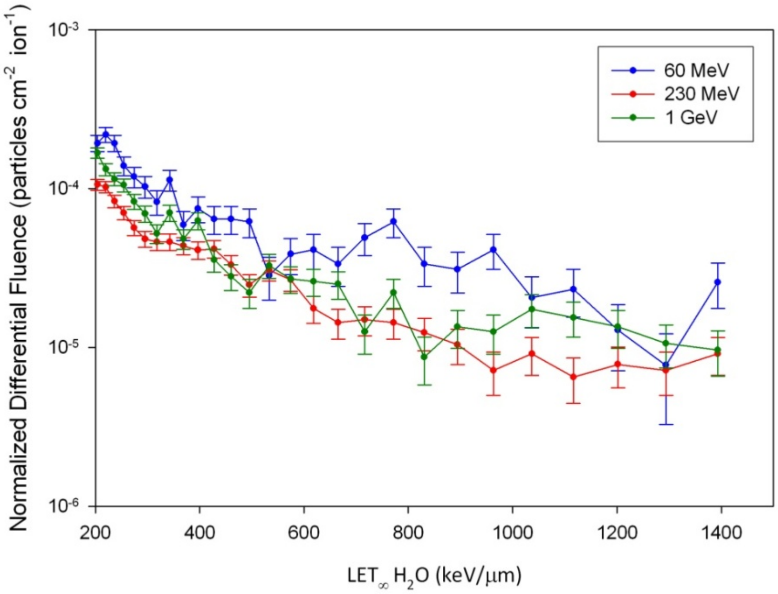

Figure 47. Comparison of results obtained from 3 proton beam energies on CR-39 PNTD targets.

6.5.1. Internal Component Determination Detector Analysis

The LET spectra in CR-39 PNTD (CR-39 target and detector), for the three proton beam energies used in this research are shown in Figure 47. In these spectra, the products of inelastic nuclear collisions between beam protons and the nuclei C and O are the primary contributors to the data. The internal component determination detectors were also used for the purpose of absorbed dose calculation since they contain information regarding C and O target fragmentation reactions, which are most relevant in tissue.

The data in Figure 47 is consistent with the inelastic nuclear reaction cross-section measurements for ^{12}C and ^{16}O previously published by other investigators [Renberg et al., 1972; Carlson et al., 1975; Schwaller et al., 1979; Janni, 1982; Paganetti, 2002], in as much as the fluences measured in our detectors scale with cross section measured by these other investigators. The inelastic nuclear interaction cross sections for 60, 230, and

1000 MeV protons on C, O, Al, and Cu target nuclei are summarized in Table 6.2. The inelastic nuclear cross sections are plotted with respect to energy Figure 48.

Table 6.2. Inelastic nuclear cross sections (in mb) for selected nuclei obtained by interpolation from Janni [Janni, 1982].

Target / Energy	C	O	Al	Cu
60 MeV	336 mb	402 mb	562 mb	965 mb
230 MeV	204 mb	233 mb	385 mb	706 mb
1 Gev	240 mb	268 mb	438 mb	778 mb

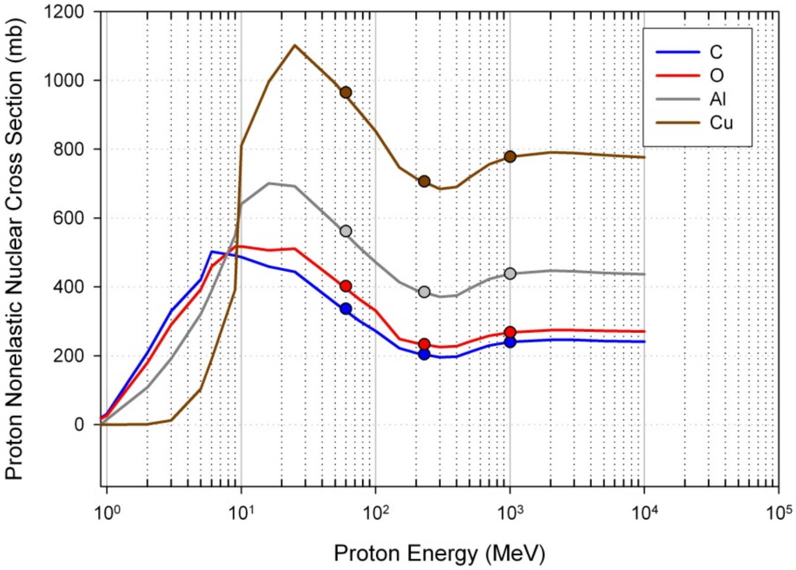

Figure 48. Summary of non-elastic nuclear reaction cross sections, in millibarns (mb), for C, O, Al, and Cu [Janni, 1982]. The cross section values are annotated with circles in the figure at the specific energy values of 60, 230, and 1000 MeV.

It is useful to divide the LET spectra in Figure 47 into two regions: LET ≲ 600 keV/µm, and LET ≳ 600 keV/µm. In the LET range below 600 keV/µm, the dominant fraction of tracks are expected to be light charged particles (LCPs), with $Z < 2$, and IMFs with $3 \leq Z \lesssim 10$. These secondary particles are ejected during the first step of the two-step nuclear collision process. A characteristic of this region is the gradual reduction in fluence, by approximately an order of magnitude, with increasing LET.

In the LET range above 600 keV/µm, HNR particles formed in the second step of the nuclear collision process are expected dominate. The primary characteristic of the high LET region is that the fluence remains relatively uniform with increasing LET, reflecting a variety of HNR particles with varied velocity, range, and depth of formation in the target layer. It is understood that there is a degree of overlap between the high and low LET ranges and that more detailed experiments are required to impose a clear distinction between IMFs and HNR particles.

The results of Figure 47 were used in the following sections to correct for internal components of fluence, as well as for total dose calculations for the short-range, high LET particle contribution to dose.

6.5.2. 60 MeV Proton Results with Al and Cu Targets

An experiment was performed with the 60 MeV proton beam (LLUMC) using an Al target foil placed between CR-39 PNTD detector layers. Figure 49 shows the differential LET fluence spectra measured in the front and back detectors, and normalized to primary proton fluence. Increased secondary particle fluence seen in the forward detector relative to the back detector is consistent with expectations for this energy. For 60 MeV proton exposures, we expect a large fractional momentum transfer in the first step of the nuclear collision, which results in a final HNR particle distribution that is peaked forward in the laboratory frame of reference relative to the primary proton beam.

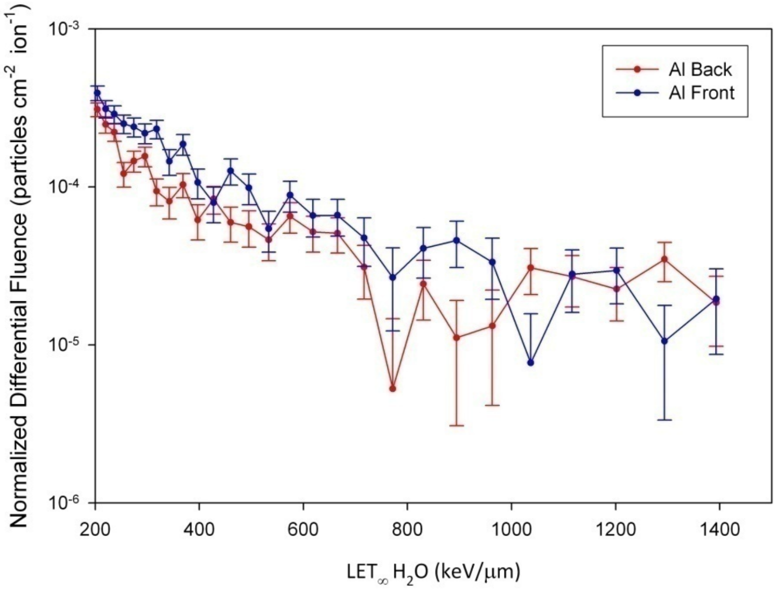

Figure 49. Analysis results for 60 MeV protons on an Al target, front and back detectors after internal component correction.

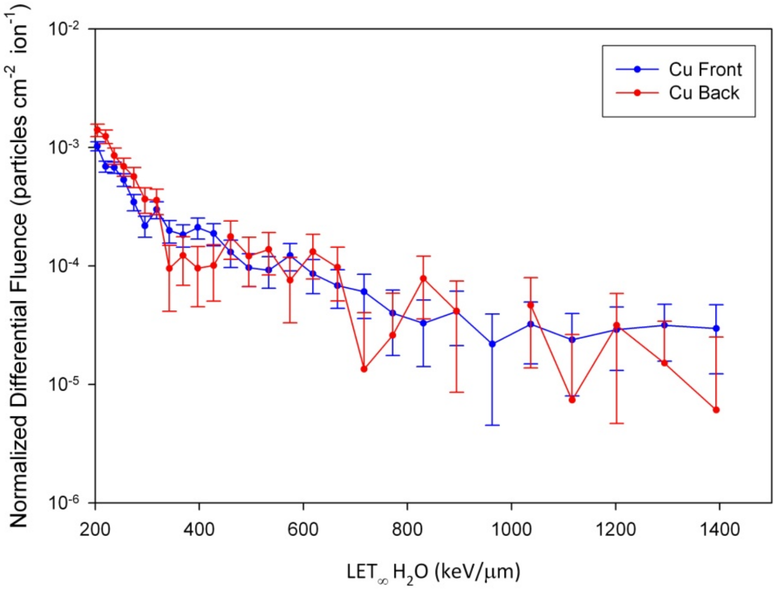

Figure 50. Analysis results for 60 MeV protons on a Cu target, front and back detectors after internal component correction.

A similar experiment was performed using a Cu target foil, shown in Figure 50. For the Cu target, there is no forward velocity peak observed. This is likely due to poor AFM scan quality affecting the statistical significance of the analysis in the back detector. More AFM data would be needed to complete the analysis of the Cu target for this proton energy.

A comparison of LET spectra measured in the 60 MeV proton beam for CR-39, Al, and Cu targets is shown in Figure 51. The results of this comparison are consistent with the non-elastic nuclear cross sections shown in Figure 48 [Janni, 1982], in which the Cu nucleus has the greatest nuclear reaction cross section (965 mb), followed by Al (562 mb) and then the C (336 mb) and O (402 mb) nuclei in the CR-39 PNTD.

In Figure 51, in the high LET region, particularly above 800 keV/µm, there does not appear to be a clear relationship between target Z and the measured HNR particle fluences. This is likely due to poor statistics for such high LET events. The additional HNR particle Z values present as target Z increases have ranges that decrease rapidly with HNR particle Z. It has been shown in the case of ^{27}Al target material that ^{7}Be HNR particles have a range of approximately 4.6 µm adjusted for the density of CR-39, while ^{24}Na HNR particles have a range of 0.37 µm [Winsberg et al., 1980]. More AFM data is needed to improve the statistics for LET values above 800 keV/µm.

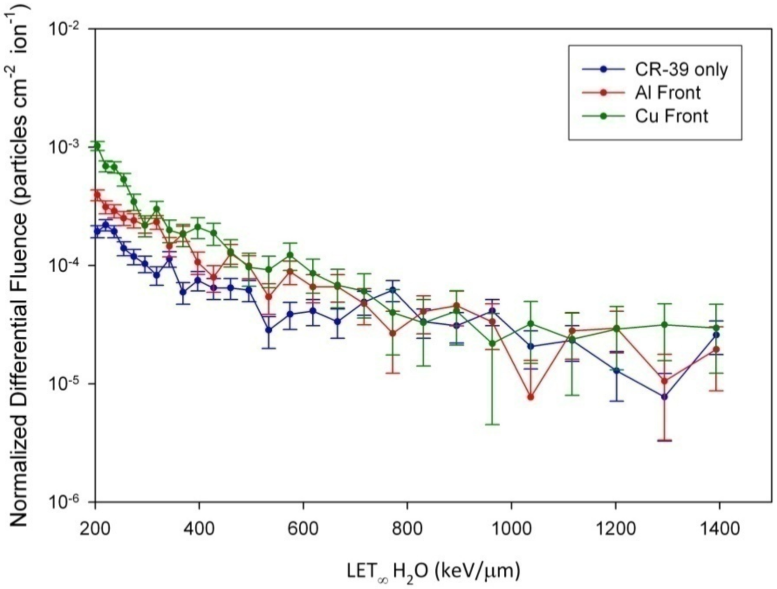

Figure 51. Comparison between CR-39, Al, and Cu target analysis results for 60 MeV proton beam exposures performed at LLUMC. The data is from front detectors only.

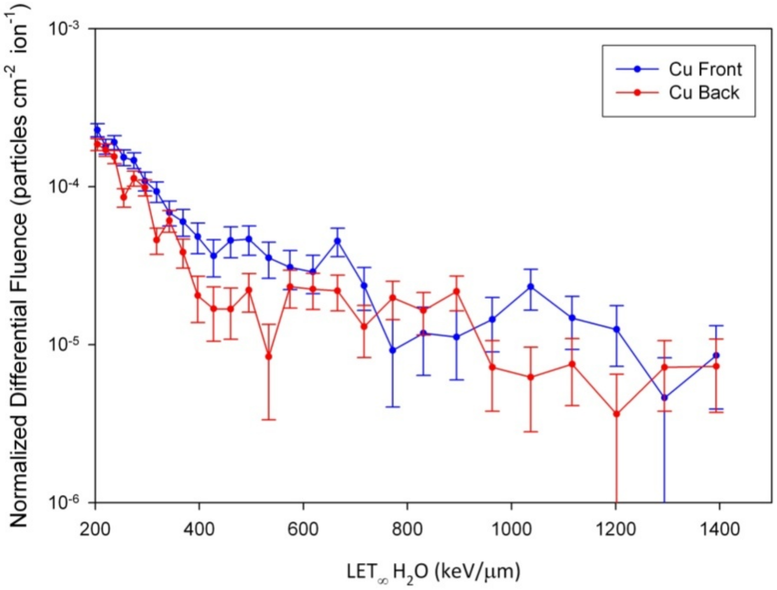

Figure 52. Analysis results for a 230 MeV proton beam on a Cu target.

6.5.3. 230 MeV Proton Results with Al and Cu Targets

The results of an experiment performed with the 230 MeV proton beam (LLUMC) using an Al target foil placed between CR-39 PNTD detector layers are shown in Figure 46. Figure 52 shows similar results for a 230 MeV proton beam on a Cu target. For 230 MeV protons on Cu, an increase in fluence is observed in the forward direction, i.e. in the front detector, which is likely due to additional forward travelling knock-out particles. At high LET, the data suffer from poor statistics, as in the other reported spectra.

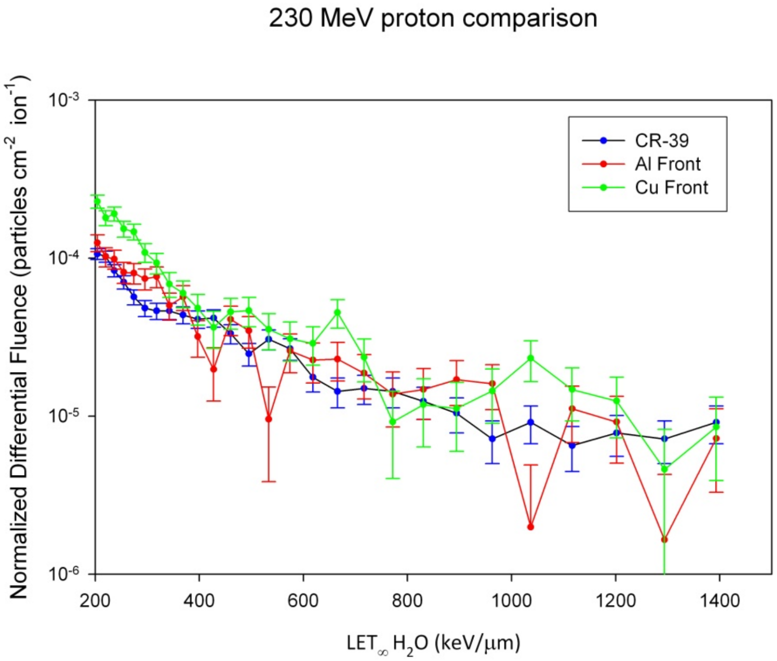

Figure 53. Comparison between Al, Cu, and CR-39 target analysis results for 230 MeV proton beam exposures performed at LLUMC.

A comparison of experimental results for CR-39 PNTD, Al, and Cu targets exposed to 230 MeV protons is shown in Figure 53. The data are qualitatively consistent with the nuclear inelastic cross sections as shown in Figure 48, except for the spectrum for Al measured in the forward direction, which appears lower than expected. The cause for this is not known and more data, i.e. additional AFM scans and/or additional beam exposures, are needed to clarify this region of the LET spectrum.

6.5.4. 1 GeV Protons on CR-39, Al, and Cu Targets

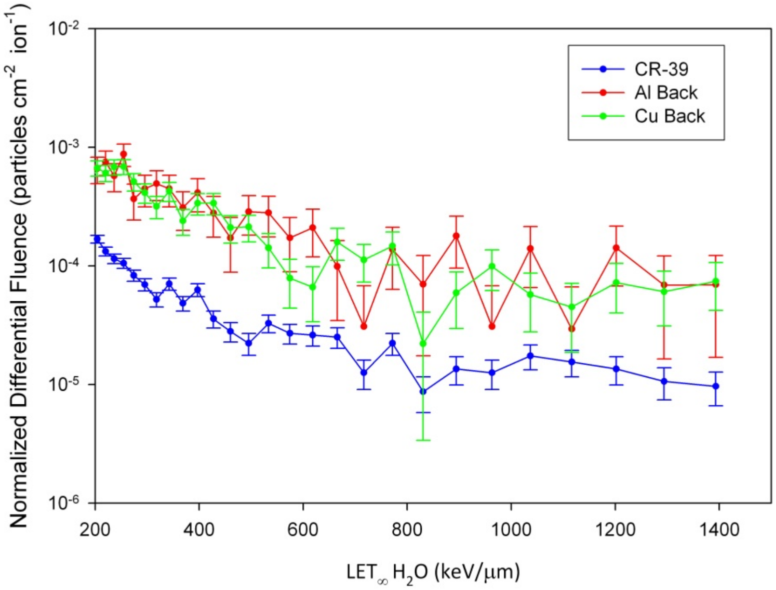

Figure 54. Comparison between CR-39, Al, and Cu target results for 1 GeV proton beam exposures performed at BNL NSRL.

An experiment was performed at the NASA Space Radiation Laboratory (NSRL) at BNL, in which CR-39, Al, and Cu target materials were exposed to beams of 1 GeV protons. The results for this set of experiments are shown in Figure 54. In this plot, the Al and Cu data were obtained from a smaller number of AFM scans than the number used in the 60 and 230 MeV analyses, resulting in a reduction in statistical significance. It has been observed that the LET spectrum fluence values tend to decrease as additional AFM scans are added to the analysis. This is expected since the area term in the fluence calculation is in the denominator and, as the denominator grows, the resulting fluence is reduced until the number of events of a particular LET prevent further reduction. The Al and Cu spectra in this plot are of the appropriate shape, but are likely too high by approximately a factor of 5.

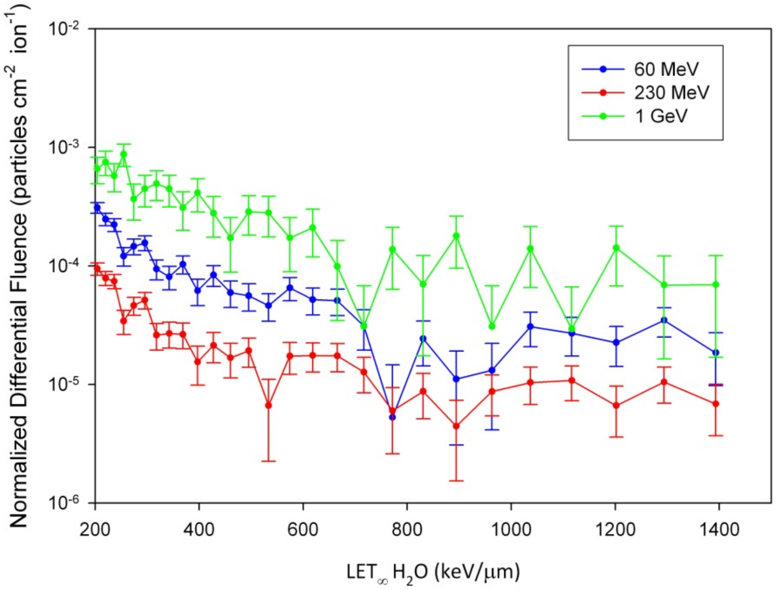

Figure 55. Comparison of proton beam exposures at 60, 230 and 1000 MeV with an Al target.

6.5.5. Comparison of Results from Three Proton Energies

The results of the experiments on Al and Cu targets are shown together as a function of primary proton energy. The Al data are compared in Figure 55 and the Cu data are compared in Figure 56. In each of the plots, the data for the 1 GeV beam exposure is affected by poor statistics as mentioned above. The comparisons between 60 and 230 MeV proton exposures, for both Al and Cu targets, are consistent with expectations based on nuclear cross section data listed in Table 6.2 and shown in Figure 48.

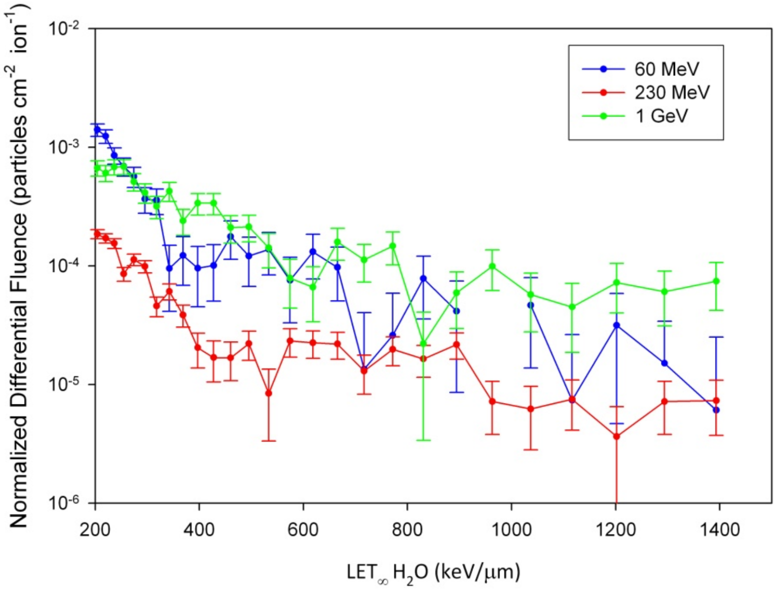

Figure 56. Comparison of proton beam exposures for 60, 230 and 1000 MeV beams with Cu targets.

6.5.6. Dose Calculations

Using the LET spectra measured with AFM, the absorbed dose was calculated for CR-39, Al, and Cu targets using equation (3.20). The doses calculated are listed in Table 2 with units of Gy·ion^{-1}. The dose calculation includes LET > 200 keV/μm, therefore it represents the dose from intermediate mass fragments as well as HNR particles. These dose measurements and their implication for proton radiotherapy are difficult to interpret due to the nature of short-range, high-LET particle stopping in tissue. It is not clear what the biological impact of the particles in question might be without further experiments.

Table 6.3. Dose measurements for three proton energies on CR-39, Al, and Cu targets. The units are Gy·ion^{-1}. For entries with two listed values: the top value is from the front detector and the bottom value is from the back.

Target Proton Energy	CR-39 (C and O)	Al	Cu
60 MeV	$6.6 \pm 1.0 \times 10^{-10}$	$1.4 \pm 0.2 \times 10^{-8}$ $9.2 \pm 2.8 \times 10^{-9}$	$5.5 \pm 0.9 \times 10^{-9}$ $5.8 \pm 1.4 \times 10^{-9}$
230 MeV	$7.3 \pm 1.2 \times 10^{-10}$	$1.1 \pm 0.2 \times 10^{-9}$ $8.4 \pm 1.3 \times 10^{-10}$	$1.4 \pm 0.2 \times 10^{-9}$ $1.1 \pm 0.2 \times 10^{-9}$
1000 MeV	$8.8 \pm 1.4 \times 10^{-10}$	$6.0 \pm 2.3 \times 10^{-9}$	$5.2 \pm 1.2 \times 10^{-9}$

6.5.7. Results of Angle Detector Exposures

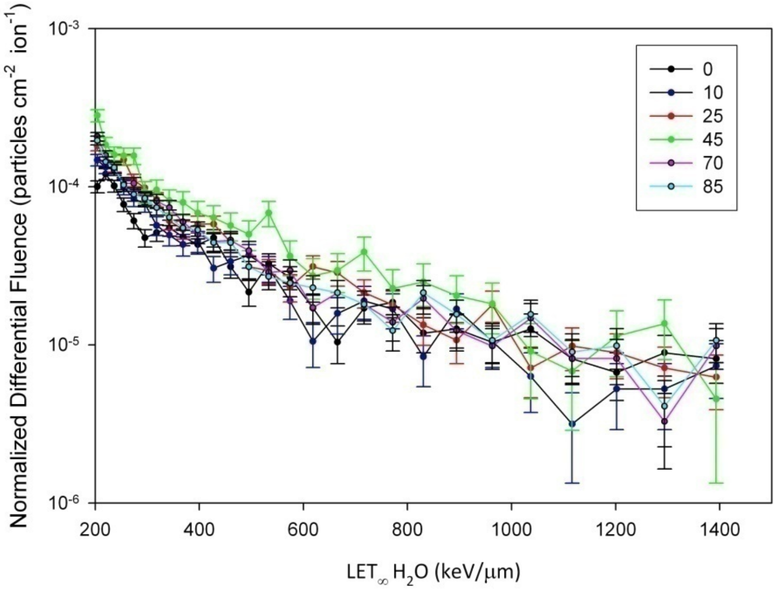

Figure 57. CR-39 PNTD was exposed to a 230 MeV proton beam at LLUMC, with the angle of beam incidence varied. The analysis results are consistent with an isotropic distribution of HNR particles.

Because HNR particles are the result of the evaporation process in the second step of the Serber two-step model, the distribution of HNR particles is expected to be isotropic with respect to direction. A set of experiments were conducted using the 230 MeV proton beam at LLUMC to test the validity of the isotropy assumption. For this set of experiments, a detector stand consisting of a retaining clip, vertical post, and a circular base with degree increment markings was used. The spectra shown in Figure 57 include data from both front and back detectors for improved statistics. The results from the angled detectors are generally consistent with the features expected for an isotropic source of HNR particles produced in reactions with C and O nuclei in CR-39 PNTD. A deviation from isotropy, were it to exist would be on the order of experimental error, e.g. < 20%.

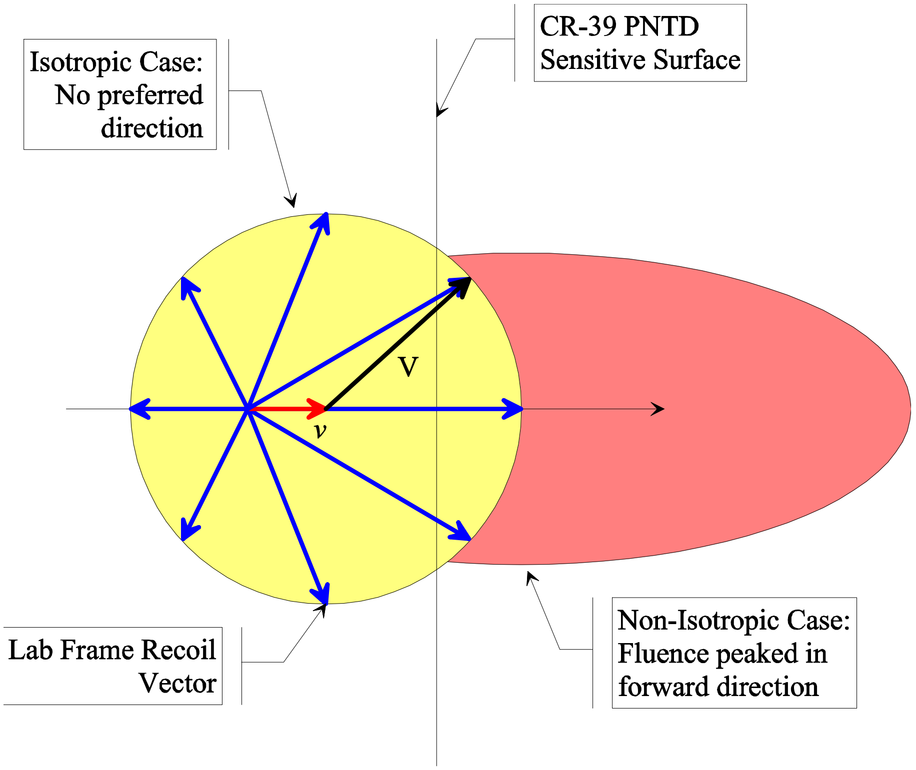

Figure 58. A non-isotropic HNR particle formation mechanism, in red, compared to an isotropic formation mechanism, shown in yellow. The blue vectors represent the vector sum of velocity components imparted in the first and second steps of the collision.

In Figure 58, the case for an isotropic HNR particle production mechanism is compared to a hypothetical production mechanism that is peaked in the forward direction. Note that for a forward preference in HNR particle formation, an increased fluence, as measured in the front and back detectors with a normally incident proton beam (0 degrees) would be expected. The increased fluence for a preferred emission direction could be peaked in a small range of LET or across the LET spectrum if the directional preference had no energy dependence. Our preliminary data indicate that for 230 MeV proton-induced nuclear reactions, the HNR particle formation mechanism is isotropic for HNR particle Z less than 8. Figure 59 shows a comparison between normalized integral fluence for LET > 200 keV/μm obtained for various angles of incidence, the data are consistent with isotropy.

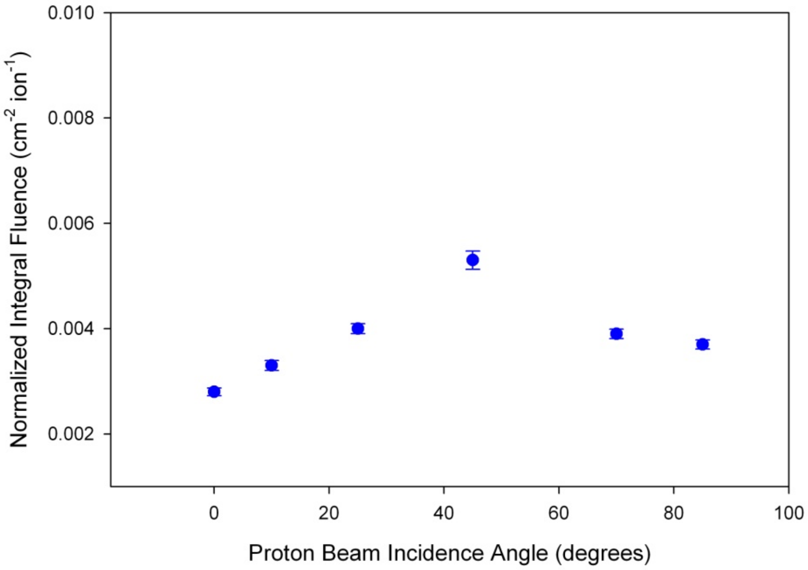

Figure 59. Normalized integral fluence for LET > 200 keV/μm obtained from 230 MeV protons on CR-39 PNTD with varied angle of incidence relative to the detector surface.

6.5.8. Discussion of Measurements

Referring again to the data from 230 MeV proton exposed detectors, an attempt was made to build a composite LET spectrum using individual LET spectra obtained from detectors processed with bulk etch values of 0.5 and 1.0 μm. In Figure 60, the blue curve is identical to the previous result, while the red curve was obtained from the analysis of the detector processed with a 1.0 μm etch. The data in the 1.0 μm bulk etch analysis were analyzed using the same calibration function as that obtained for 0.5 μm. The relationship between the two spectra reveals two important results: 1) a multiple etch analysis method, if properly calibrated, could be used to obtain a full spectrum analysis using identical scan sizes, and 2) the longer 1.0 μm etch is sufficient to remove a significant population of short-range, high LET tracks, which is evident from the poor high LET particle statistics in the detector processed with 1.0 μm etching.

In the thin-target/thin-catcher experiments conducted by previous investigators, notably [Winsberg, 1980a], it was possible to determine the parameters of the individual nuclear reactions that take place in a target layer by careful examination of the front and back catcher foils. Unfortunately, this analysis is not possible with our present methods. It is possible to convert the fluence measurements obtained in this work to a total number of events measured in the forward and backward directions, and this would directly relate to the activity measurements in catcher foil counting, but since all of the various possible HNR particles are measured, and no means of identifying their individual charges exists, it is not possible to make calculations specific to a particular reaction process.

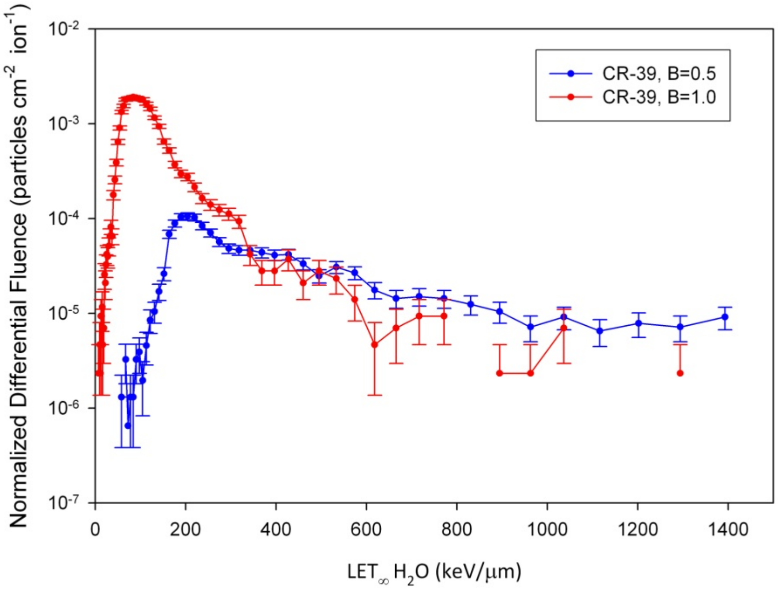

Figure 60. This plot compares the analysis results from CR-39 PNTD exposed to 230 MeV protons at LLUMC for varied amounts of etch. The vertical shift in fluence for the 1 μm etch indicates that a separate calibration would be required for a change in etch.

It would be an interesting extension of both AFM/CR-39 PNTD and radiochemical methods to make a coordinated comparison, e.g. conduct an experiment using the present method and also using gamma spectroscopy methods for activity determinations using the same detectors. The AFM/CR-39 PNTD method would provide detailed measurements of nuclear tracks while the radiochemical method would provide isotope identification. A comparison between the two measurement methods could be used to determine the relative contributions from each type of HNR particle. This approach would be complicated by the high doses required in activation studies with thin targets, although with sensitive active detectors used in the counting facility it may be feasible.

CHAPTER VII

EXTERNAL SPACECRAFT MEASUREMENTS

As described in the previous chapter, the analysis methods for AFM track data from CR-39 PNTD were tested in a number of accelerator-based HNR particle experiments. In addition to the proton accelerator experiments performed for this work, two detectors exposed to high fluences on the exterior of spacecraft in low Earth orbit (LEO) were analyzed with AFM. In the first space exposure, a CR-39 PNTD was exposed on the outer surface of the Mir Space Station for 130 days and returned to Earth in 1997 [Benton et al., 2002a]. AFM analysis was also applied to CR-39 PNTD exposed as part of the Matroshka experiment on the exterior of the International Space Station (ISS) for 539 days and returned to Earth in 2005 [Reitz et al., 2009].

The radiation environment in the 400 km altitude, 51.6° inclination orbit of the Mir Space Station and ISS is dominated by the proton component of the GCR spectrum [Simpson, 1983], with additional proton contributions from Earth's trapped radiation belts and solar particle events [NCRP, 1989]. The trapped proton flux is at its maximum in a region known as the South Atlantic Anomaly (SAA) [NCRP, 1989]. Based on recent measurements in LEO [Badhwar et al., 1995; Alcaraz et al., 2000; Badhwar, 2002; Benton et al., 2006], it is expected that the majority of the protons that register tracks in

CR-39 PNTD will have energy $\lesssim$ 20 MeV. Protons with such low energy typically stop in $\lesssim$ 0.1 g/cm^2 of material. Due to the long duration exposure, especially in the case for the external Matroshka detectors, very high proton fluences are expected. Analysis of detectors with OPT methods is difficult for fluences > 10^5 cm^{-2}, therefore the AFM must be used to complete the analysis.

7.0 MIR Least Shielded External Analysis

The least shielded layer of CR-39 PNTD exposed on Mir was mounted externally on the Kvant 2 module under 0.005 g/cm^2 aluminized Kapton foil for protection during handling and to maintain an oxygen environment around the detector. Following return to Earth, the PNTD was etched in 6.25 N NaOH at 50º C. The bulk etch value measured for this detector was 0.84 μm as determined by the 'step method' [Yasuda et al., 1998; Benton et al., 2002a].

The first analysis of this detector was performed by Benton using AFM, in the first application of AFM methods for CR-39 PNTD exposed in space [Benton et al., 2002a]. In this analysis Benton, acquired the AFM scans manually and analyzed the track data by means of the section analysis tools provided by the AFM manufacturer. To test the AFM analysis methods developed as part of the current work, this same detector was reanalyzed.

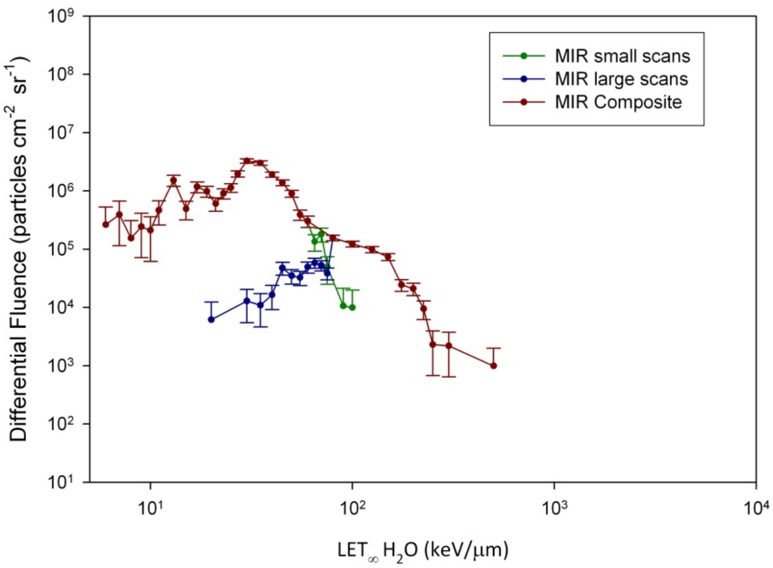

Figure 61. Differential LET fluence spectra measured in CR-39 PNTD exposed under 0.005 g/cm^2 shielding on the exterior of the Mir Space Station. Analysis of the detector was completed using a combination of small area (5 µm × 5 µm) AFM scans and large area (90 µm × 90 µm) scans to ensure adequate sampling of low and high LET components.

Since the space environment contains energetic protons and heavy ions from various sources, an analysis of the complete LET spectrum from 5 to 1500 keV/µm was measured. In order to properly analyze the complete LET spectrum, a combination of different AFM scan sizes was used to form a composite LET spectrum for this detector. Small scan sizes (5 µm × 5 µm) were included to accurately sample low LET tracks and large area (90 µm × 90 µm) scans were used to attain sufficient statistics for high LET tracks, which were far less common. In analysis of each sized scan frame, the area scanned was independently recorded to properly determine fluence information. The two resulting spectra were then merged by selecting the points with greatest statistical significance from each curve. The composite spectrum from the reanalysis of the externally exposed PNTD from Mir is shown (in red) in Figure 61.

The LET spectrum measured on the exterior of the Mir Space Station is dominated by particles of LET < 100 keV/μm. These are primarily low energy protons encountered during passage of the Mir Space Station through the SAA.

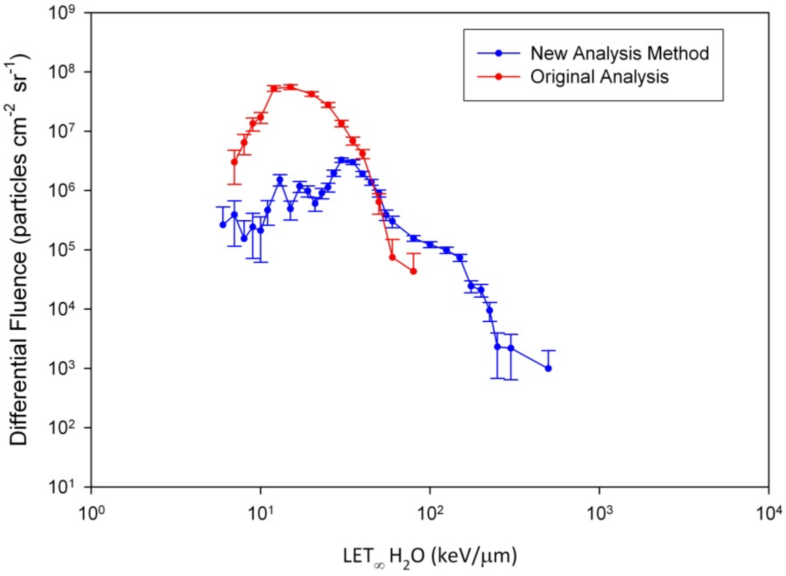

Figure 62. Comparison between differential fluence spectrum obtained in the original analysis and that obtained using new methods.

A comparison of the LET spectrum obtained using the AFM analysis tools developed in this work with the original LET spectrum measurement obtained using the section analysis tool is shown in Figure 62. The major difference between the spectra is the reduced peak value in fluence obtained with the new methods, largely due to the greater resolution and lack of subjective bias in the new methods compared to the section analysis tool. Additionally, the LET spectrum obtained with the new methods has more information in the high LET region above 100 keV/ μm. This is due to the acquisition of

AFM data over a much larger scan area which obtains greatly improved statistics on comparatively rare, high-LET tracks.

7.1. Matroshka Least Shielded External Detector

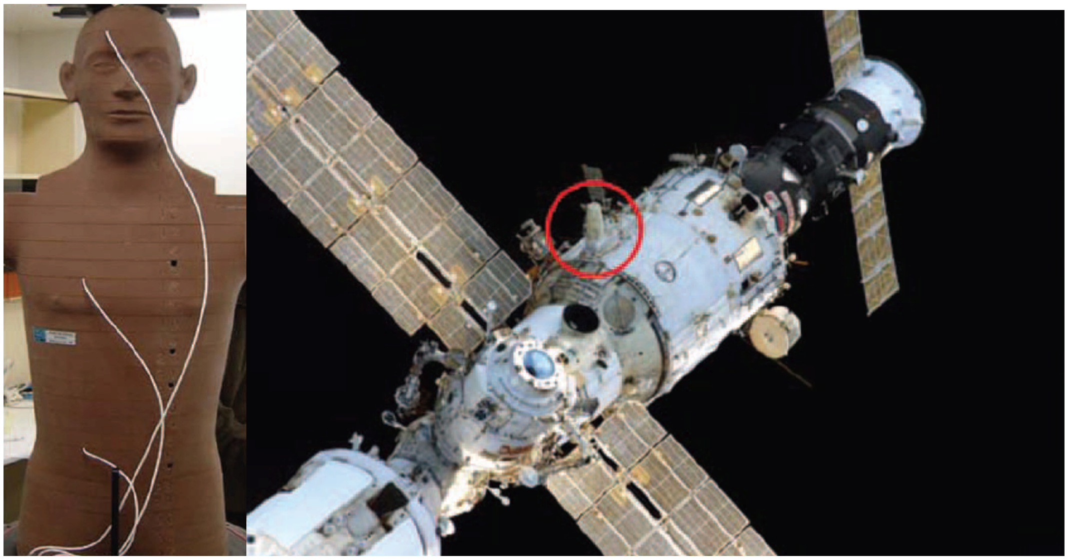

Figure 63. The Matroshka experiment consisted of multiple detectors of various types situated in a human phantom which was installed on the ISS exterior during exposure.

The Matroshka experiment consisted of a tissue equivalent phantom torso and head exposed within a sealed container simulating an EVA suit exposed on the exterior of the ISS as shown in Figure 63. Passive radiation detectors were exposed on the outside of the Matroshka container and this included a layer of CR-39 PNTD exposed under 0.005 g/cm^2 of aluminized Kapton foil.

The analysis of the CR-39 PNTD layer exposed with the Matroshka experiment was similar to that for the externally exposed PNTD on Mir with the exception that a mid-range AFM scan size (50 μm × 50 μm) was also used. The differential LET fluence spectra obtained from 5 µm × 5 µm, 50 µm × 50 µm, and 90 µm × 90 µm AFM scans are shown in Figure 64.

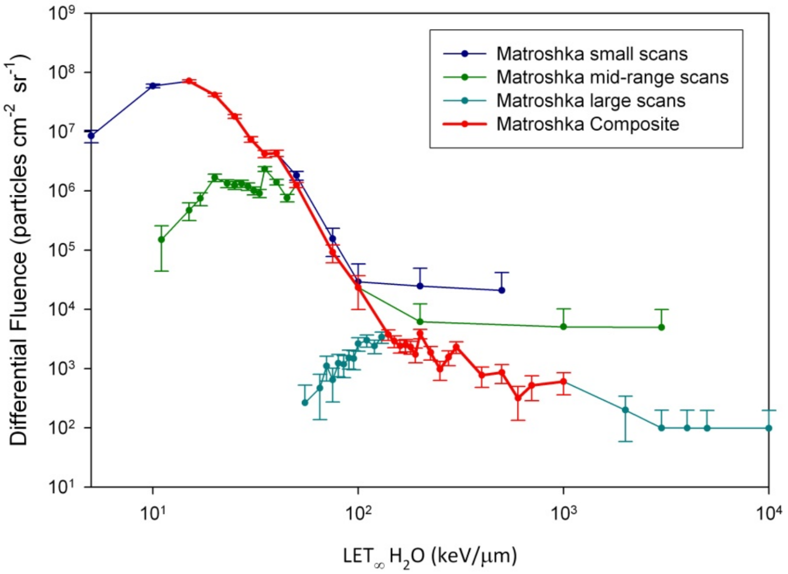

Figure 64. Analysis of the Matroshka least shielded external detector was completed using three separate scan regimes. This is discussed in the text.

The composite spectrum obtained from combining the LET spectrum measurements obtained from the three different scan sizes is shown (in red) in Figure 64. The differential LET fluence spectrum obtained from the Matroshka detector displays a drop in fluence of almost four orders of magnitude in the range between 10 and 100 keV/µm. This LET region is dominated by low energy protons, primarily encountered in the SAA, that are attenuated in the first 0.1 g/cm^2 of shielding. The high LET component of the spectrum consists of primary heavy ions ($Z \geq 3$) in the GCR.

7.2. Comparison of External LET Spectrum Measurements for Mir and ISS

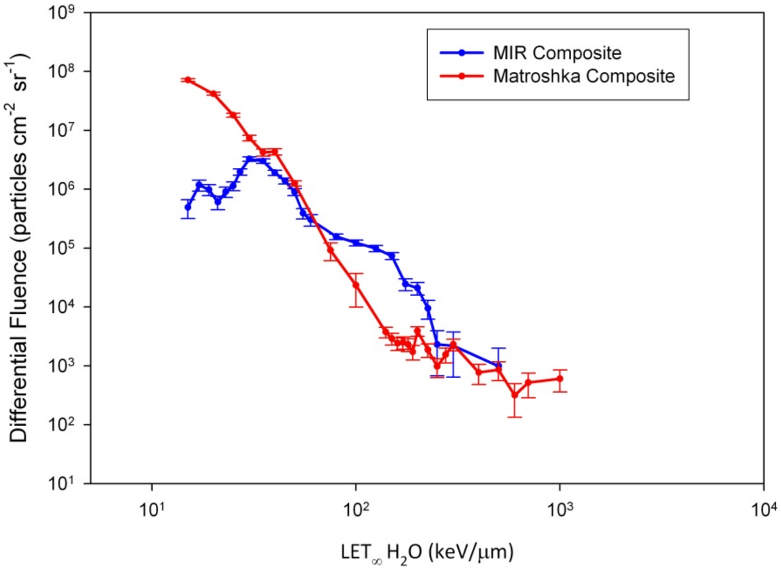

Figure 65. Differential LET fluence spectra measured in CR-39 PNTD exposed on the exterior of the Mir Space Station and ISS and analyzed using the newly developed AFM analysis methods.

In Figure 65, the LET spectra from the outside of Mir and ISS are plotted together for comparison. The detectors from the two experiments were exposed under different localized shielding and under different environmental conditions, accounting for the differences between the two curves. The differences in exposure environments include spacecraft orientation, external experiment placement, mounting hardware, and the difference in phase of the solar cycle. For both space experiments, an analysis of the detector would not be possible using OPT methods due to the high fluence of protons encountered during the exposures. OPT methods are limited to fluences $\lesssim 10^5$, above which track overlap becomes a limiting factor.

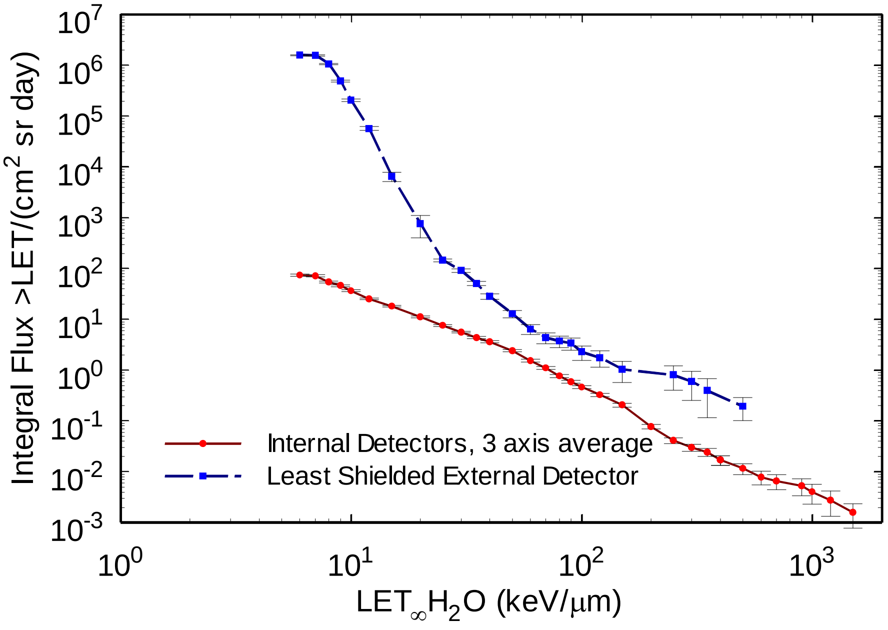

Figure 66. Differential LET fluence spectra measured in CR-39 PNTD exposed on the exterior of the ISS and analyzed by AFM and in CR-39 PNTD exposed on the interior of the ISS and analyzed by OPT methods.

Figure 66 compares the differential LET fluence spectrum measured on the exterior of the ISS with a spectrum measured in CR-39 PNTD exposed on the interior of the ISS during the same period. The internal LET spectrum was obtained by OPT analysis of the CR-39 PNTD. The principle difference between the two spectra is the presence of low energy proton tracks with LET < 100 keV/μm in the externally exposed detector. These low energy protons are attenuated before they have a chance to reach the internally exposed PNTD.

CHAPTER VIII

CONCLUSIONS AND FUTURE WORK

The methods presented in this paper for the analysis of CR-39 PNTD with AFM using topographic analysis have been applied to numerous accelerator-based experiments and to experiments with detectors exposed in space. The experimental applications have successfully demonstrated the capability of resolving nuclear track features of short-range, high-LET charged particles. However, the preliminary nature of these results must be stressed. It is only with the completion of a quantitative AFM analysis methodology that we can now begin a rigorous investigation of HNR particles and their contribution to total dose in proton radiotherapy patients and astronauts. In this Chapter, the conclusions reached as a result of this investigation will be discussed, as well as the possibilities for future work, both to further improve the AFM data analysis methods and for applications of these methods in research.

8.0 AFM Enables Use of Short Etch

An important feature of this work is the implementation of a short duration chemical etch to achieve a bulk etch of 0.5 μm. This bulk etch value has been demonstrated to preserve short-range high LET tracks for analysis. Our analysis indicates that additional etching, up to 1.0 μm, is sufficient to remove many nuclear tracks of interest in this work. This finding is consistent with recoil range data presented by various investigators, which show that many HNR particles have ranges less than 1.0 μm. With respect to CR-39 PNTD, it has been shown that the bulk etch value has an intrinsic effect on the analysis result attainable for any given exposure. The technical merits of reduced chemical etching have been previously established [Benton et al., 2000; Benton et al., 2002a, 2002c]. The work reported here provides a quantitative assessment of the benefit of reduced etching in a few selected circumstances.

8.1. Importance of Scan Automation

With respect to AFM operation during scanning, it has been demonstrated that scan automation, e.g. the implementation of a properly designed Programmed Move or Auto Scan, is an essential analytical practice. Automated scanning enables the acquisition of multiple AFM scans without overlapping successive scans. Manual scanning, e.g. each scan is started individually, may be used provided the microscopist maintains a record of each position scanned and selects a previously un-scanned area for successive scans. Scan automation enables unattended operation of the AFM for protracted scanning sessions that, taken together, total in several days of AFM scanning for each detector. A large quantity of AFM data is required to collect sufficient statistics on the comparatively rare short-range, high LET charged particle tracks. Experiment parameters can be adjusted to a certain degree to increase the number of HNR particles by increasing the primary beam dose delivered, but high beam doses are not always practical due to accelerator limitations. The experimentalist must operate within the restrictions of the beam delivery system, which often requires the acceptance of relatively low beam doses.

8.2. Use of Semi-Automated Analysis

Regarding the analysis of AFM data, image processing based methods, existing Veeco software, and manual topographic analysis were each evaluated extensively for adaptation into a robust AFM/CR-39 PNTD analysis system. The semi-automated analysis method presented here enables rapid analysis of AFM data while maintaining a high degree of accuracy, both attributes that were lacking in previously existing methods. Application of ellipse specific, least squares ellipse fitting, followed by the estimation of the goodness of fit has been demonstrated to be a powerful tool, both for analysis of nuclear tracks and for the separation of conjoined tracks, as well as for the rejection of non-track features.

It is clear that established OPT analysis methods are suitable for the vast majority of applications using CR-39 PNTD. The use of AFM for CR-39 PNTD analysis is a time consuming endeavor, which is only appropriate in selected applications, such as the analysis of CR-39 PNTD exposed in space or for baseline measurements used to confirm Monte Carlo calculations for proton radiotherapy. For detectors in which the fluence limitations of the OPT method are exceeded, the AFM provides a valuable alternative analysis system that is capable of accurate analysis on detectors exposed to particle fluence $>10^5$ cm^2. Additionally, in instances in which information is needed regarding short-range, high-LET charged particles, such as HNR particles, the AFM offers a viable means of analysis.

With detailed measurements of short-range, high-LET HNR particles possible, a theoretical framework can be established to accurately treat the dose delivered to tissue by such particles. The energy deposited by HNR particles in their track cores is highly localized, but long range δ-rays generated in the electronic stopping process can travel significantly further. The distribution of energy in tissue, and therefore the distribution of dose, and the associated biological impact of HNR particles, remains to be analyzed.

In applications of CR-39 PNTD in space dosimetry, the advantages of the short-etch process accompanied by AFM analysis are clear; naturally occurring protons in the low Earth orbit environment lead to target fragmentation reactions that can deposit dose in tissue. Using the methods described in this document, a framework for a detailed analysis of this dose contribution now exists. Methods used to model astronaut dose from target fragmentation secondary particles can be augmented and supported by detailed measurements using CR-39 PNTD and the analysis methods presented herein.

8.3. HNR Particle Isotropy

Many nuclear interaction models have emerged to explain the nucleon-nucleon energy exchange that occurs in nuclear collision experiments. Our challenge has been to identify the theoretical formulation that most clearly describes nuclear interactions in the proton energy ranges encountered in this work: 60 MeV to 1 GeV. The Serber two-step model and its modern adaptation, the cascade/evaporation model, serve well in the energy range of interest. In our experiments which tested for HNR particle isotropy, no appreciable deviation from isotropy was observed. Since our data contain the nuclear tracks from all possible HNR particle Z values for a given target nucleus, it is not possible to conclude that each particular HNR particle formation channel is isotropic. Rather, in terms of the process as a whole, anisotropy has not been observed.

8.4. Future work

Many improvements to the algorithms presented here can be made. Implementation of a multi-level analysis method as discussed in Chapter V would likely provide more detailed information regarding the shape of track cones. This would be useful for identifying tracks formed by particles with changing LET. Additionally, the algorithm used for the separation of over-lapped tracks could be modified easily to accommodate multiple overlaps. A robust algorithm for separating multiple over-lapped tracks could allow analysis of detectors exposed to fluences in excess of 10^8 cm^{-2}.

The need for additional data must be emphasized, particularly with respect to proton accelerator exposures. Additional detector exposures are needed to completely analyze the range of proton beam energies used in proton radiotherapy. A reasonable objective would be to study the 50 to 250 MeV proton energy range in 25 MeV increments. This data is necessary to provide a comprehensive analysis of the dose contribution from target fragmentation reactions. Additionally, more data is needed to assess the absorbed dose associated with proton irradiation of target materials of interest to the proton therapy community, such as Ti and Ta. An experiment has been performed with a Ti target layer, but more AFM data is needed to obtain an accurate calculation of the absorbed dose to a tissue layer adjacent to Ti when exposed to energetic protons. The results of angled detector analyses could be vastly improved with additional data. This would also directly support an investigation into an improved method for internal component correction.

In addition to beam exposed detectors, additional space exposures would be useful for quantifying dose to astronauts from HNR particles. Based on the previous literature, it is likely that the methods presented in this work would be of benefit for internal and external detectors exposed on spacecraft. Interpreting the biological impact of HNR particles to astronauts (and proton cancer therapy patients) remains an important objective. With the methods presented here, new tools now exist to study the dosimetric impact of short-range, high-LET particles.

REFERENCES

[Agin, 1981] Agin, G. J. (1981). "Fitting Elipses and General Second-Order Curves." *Robotics Institute, Carnegie Mellon University* **CMU-RI-TR-81-05**.

[Alcaraz et al., 2000] Alcaraz, J., D. Alvisi, et al. (2000). "Protons in near earth orbit." *Physics Letters B* **472**(1-2): 215-226.

[Alexander et al., 1961] Alexander, J. M. and L. Winsberg (1961). "Recoil Studies of Nuclear Reactions Induced by Heavy Ions." *Physical Review* **121**(2): 529.

[Badhwar, 2002] Badhwar, G. D. (2002). "Shuttle Radiation Dose Measurements in the International Space Station Orbits1." *Radiation Research* **157**(1): 69-75.

[Badhwar et al., 1995] Badhwar, G. D.J. U. Patel, et al. (1995). "Measurements of the secondary particle energy spectra in the space shuttle." *Radiation Measurements* **24**(2): 129-138.

[Bailon et al., 2005] Bailon, M. F.P. F. Salinas, et al. (2005). "Application of conductive AFM on the electrical characterization of single-bit marginal failure." Physical and Failure Analysis of Integrated Circuits, 2005. IPFA 2005. Proceedings of the 12th International Symposium on the.

[Beiser, 1952] Beiser, A. (1952). "Nuclear Emulsion Technique." *Reviews of Modern Physics* **24**(4): 273.

[Benton, 2004] Benton, E. R. (2004) *Radiation Dosimetry At Aviation Altitudes And In Low-Earth Orbit*, Ph.D. thesis, Department of Experimental Physics, The National University of Ireland.

[Benton et al., 2000] Benton, E. R. and E. V. Benton (2000). Analysis of CR-39 PNTDs with an Atomic Force Microscope: Pilot Study, Eril Research, Inc.**:** 14.

[Benton et al., 2001a] Benton, E. R. and E. V. Benton (2001a). "Space radiation dosimetry in low-Earth orbit and beyond." *Nuclear Instruments and Methods in Physics Research Section B: Beam Interactions with Materials and Atoms* **184**(1-2): 255-294.

[Benton et al., 2001b] Benton, E. R.E. V. Benton, et al. (2001b). Progress in the Measurement of Target Fragmentation from the Loma Linda University Proton Therapy Facility and the First Measurement of LET Spectra in CR-39 PNTD Using Atomic Force Microscopy, Eril Research, Inc.**:** 39.

[Benton et al., 2002a] Benton, E. R.E. V. Benton, et al. (2002a). "Passive dosimetry aboard the Mir Orbital Station: external measurements." *Radiation Measurements* **35**(5): 457-471.

[Benton et al., 2002b] Benton, E. R.E. V. Benton, et al. (2002b). "Passive dosimetry aboard the Mir Orbital Station: internal measurements." *Radiation Measurements* **35**(5): 439-455.

[Benton et al., 2002c] Benton, E. R.E. V. Benton, et al. (2002c). Target Fragmentation Measurements in the Proton Therapy Beam at LLUMC, Eril Research, Inc.

[Benton et al., 1996a] Benton, E. R.E. V. Benton, et al. (1996a). "Secondary particle contribution to LET spectra on LDEF." *Radiation Measurements* **26**(6): 793-797.

[Benton et al., 2006] Benton, E. R.E. V. Benton, et al. (2006). "Characterization of the radiation shielding properties of US and Russian EVA suits using passive detectors." *Radiation Measurements* **41**(9-10): 1191-1201.

[Benton et al., 1966] Benton, E. V. and M. M. Colliver (1966). "Registration of Heavy Ions During the Flight of Gemini VI." *Health Physics* **13**: 495-500.

[Benton et al., 1972] Benton, E. V.S. B. Curtis, et al. (1972). "Comparison of measured and calculated high-LET nuclear recoil particle exposure on Biosatellite-III." *Health Physics* **23**: 149-157.

[Benton et al., 1996b] Benton, E. V.A. L. Frank, et al. (1996b). "Let spectra measurements on LDEF: Variations with shielding and location." *Radiation Measurements* **26**(6): 783-791.

[Benton et al., 1969a] Benton, E. V. and R. P. Henke (1969a). "Heavy particle range-energy relations for dielectric nuclear track detectors." *Nuclear Instruments and Methods* **67**(1): 87-92.

[Benton et al., 1969b] Benton, E. V. and W. D. Nix (1969b). "The restricted energy loss criterion for registration of charged particles in plastics." *Nuclear Instruments and Methods* **67**(2): 343-347.

[Benton et al., 1986] Benton, E. V.K. Ogura, et al. (1986). "Response of different types of CR-39 to energetic ions." *International Journal of Radiation Applications and Instrumentation. Part D. Nuclear Tracks and Radiation Measurements* **12**(1-6): 79-82.

[Bernardini et al., 1952] Bernardini, G.E. T. Booth, et al. (1952). "Interactions of High Energy Nucleons with Nuclei. Part I." *Physical Review* **85**(5): 826.

[Bertini, 1963] Bertini, H. W. (1963). "Low-Energy Intranuclear Cascade Calculation." *Physical Review* **131**(4): 1801.

[Bethe, 1930] Bethe, H. (1930). "Zur Theorie des Durchgangs schneller Korpuskularstrahlen durch Materie." *Annalen der Physik* **397**(3): 325-400.

[Binnig et al., 1986] Binnig, G.C. F. Quate, et al. (1986). "Atomic Force Microscope." *Physical Review Letters* **56**(9): 930.

[Binnig et al., 1982] Binnig, G.H. Rohrer, et al. (1982). "Surface Studies by Scanning Tunneling Microscopy." *Physical Review Letters* **49**(1): 57.

[Björk, 1996] Björk, A. *Numerical Methods for Least Squares Problems*. (SIAM, 1996).

[Blane et al., 2000] Blane, M. M.Z. Lei, et al. (2000). "The 3L algorithm for fitting implicit polynomial curves and surfaces to data." *Pattern Analysis and Machine Intelligence, IEEE Transactions on* **22**(3): 298-313.

[Blann, 1971] Blann, M. (1971). "Hybrid Model for Pre-Equilibrium Decay in Nuclear Reactions." *Physical Review Letters* **27**(6): 337.

[Blann, 1972] Blann, M. (1972). "Importance of the Nuclear Density Distribution on Pre-equilibrium Decay." *Physical Review Letters* **28**(12): 757.

[Bogdanov et al., 2005] Bogdanov, S.E. Shablya, et al. (2005). "Interaction of gold nuclei with photoemulsion nuclei at energies in the range 100–1200 MeV per nucleon and cascade-evaporation model." *Physics of Atomic Nuclei* **68**(9): 1540-1547.

[Bonnell, 2001] Bonnell, D., (2001)."Scanning probed microscopy and spectroscopy: theory, techniques, and applications." NY, Wiley.

[Bookstein, 1979] Bookstein, F. L. (1979). "Fitting conic sections to scattered data." *Computer Graphics and Image Processing* **9**(1): 56-71.

[Bortfeld, 1997] Bortfeld, T. (1997). "An analytical approximation of the Bragg curve for therapeutic proton beams." *Medical Physics* **24**(12): 2024-2033.

[Cain et al., 2001] Cain, R. G.M. G. Reitsma, et al. (2001). "Quantitative comparison of three calibration techniques for the lateral force microscope." *Review of Scientific Instruments* **72**(8): 3304-3312.

[Carlson et al., 1975] Carlson, R. F.A. J. Cox, et al. (1975). "Proton total reaction cross sections for the doubly magic nuclei O16, Ca40, and Pb208 in the energy range 20-50 MeV." *Physical Review C* **12**(4): 1167.

[Cartwright et al., 1978] Cartwright, B. G.E. K. Shirk, et al. (1978). "A nuclear-track-recording polymer of unique sensitivity and resolution." *Nuclear Instruments and Methods* **153**(2-3): 457-460.

[Cassou et al., 1978] Cassou, R. M. and E. V. Benton (1978). "Properties and applications of CR-39 polymeric nuclear track detector." *Nuclear Track Detection* **2**(3): 173-179.

[Chadwick et al., 1998] Chadwick, M. B.D. T. L. Jones, et al. (1998). Nuclear data for radiotherapy: Presentation of a new ICRU report and IAEA initiatives. Other Information: Supercedes report DE98006323; PBD: [1998]; PBD: 1 Sep 1998**:** Medium: P; Size: 16 pages.

[Cork et al., 1957] Cork, B.W. A. Wenzel, et al. (1957). "Elastic Proton-Proton Scattering at 2.24, 4.40, and 6.15 Bev." *Physical Review* **107**(3): 859.

[Cugnon, 1987] Cugnon, J. (1987). "Proton-nucleus interaction at high energy." *Nuclear Physics A* **462**(4): 751-780.

[Cugnon et al., 1997] Cugnon, J.C. Volant, et al. (1997). "Improved intranuclear cascade model for nucleon-nucleus interactions." *Nuclear Physics A* **620**(4): 475-509.

[Cumming et al., 1981] Cumming, J. B.P. E. Haustein, et al. (1981). "Momentum transfer in the fragmentation of Cu by relativistic heavy ions and protons." *Physical Review C* **24**(5): 2162.

[Doke, 2005] Doke, J. (2005) "GRABIT." from http://www.mathworks.com/matlabcentral/fileexchange/7173.

[Drexel, 2008] Drexel. (2008). "MFM Challenge." Retrieved 6/18/2009, 2009, from http://nanoe.ece.drexel.edu/wiki/index.php/MFM_Challenge.

[Drndic et al., 1994] Drndic, M.Y. D. He, et al. (1994). "Atomic-force-microscopic study of etched nuclear tracks at extremely short distance scale." *Nuclear Instruments and Methods in Physics Research Section B: Beam Interactions with Materials and Atoms* **93**(1): 52-56.

[Durrani et al., 1987] Durrani, S. A. and R. K. Bull. *Solid State Nuclear Track Detection*. (Pergamon Press, Oxford, 1987).

[Fidorra et al., 1981] Fidorra, J. and J. Booz (1981). "Microdosimetric investigations on collimated fast-neutron beams for radiation therapy: I. Measurements of microdosimetric spectra and particle dose fractions in a water phantom for fast neutrons from 14 MeV deuterons on beryllium." *Phys. Med. Biol.* **26**(1): 27-41.

[Fitzgibbon et al., 1999] Fitzgibbon, A.M. Pilu, et al. (1999). "Direct least square fitting of ellipses." *Pattern Analysis and Machine Intelligence, IEEE Transactions on* **21**(5): 476-480.

[Fitzgibbon et al., 1995] Fitzgibbon, A. W. and R. B. Fischer (1995). "A buyer's guide to conic fitting." Proc. of the British Machine Vision Conference, Birmingham, England.

[Fleischer et al., 1975] Fleischer, R. L.P. B. Price, et al. *Nuclear Tracks in Solids*. (University of California Press, Berkeley, 1975).

[Fleischer et al., 1964] Fleischer, R. L.P. B. Price, et al. (1964). "Track Registration in Various Solid-State Nuclear Track Detectors." *Physical Review* **133**(5A): A1443.

[Fleischer et al., 1967] Fleischer, R. L.P. B. Price, et al. (1967). "Criterion for Registration in Dielectric Track Detectors." *Physical Review* **156**(2): 353.

[Geiger et al., 1909] Geiger, H. and E. Marsden (1909). "On a Diffuse Reflection of the alpha-Particles." *Proceedings of the Royal Society of London. Series A* **82**(557): 495-500.

[Geissel et al., 1992] Geissel, H.P. Armbruster, et al. (1992). "The GSI projectile fragment separator (FRS): a versatile magnetic system for relativistic heavy ions." *Nuclear Instruments and Methods in Physics Research Section B: Beam Interactions with Materials and Atoms* **70**(1-4): 286-297.

[Gemignani, 1999] Gemignani, L. (1999). "Fast QR factorization of low-rank changes of Vandermonde-like matrices." *Calcolo* **36**(1): 1-15.

[Ghoshal, 1950] Ghoshal, S. N. (1950). "An Experimental Verification of the Theory of Compound Nucleus." *Physical Review* **80**(6): 939.

[Ginger et al., 2008] Ginger, D. S.K. Kwiatkowski, et al. (2008). "Exclusive studies of 130--270 MeV [sup 3]He- and 200-MeV proton-induced reactions on [sup 27]Al, [sup nat]Ag, and [sup 197]Au." *Physical Review C (Nuclear Physics)* **78**(3): 034601.

[Glassgold, 1958] Glassgold, A. E. (1958). "Nuclear Density Distributions from Proton Scattering." *Reviews of Modern Physics* **30**(2): 419.

[Gottschalk et al., 1993] Gottschalk, B.A. M. Koehler, et al. (1993). "Multiple Coulomb scattering of 160 MeV protons." *Nuclear Instruments and Methods in Physics Research Section B: Beam Interactions with Materials and Atoms* **74**(4): 467-490.

[Gottschalk et al., 1982] Gottschalk, B.A. M. Koehler, et al. (1982). "Radiotherapy with 160 MeV Protons." *Proc. Intern. Sym. Appl. Technol. Ion. Rad.* **1**: 181-203.

[Gottschalk et al., 1999] Gottschalk, B.R. Platais, et al. (1999). "Nuclear interactions of 160 MeV protons stopping in copper: A test of Monte Carlo nuclear models." *Medical Physics* **26**(12): 2597-2601.

[Halíř et al., 1998] Halíř, R. and J. Flusser (1998). "Numerically Stable Direct Least Squares Fitting of Ellipses." 6th International Conference in Central Europe on Computer Graphics and Visualization, CZ, Plzeo, WSCG.

[Harp et al., 1968] Harp, G. D.J. M. Miller, et al. (1968). "Attainment of Statistical Equilibrium in Excited Nuclei." *Physical Review* **165**(4): 1166.

[He et al., 1995] He, Y. D. and C. I. Hancox (1995). "Measurement of low energy ion tracks in CR-39 plastic with an atomic force microscope." *Review of Scientific Instruments* **66**(9): 4575-4582.

[Henke et al., 1971] Henke, R. P. and E. V. Benton (1971). "On geometry of tracks in dielectric nuclear track detectors." *Nuclear Instruments and Methods* **97**(3): 483-489.

[Henke et al., 1986] Henke, R. P.K. Ogura, et al. (1986). "Standard method for measurement of bulk etch in CR-39." *International Journal of Radiation*

Applications and Instrumentation. Part D. Nuclear Tracks and Radiation Measurements **12**(1-6): 307-310.

[Henshaw et al., 1981] Henshaw, D. L.N. Griffiths, et al. (1981). "A method of producing thin CR-39 plastic nuclear track detectors and their application in nuclear science and technology." *Nuclear Instruments and Methods* **180**(1): 65-77.

[Hess, 1958] Hess, W. N. (1958). "Summary of High-Energy Nucleon-Nucleon Cross-Section Data." *Reviews of Modern Physics* **30**(2): 368.

[ICRU, 1993] ICRU, (1993).International Committee on Radiation Units and Measurements "Stopping Power and Ranges for Protons and Alpha Particles." ICRU Report No. 49. Bethesda, MD, ICRU Publications.

[ICRU, 1998] ICRU, (1998).International Committee on Radiation Units and Measurements "Fundamental Quantities and Units of Ionizing Radiation." ICRU Report No. 60. Bethesda, MD, ICRU Publications.

[ICRU, 2000] ICRU, (2000).International Committee on Radiation Units and Measurement "Nuclear Data for Neutron and Proton Radiotherapy and for Radiation Protection." ICRU Report No. 63. Bethesda, MD, ICRU Publications.

[Isralewitz et al., 2001] Isralewitz, B.M. Gao, et al. (2001). "Steered molecular dynamics and mechanical functions of proteins." *Current Opinion in Structural Biology* **11**(2): 224-230.

[Janni, 1982] Janni, J. F. (1982). "Energy loss, range, path length, time-of-flight, straggling, multiple scattering, and nuclear interaction probability : In two parts. Part 1. For 63 compounds Part 2. For elements $1 \leq Z \leq 92$." *Atomic Data and Nuclear Data Tables* **27**(2-3): 147-339.

[Jesse et al., 2006] Jesse, S.H. N. Lee, et al. (2006). "Quantitative mapping of switching behavior in piezoresponse force microscopy." *Review of Scientific Instruments* **77**(7): 073702-10.

[Katz et al., 1968] Katz, R. and E. J. Kobetich (1968). "Formation of Etchable Tracks in Dielectrics." *Physical Review* **170**(2): 401.

[Kodaira et al., 2007] Kodaira, S.N. Yasuda, et al. (2007). "New method of the precise measurement for the thickness and bulk etch rate of the solid-state track detector." *Nuclear Instruments and Methods in Physics Research Section A: Accelerators, Spectrometers, Detectors and Associated*

Equipment **574**(1): 163-170.

[Koehler et al., 1975] Koehler, A. M.R. J. Schneider, et al. (1975). "Range modulators for protons and heavy ions." *Nuclear Instruments and Methods* **131**(3): 437-440.

[Kopniczky et al., 1995] Kopniczky, J.A. Hallén, et al. (1995). "MeV-ion-induced defects in organic crystals." *Radiation Measurements* **25**(1-4): 47-50.

[Kopniczky et al., 1994] Kopniczky, J.C. T. Reimann, et al. (1994). "Scanning-force-microscopy study of MeV-atomic-ion-induced surface tracks in organic crystals." *Physical Review B* **49**(1): 625.

[Lattes et al., 1947] Lattes, C. M. G.G. P. S. Occhialini, et al. (1947). "Observations on the Tracks of Slow Mesons in Photographic Emulsions." *Nature* **160**: 486-492.

[Lu et al., 2006] Lu, H.-M. and H. Kooy (2006). "Optimization of current modulation function for proton spread-out Bragg peak fields." *Medical Physics* **33**(5): 1281-1287.

[Lu et al., 2008] Lu, W. and J. Tan (2008). "Detection of incomplete ellipse in images with strong noise by iterative randomized Hough transform (IRHT)." *Pattern Recognition* **41**(4): 1268-1279.

[Lynch, 1987] Lynch, W. G. (1987). "Nuclear Fragmentation in Proton- and Heavy-Ion-Induced Reactions." *Annual Review of Nuclear and Particle Science* **37**(1): 493-535.

[Machner et al., 2006] Machner, H.D. G. Aschman, et al. (2006). "Isotopic production cross sections in proton-nucleus collisions at 200 MeV." *Physical Review C (Nuclear Physics)* **73**(4): 044606-12.

[Magonov et al., 1997] Magonov, S. N. and D. H. Reneker (1997). "Characterization of Polymer Surfaces with Atomic Force Microscopy." *Annual Review of Materials Science* **27**(1): 175.

[Malfliet, 1981] Malfliet, R. (1981). "Non-equilibrium dynamics in high-energy nucleus-nucleus collisions : (I). Multiple collisions model based on the Boltzmann equation." *Nuclear Physics A* **363**(2): 429-455.

[Miller et al., 1959] Miller, J. M. and J. Hudis (1959). "High-Energy Nuclear Reactions." *Annual Review of Nuclear Science* **9**(1): 159-202.

[Morris et al., 1999] Morris, V. J.A. R. Kirby, et al. *Atomic Force Microscopy for Biologists*. (World Scientific Publishing Co., London, 1999).

[NCRP, 1989] NCRP, (1989).National Council on Radiation Protection and Measurements "Guidance on Radiation Received in Space Activities." NCRP Report No. 98. Bethesda, MD, NCRP Publications.

[Nefedov et al., 1996] Nefedov, N.I. Csige, et al. (1996). "Particle directionality and trapped proton fluences on LDEF." *Radiation Measurements* **26**(6): 881-887.

[Nikezic et al., 2002] Nikezic, D.J. P. Y. Ho, et al. (2002). "Feasibility and limitation of track studies using atomic force microscopy." *Nuclear Instruments and Methods in Physics Research Section B: Beam Interactions with Materials and Atoms* **197**(3-4): 293-300.

[Nikezic et al., 2004] Nikezic, D. and K. N. Yu (2004). "Formation and growth of tracks in nuclear track materials." *Materials Science and Engineering: R: Reports* **46**(3-5): 51-123.

[Paganetti, 2002] Paganetti, H. (2002). "Nuclear interactions in proton therapy: dose and relative biological effect distributions originating from primary and secondary particles." *Physics in Medicine and Biology* **47**(5): 747-764.

[Paganetti et al., 1997] Paganetti, H.P. Olko, et al. (1997). "Calculation of relative biological effectiveness for proton beams using biological weighting functions." *International Journal of Radiation Oncology*Biology*Physics* **37**(3): 719-729.

[Papaleo et al., 2008] Papaleo, R. M.M. R. Silva, et al. (2008). "Direct Evidence for Projectile Charge-State Dependent Crater Formation Due to Fast Ions." *Physical Review Letters* **101**(16): 167601-4.

[Pastushenko, 2006] Pastushenko, V. (2006) "Flatrow." from http://www.mathworks.com/matlabcentral/fileexchange/authors/4126.

[Pilu et al., 1996] Pilu, M.A. W. Fitzgibbon, et al. (1996). "Ellipse-specific direct least-square fitting." Image Processing, 1996. Proceedings., International Conference on.

[Price, 1993] Price, P. B. (1993). "Advances in solid state nuclear track detectors." *Nuclear Tracks and Radiation Measurements* **22**(1-4): 9-21.

[Ratner et al., 1998] Ratner, B. D. and V. V. Tsukruk, (1998)."Scanning Probe

Microscopy of Polymers." ACS Symposium Series, Oxford University Press.

[Reitz et al., 2009] Reitz, G.T. Berger, et al. (2009). "Astronaut's Organ Doses Inferred from Measurements in a Human Phantom Outside the International Space Station." *Radiation Research* **171**(2): 225-235.

[Renberg et al., 1972] Renberg, P. U.D. F. Measday, et al. (1972). "Reaction cross sections for protons in the energy range 220-570 MeV." *Nuclear Physics A* **183**(1): 81-104.

[Rosin, 1996] Rosin, P. L. (1996). "Analysing error of fit functions for ellipses." *Pattern Recognition Letters* **17**(14): 1461-1470.

[Sampson, 1982] Sampson, P. D. (1982). "Fitting conic sections to "very scattered" data: An iterative refinement of the bookstein algorithm." *Computer Graphics and Image Processing* **18**(1): 97-108.

[Sarid, 1997] Sarid, D. *Exploring Scanning Probe Microscopy with Mathematica*. (Wiley, New York, 1997).

[Satchler, 1967] Satchler, G. R. (1967). "Optical model for 30 MeV proton scattering." *Nuclear Physics A* **92**(2): 273-305.

[Schwaller et al., 1979] Schwaller, P.M. Pepin, et al. (1979). "Proton total cross sections on 1H, 2H, 4He, 9Be, C and O in the energy range 180 to 560 MeV." *Nuclear Physics A* **316**(3): 317-344.

[Serber, 1947] Serber, R. (1947). "Nuclear Reactions at High Energies." *Physical Review* **72**(11): 1114.

[Shinn et al., 1999] Shinn, J. L.G. D. Badhwar, et al. (1999). "An analysis of energy deposition in a tissue equivalent proportional counter onboard the space shuttle." *Radiation Measurements* **30**(1): 19-28.

[Shinn et al., 1990] Shinn, J. L.J. W. Wilson, et al. (1990). "Risk assessment methodologies for target fragments produced in high-energy nuclear reactions." *Health Physics* **59**: 141-143.

[Simpson, 1983] Simpson, J. A. (1983). "Elemental and Isotopic Composition of the Galactic Cosmic Rays." *Annual Review of Nuclear and Particle Science* **33**(1): 323-382.

[Singleterry et al., 2001] Singleterry, R. C.F. F. Badavi, et al. (2001). "Estimation of neutron and other radiation exposure components in low earth orbit." *Radiation Measurements* **33**(3): 355-360.

[Snowden-Ifft et al., 1993] Snowden-Ifft, D.P. B. Price, et al. (1993). "Atomic-force-microscopic observations of dissolution of mica at sites penetrated by keV/nucleon ions." *Physical Review Letters* **70**(15): 2348.

[Somogyi, 1980] Somogyi, G. (1980). "Development of Etched Nuclear Tracks." *Nuclear Instruments and Methods* **173**(1): 21-42.

[Somogyi et al., 1973] Somogyi, G. and S. A. Szalay (1973). "Track-diameter kinetics in dielectric track detectors." *Nuclear Instruments and Methods* **109**(2): 211-232.

[Taubin, 1991] Taubin, G. (1991). "Estimation of planar curves, surfaces, and nonplanar space curves defined by implicit equations with applications to edge and range image segmentation." *Pattern Analysis and Machine Intelligence, IEEE Transactions on* **13**(11): 1115-1138.

[Tawara et al., 2002] Tawara, H.T. Doke, et al. (2002). "LET distributions from CR-39 plates on Space Shuttle missions STS-84 and STS-91 and a comparison of the results of the CR-39 plates with those of RRMD-II and RRMD-III telescopes." *Radiation Measurements* **35**(2): 119-126.

[Thibaudau et al., 1991] Thibaudau, F.J. Cousty, et al. (1991). "Atomic-force-microscopy observations of tracks induced by swift Kr ions in mica." *Physical Review Letters* **67**(12): 1582.

[Veeco, 1998] Veeco (1998). *Command Reference Manual*. (Digital Instruments, Inc., Santa Clara, CA, 1998). http://www.veeco.com/contact/user_manuals.aspx.

[Veeco Instruments, 2005a] Veeco Instruments, I. (2005a) "A Practical Guide to SPM." from http://www.veeco.com/pdfs/library/SPM_Guide_0829_05_166.pdf.

[Veeco Instruments, 2005b] Veeco Instruments, I. (2005b) "Scanning Probe/Atomic Force Microscopy: Technology Overview and Update." Application Note 48 Rev A2, from http://www.veeco.com/pdfs/appnotes/AN48r2_SPM_AFM_278.pdf.

[Viola et al., 2006] Viola, V. E.K. Kwiatkowski, et al. (2006). "Light-ion-induced multifragmentation: The ISiS project." *Physics Reports* **434**(1-2): 1-46.

[Waddington et al., 1985] Waddington, C. J. and P. S. Freier (1985). "Interactions of energetic gold nuclei in nuclear emulsions." *Physical Review C* **31**(3): 888.

[Williams et al., 1967] Williams, I. R. and C. B. Fulmer (1967). "Excitation Functions for Radioactive Isotopes Produced by Protons below 60 MeV on Al, Fe, and Cu." *Physical Review* **162**(4): 1055.

[Wilson et al., 1993] Wilson, J. W.F. A. Cucinotta, et al. *Target fragmentation in radiobiology*. 1993).

[Wilson, 1946] Wilson, R. R. (1946). "Radiological use of fast protons." *Radiology* **47**: 487-491.

[Winsberg, 1964] Winsberg, L. (1964). "Recoil Studies of Nuclear Reactions Induced by High-Energy Particles. I. Production of Tb149." *Physical Review* **135**(5B): B1105.

[Winsberg, 1978] Winsberg, L. (1978). "The analysis of thick-target thick-catcher nuclear recoil experiments." *Nuclear Instruments and Methods* **150**(3): 465-477.

[Winsberg, 1980a] Winsberg, L. (1980a). "Systematics of particle-nucleus reactions. I. Parameters." *Physical Review C* **22**(5): 2116.

[Winsberg, 1980b] Winsberg, L. (1980b). "Systematics of particle-nucleus reactions. II. Nuclear recoil in nonfission reactions induced by 1-GeV to 400-GeV protons." *Physical Review C* **22**(5): 2123.

[Winsberg et al., 1961] Winsberg, L. and J. M. Alexander (1961). "Ranges and Range Straggling of Tb149, At, and Po." *Physical Review* **121**(2): 518.

[Winsberg et al., 1980] Winsberg, L.E. P. Steinberg, et al. (1980). "Recoil properties of nuclei produced in the interaction of protons with Al27." *Physical Review C* **22**(5): 2108.

[Wroe et al., 2005] Wroe, A. J.I. M. Cornelius, et al. (2005). "The role of nonelastic reactions in absorbed dose distributions from therapeutic proton beams in different medium." *Medical Physics* **32**(1): 37-41.

[Yamamoto et al., 1997] Yamamoto, M.N. Yasuda, et al. (1997). "CR-39 sensitivity analysis on heavy ion beam with atomic force microscope." *Radiation Measurements* **28**(1-6): 227-230.

[Yamamoto et al., 1999] Yamamoto, M.N. Yasuda, et al. (1999). "Atomic force microscopic analyses of heavy ion tracks in CR-39." *Nuclear Instruments and Methods in Physics Research Section B: Beam Interactions with Materials and Atoms* **152**(2-3): 349-356.

[Yasuda et al., 2001] Yasuda, N.K. Uchikawa, et al. (2001). "Estimation of the latent track size of CR-39 using atomic force microscope." *Radiation Measurements* **34**(1-6): 45-49.

[Yasuda et al., 1999] Yasuda, N.M. Yamamoto, et al. (1999). "Track sensitivity and the surface roughness measurements of CR-39 with atomic force microscope." *Radiation Measurements* **31**(1-6): 203-208.

[Yasuda et al., 1998] Yasuda, N.M. Yamamoto, et al. (1998). "Measurement of bulk etch rate of CR-39 with atomic force microscopy." *Nuclear Instruments and Methods in Physics Research Section B: Beam Interactions with Materials and Atoms* **142**(1-2): 111-116.

[Zhang, 1997] Zhang, Z. (1997). "Parameter estimation techniques: a tutorial with application to conic fitting." *Image and Vision Computing* **15**(1): 59-76.

GLOSSARY

Atomic force microscope (AFM); This type of microscope uses a fine silicon tip to physically probe surface features, thereby forming a topographic map of a surface. Discussed in detail in Chapter IV.

Brookhaven National Laboratory (BNL); Laboratory in Brookhaven, NY that hosts the NSRL.

Bulk etch (B); The thickness of CR-39 PNTD material removed by chemical etching.

Bulk etch rate (V_G); The rate at which chemical etching removes CR-39 PNTD material in areas not exposed to charged particles.

Charge coupled device (CCD); The optical encoding semiconductor device used by digital cameras and video recorders.

Continuous slowing down approximation (CSDA); This approximation is used by the Bethe-bloch formula to simplify the calculation of stopping power, it assumes interaction occurs over a continuum as opposed to discrete locations.

Estimate of fit (EOF); A formula used to quantify the accuracy of a fitted ellipse. Typically weighted as in gradient weighted EOF.

Fluence cascade (FLUKA); A Monte Carlo package useful for nuclear collision modeling.

Galactic Cosmic Ray (GCR) background; Naturally occurring background radiation consisting of energetic protons and heavy ions. Proton energy can extend up to 10^{22} eV, but as energy increases the number of protons with that energy is reduced.

Heavy nuclear recoil (HNR) particle; A type of heavy ion radiation formed as a result of nuclear collisions having short-range and high-LET. These particles are emitted in the second step of the Serber two-step model.

Intermediate mass fragment (IMF); A type of heavy ion radiation formed as a result of nuclear collisions. These particles are formed in the first step of the Serber two-step model and have velocity peaked in parallel with the primary ion beam.

Intra-nuclear cascade (INC); In recent literature, the first step of the Serber two-step model is often referred to as an intra-nuclear cascade due to the exchange of energy between nucleons.

Linear energy transfer (LET); Term used to represent the energy deposition of a charged particle along its path (dE/dx).

Loma Linda University Medical Center (LLUMC); This proton cancer treatment center donated beam time for many experiments in this work as well as the AFM used in this work.

Long duration exposure facility (LDEF); LDEF was an experiment placed in orbit by space shuttle *Challenger* consisting of many various test materials designed to test the effects of space exposure.

NASA Space Radiation Laboratory (NSRL); A laboratory designed to use heavy ion beams to study the biological effects of simulated space radiations.

Multi-layer Faraday cup (MLFC); An instrument used to detect charge deposition as a function of depth in beam experiments.

Optical microscopy methods (OPT); This term is used for the established means of CR-39 PNTD analysis via examination with an optical microscope. For this analysis method long duration chemical etching is typically used.

Plastic nuclear track detector (PNTD); Term used to describe a track detecting material composed of plastic, a subset of the broader classification SSNTD.

Restricted energy loss (REL); Energy deposited along the path of a charged particle which is transferred to electrons with final energy below a predetermined threshold.

Scanning probe microscopy (SPM); Term used to describe a broad class of microscopy tools which use physical probes to analyze surface characteristics as opposed to visible light or electron beams.

Scanning tunneling microscope (STM); First member of the SPM class, this variant of SPM measures tunneling current with a sharp metal tip with respect to X and Y on a metal (or conducting) surface.

Spread out Bragg peak (SOBP); This term applies to range modulated proton beams used in proton radiotherapy. The spread out Bragg peak is the sum of multiple proton Bragg curves after passing through a range modulation device, such as a stepped wedge range modulator wheel.

Solar particle event (SPE); Temporary increase in proton flux due to solar activity.

Solid state nuclear track detector (SSNTD); A dielectric solid with characteristics that make it useful as a track detector. ‘Good’ track detectors are homogenous, transparent, and have a suitable etchant available for chemical etching.

South Atlantic anomaly (SAA); Region in orbit over South America in which trapped proton flux is highest due to an irregularity in the magnetic field of the Earth

Tissue equivalent proportional counter (TEPC); A type of gas-filled radiation detector that is composed of materials that render its measurement output nearly equivalent to dose in tissue

Track candidate (TC); Used in this work to refer to the matrix of points collected at a depth, S, below the surface value for testing as a nuclear track.

Track etch rate (V_T); The rate at which chemical etching removes CR-39 PNTD material along the latent damage trail formed on the trajectory of a charged particle.

Track length (L_R); The length of a latent damage trail formed by the passage of a charged particle.

Z: The number of protons in the nucleus of an atom.

VITA

Carl E. Johnson Jr.

Candidate for the Degree of

Doctor of Philosophy

Dissertation: ATOMIC FORCE MICROSCOPY METHODS FOR THE ANALYSIS OF HIGH-LET TRACKS IN CR-39 PLASTIC NUCLEAR TRACK DETECTOR

Major Field: Physics

Biographical:

Personal Data: Born October 4, 1969 in Tulsa Oklahoma.

Education:
Completed the requirements for the Doctor of Philosophy degree in Physics at Oklahoma State University, Stillwater, Oklahoma in July, 2009.

Received the Master of Science in Applied Science at the University of Arkansas at Little Rock, Little Rock, Arkansas in 2005.

Received the Bachelors of Science in Physics at the University of Arkansas at Little Rock, Little Rock, Arkansas in 2003.

Experience: Served as Naval Nuclear Propulsion Plant Operator in the United States Navy from 1987 to 1993. Worked as a licensed boiler and machinery inspector from 1995 to 2003.

Name: Carl E. Johnson Date of Degree: July, 2009

Institution: Oklahoma State University Location: Stillwater, Oklahoma

Title of Study: ATOMIC FORCE MICROSCOPY METHODS FOR THE ANALYSIS OF HIGH-LET TRACKS IN CR-39 PLASTIC NUCLEAR TRACK DETECTOR

Pages in Study: 185 Candidate for the Degree of Doctor of Philosophy

Major Field: Physics

Scope and Method of Study: Proton- and neutron-induced target fragmentation reactions generate short-range (~1-10 μm), high-linear energy transfer (LET) heavy nuclear recoil (HNR) particles that contribute to total radiation dose deposited in healthy tissue in patients undergoing proton cancer therapy and to astronauts during spaceflight. Conventional detection using CR-39 plastic nuclear track detector (PNTD) that has been chemically etched for analysis by standard visible light microscopy fails because the required bulk etch, $B \approx 40$ μm removes short-range tracks. We have developed a method based on Atomic Force Microscopy (AFM) to directly measure HNR particle tracks in CR-39 PNTD. Novel algorithms using least squares ellipse fitting and estimation of fitting in an iterative process were developed to enable the analysis of nuclear tracks in AFM data. In irradiations conducted at the Loma Linda University Medical Center (LLUMC) Proton Therapy Facility and the NASA Space Radiation Laboratory (NSRL) at Brookhaven National Laboratory (BNL), targets of varying composition, including a number of elemental targets of high Z, were exposed in contact with layers of CR-39 PNTD to beams of 60 MeV, 230 MeV, and 1 GeV protons at doses between 2 and 10 Gy. Chemical etching of the CR-39 PNTD was performed under standard conditions (50°C, 6.25 *N* NaOH) for 2-4 hours (removed layer $B = 0.5$-1.0 μm).

Findings and Conclusions: The use of a short duration chemical etch yielded densities of secondary tracks of 10^5-10^6 cm^{-2} using the analysis methods presented in this work for accelerator-based experiments. LET spectra were obtained with good statistics between 200 and 1500 keV/μm and the results were consistent with nonelastic nuclear cross sections. Absorbed dose measurements were also completed for selected detectors, ~7×10^{-10} Gy ion^{-1} was measured for 230 MeV protons. Additionally our data are consistent with an isotropic HNR particle production mechanism. The semi-automated analysis method developed in this work has demonstrated the capability of analyzing detectors exposed to fluences of 10^8 cm^{-2} for detectors exposed on spacecraft. This method should prove to be broadly applicable in future studies of HNR particles.